Editors' Suggestion

Demonstration of a kicker impedance reduction scheme with diode stack and resistors by operating the 3-GeV rapid cycling synchrotron of the Japan Proton Accelerator Research Complex

Yoshihiro Shobuda, Hiroyuki Harada, Pranab Kumar Saha, Tomohiro Takayanagi, Fumihiko Tamura, Tomohito Togashi, Yasuhiro Watanabe, Kazami Yamamoto, and Masanobu Yamamoto

JAEA, Japan Atomic Energy Agency, 2-4 Shirakata, Tokaimura, Nakagun, Ibaraki 319-1195, Japan

(Received 23 August 2022; accepted 5 May 2023; published 31 May 2023)

At the Rapid Cycling Synchrotron (RCS) in Japan Proton Accelerator Research Complex (J-PARC), theoretical predictions have indicated that the kicker impedance would excite the beam instability. A 1-MW beam with large emittance can be delivered to the Material and Life Science Experimental Facility through suppression of the beam instabilities by choosing the appropriate machine parameters. However, we require other high-intensity and high-quality smaller emittance beams (than the 1-MW beam) for the main ring. Hence, we proposed a scheme for suppressing the kicker impedance by using prototype diodes and resistors, thereby demonstrating the effect on the kicker impedance reduction. However, the J-PARC RCS must be operated with a repetition rate of 25 Hz, which urged us to consider special diodes that are tolerant to heating. After developments, we have demonstrated that the special diodes with resistors can suppress the beam instability by reducing the kicker impedance. Enhanced durability of the prototype diodes and resistors for the 25-Hz operation was also realized. Moreover, the new diodes and the resistors have a negligible effect on the extracted beam from the RCS. From a simulation point of view, the scheme can be employed for at least 5-MW beam operation within the stipulated specifications.

DOI: 10.1103/PhysRevAccelBeams.26.053501

I. INTRODUCTION

The 3-GeV Rapid Cycling Synchrotron (RCS) in Japan Proton Accelerator Research Complex (J-PARC) [1] has accelerated two bunches containing 4.15×10^{13} particles per bunch from 400 MeV to 3 GeV in 20 ms. This acceleration with a repetition rate of 25 Hz has made a 1-MW beam operation possible [2]. The beam instability [3] excited by the extraction kicker magnet has been the main issue that limits the generation of the high-intensity beam since the construction phase [4]. However, theoretical, simulation, and experimental measurements have clarified the mechanism of space-charge effects (including indirect space-charge effects) to suppress beam instability in a space-charge-dominated machine (like the RCS) [5–7].

The RCS provides proton beams downstream to both the Material and Life Science Facility (MLF) and the main ring (MR) [8]. The standard unnormalized transverse painting emittance, the unnormalized value of the entire painting area, for the MLF, is relatively large (e.g., 200π mm mrad), which can easily stabilize a high-intensity beam (even a 1-MW beam) without any transverse feedback system by just turning off the sextupole magnets. However, the emittance must be less than 50π mm mrad for the MR. Small emittance broadens the transverse tune spreads due to space-charge effects, restricting the variable tune-tracking pattern during the acceleration period. Furthermore, suppression of beam instability is more difficult with a smaller transverse emittance than with a larger emittance, because the suppression effect due to the indirect space-charge force is relatively mitigated for the smaller transverse emittance beam [6,7]. In the end, lowering the kicker impedance [3] is required for the generation of high-intensity and high-quality small emittance beams by the RCS.

The kicker at the RCS is a transmission-line type embedding two ferrite cores [9]. The kicker has four terminals, two of which are connected to the power supply through 130-m long coaxial cables [10], and the other two are terminated in a short circuit [9]. The shorted ends are beneficial for beam extraction, owing to the doubled excitation currents. However, the drawback is that these terminal conditions enhance the kicker impedance [11,12].

The standard method of suppressing the kicker impedance involves inserting matched resistors at the end of the kicker terminals [13]. However, the scheme makes void the merit of the doubled excitation currents with the shorted ends.

To overcome this difficulty, in previous work, we suggested inserting diodes with matched resistors at the end of the kicker terminals [14,15]. This scheme guarantees doubled excitation currents with the shorted ends by preventing the forward current created by the pulse forming line (PFL) from flowing into the matched resistor. Furthermore, the beam-induced current with high frequency can pass through the diodes and is absorbed into the matched resistors suppressing the kicker impedance.

However, from a practical point of view, additional efforts are required because the heating on the diodes and resistors can destroy these parts under the 25-Hz repetition routine operation of RCS; this could occur even though these parts are cooled in an oil tank. The specification of the diodes and the resistors requires temperatures below 85 and 150 °C, respectively. In addition, Ref. [16] suggested that the fast-rising voltage across the diodes during the turn-on of the thyratron switch may cause degradation of the diode stack due to transient voltage. Further studies are therefore required to determine the reliability of this impedance reduction method. Moreover, the attached diodes and resistors may have a significant effect on the extraction beams from the RCS [16].

Accordingly, we have developed a new special diode module to address these concerns. The suppression of the temperature rise on the diodes enhances the diode-stack durability by mitigating the burden from the voltages across the diodes, as demonstrated by continuous operations with a 25-Hz repetition rate. Moreover, we have improved the function of the diodes and resistors to reduce the kicker impedance to the impedance level of the "fictitious" kicker whose terminals were terminated only with matched resistors. Overall, the scheme has successfully suppressed (with sufficient durability) the beam instability without affecting the extraction beams from the RCS, which is also demonstrated by measurements.

The paper is organized as follows: In Sec. II, we review the basic concepts for reducing the kicker impedance with diodes and matched resistors. In Sec. III, we illustrate the strategy for designing the new diode module. In Sec. IV, we discuss the validity of the parameters describing the kicker and the diode units used in SPICE© (simulation program with integrated circuit emphasis) for the circuit simulations [17,18]. We describe the measurements of currents and voltages excited by the PFLs (pulse forming lines), consistent with the simulation results. In Sec. V, we analyze the temperature rise of the diode unit cooled in the oil tank from analytical, simulation, and measurement points of view. The simulations suggest that the scheme can be applied to up to 5-MW beams suppressing the kicker impedance with sufficient durability, in principle. In Sec. VI, we analytically discuss the temperature rise of the oil tank to indirectly detect the malfunction of the diode module in it and measured the temperature of oil during 45 days of 830-kW routine beam operations, by which the durability of the unit is demonstrated. In Sec. VII, we reveal the kicker impedance reduction by using the new diode unit from simulation and measurement points of view. In Sec. VIII, we discuss the effect of the diode units on the extraction beams from the RCS after demonstrating the suppression of the beam instabilities during the acceleration. The paper is summarized in Sec. IX.

II. BASIC CONCEPTS TO REDUCE THE KICKER IMPEDANCE WITH DIODES AND MATCHED RESISTORS

Figure 1 illustrates the present kicker at the RCS equivalent electrical circuit model. The kicker is a transmission-line type, combined with two ferrite cores embedding aluminum coils. Each core has two terminals, where one is connected to one end of a thyratron through two 130-m long coaxial cables and the other end is terminated in a short circuit. Thanks to the shorted ends on the kicker magnet, the excitation currents are doubled for beam extraction from the RCS, and consequently, the electric power is halved.

Two sets of two 110-m long coaxial cables [10] comprise two sets of PFLs in Figs. 1 and 2. One end of each cable is terminated by the diode before the matched load (hereafter this diode with 20-Ω resistor is referred to as end-clipper).

The charging method is a constant current type using an IGBT (insulated gate bipolar transistor). The charging time is set to 30 ms and the hold time is defined as 6 ms at the maximum charging voltage of 80 kV. This voltage is set to 60 kV in routine operation for extraction of the beams from the RCS [9].

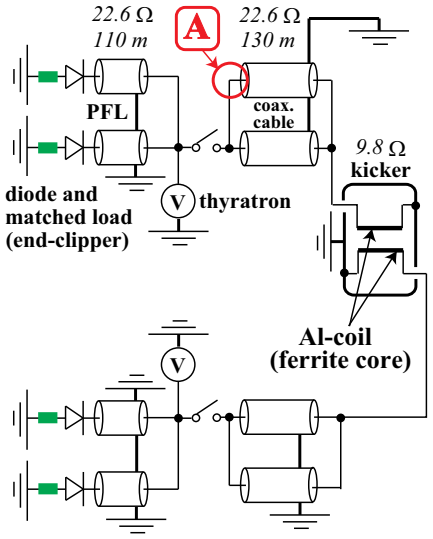

FIG. 1. Diagram illustrating the present kicker equivalent electrical circuit model. The location "A" shows the current monitoring point of Figs. 10, 13, 15, 16, 19, and 53. The current transformer at "A" is placed in the direction to display positive when the currents flow to the kicker magnet.

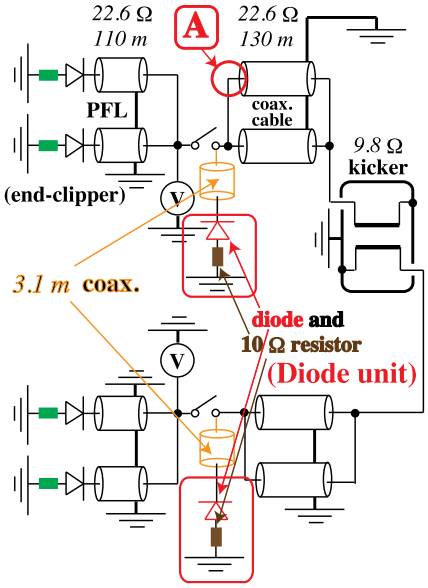

FIG. 2. Diagram illustrating the improved kicker equivalent electrical circuit model. The location "A" shows the current monitoring point of Figs. 9, 10, 13, 18, 19, 20, 24, and 53. The current transformer at "A" is placed in the direction to display positive when the currents flow to the kicker magnet.

Two thyratrons and four end-clippers are placed in the respective oil tanks, which are connected to the oil pipes, through which the cooling oil is circulated.

In Fig. 2, the diode with the matched resistor (hereafter, this diode with 10-Ω resistor is referred to as diode unit) is attached to the thyratron through a 3.1-m long 20-Ω coaxial-cable after creating another terminal on the thyratron [10]. The kicker is a transmission line and combined type-kicker, and hence two diode units must be prepared for the left- and right-hand side of the kicker (hereafter, depending on the situation, we refer to the former unit as diode unit 1 and the latter unit as diode unit 2). The diode units are inserted at the ends of 130-m long coaxial cables, and therefore the diodes prevent the forward current due to the PFLs from flowing into the matched resistors. In addition, the beam-induced current with high frequency is absorbed into the resistors, suppressing the kicker impedance. Hence, the benefit secured by the shorted ends is maintained, while the beam impedance of the kicker is suppressed [14,15].

From an engineering viewpoint, the reverse voltage V_R of the diode must be high enough to intercept the pulse voltage from the PFLs. The corresponding forward voltage drops V_F must be low enough to allow a small amplitude beam-induced voltage pulse to be affected by the resistor.

In the RCS, V_R is set to 50 kV, and V_F must be kept below 50 V. The diffused junction silicon diodes in the prototype diode unit were developed by ORIGIN [19]. Figure 3 shows a picture of the prototype diode unit [14,15] comprising diodes and resistors. The diode consists of four parallel branches. Each branch has 13 modules in series. Table I shows the SPICE© parameters for each module [14].

Two diode units, placed in the respective oil tanks, are cooled by circulating oil, which is used for the thyratrons and the end-clippers. As shown in Fig. 3, the diode is installed in the oil container, which is designed such that the oil flows in from the bottom of the container; the oil flows out from the top of the container. However, the diode module is enclosed in a capsule (black) as shown in the left picture of Fig. 4 and is therefore ineffective in cooling the diode module. Though the capsuled diodes have been put to practical use for end-clippers (refer to Fig. 6 in Ref. [20]), they differ significantly from the diode unit in that the beam-induced currents flow to the units during beam accelerations. Moreover, the fast-rising voltage across the diode unit during the turn-on of the thyratron switch may lead to degradation of the unit due to transient voltage, as discussed in [16].

To address this concern, we design a new diode module, sustainable for the 25-Hz continuous operations of the kicker magnet. In the following section, we illustrate how to design the new diode module for practical use of the diode units.

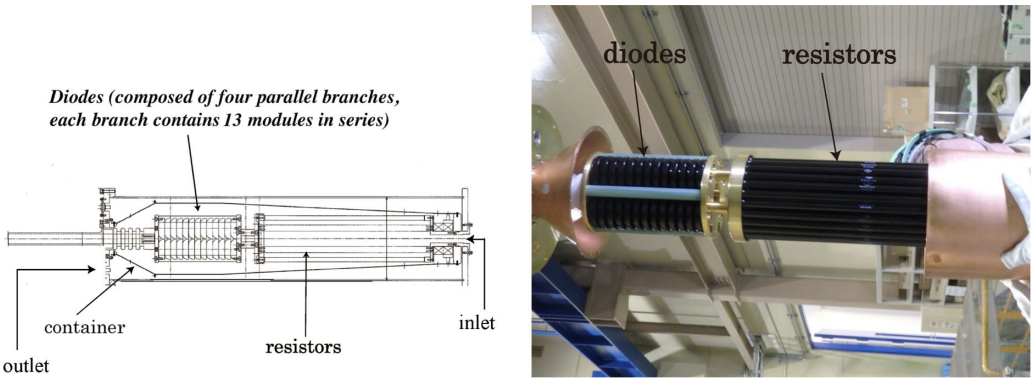

FIG. 3. A detailed diagram (left) and a photo (right) showing a series circuit of 10 Ω resistors and prototype diode unit.

TABLE I. SPICE© parameters for one prototype diode module [14].

Parameters	Units	Value
Saturation current	A	2.04×10^{-6}
Ohmic resistance	Ω	0.01
Emission coefficient	···	8.28
Transit time	*s*	7.21×10^{-4}
Zero-bias junction capacitance	F	1.52×10^{-9}
Junction potential	V	0.423
Grading coefficient	···	0.063
Action energy	eV	1.1
Saturation current temperature exponent	···	3
Flicker noise coefficient	···	0
Flicker noise exponent	···	1
Coefficient for forward bias	···	0.5
Reverse breakdown voltage	V	4000
Current at breakdown voltage	A	5.0×10^{-5}
Normal temperature	℃	25

III. STRATEGY FOR DESIGNING THE NEW DIODE MODULE

To enhance the cooling efficiency of the diode module, we design the new module for direct contact with the circulating oil. For this purpose, we decompose the prototype diode module by scrapping the black capsule shown in Fig. 3. One capsuled diode module consists of 12 "minidiodes" and four capacitors each with 1000 pF (see the right panel in Fig. 4). Table II shows SPICE© parameters for one minidiode. Regarding the minidiodes, one diode shown in Fig. 2 consists of 24 parallel and 26 series minidiodes and 8 parallel and 26 series 1000 pF capacitors.

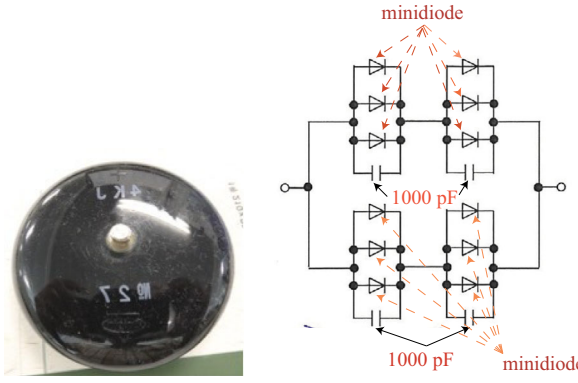

FIG. 4. A picture of one prototype diode module (left) shown in Fig. 3, and the internal structure based on the electrical circuit model. The structure consists of 12 minidiodes (refer to Table II) and four 1000 pF capacitors (right).

TABLE II. SPICE© parameters for minidiode shown in Fig. 4.

Parameters	Units	Value
Saturation current	A	5.58×10^{-8}
Ohmic resistance	Ω	0.01
Emission coefficient	···	3.84
Transit time	*s*	3.75×10^{-6}
Zero-bias junction capacitance	F	1.74×10^{-10}
Junction potential	V	1.055
Grading coefficient	···	0.449
Action energy	eV	1.1
Saturation current temperature exponent	···	3
Flicker noise coefficient	···	0
Flicker noise exponent	···	1
Coefficient for forward bias	···	0.5
Reverse breakdown voltage	V	2000
Current at breakdown voltage	A	5.00×10^{-5}
Normal temperature	℃	25

The basic strategy for modification of the diode shown in Fig. 2 is to (i) immerse the minidiodes directly in circulating oil, (ii) increase the number of parallel branches, thereby reducing the heat load on the respective diodes and the synthetic inductance of the diode stack, and (iii) limit the synthetic capacity of the diode stack to less than 0.5 nF. This value is equivalent to the synthetic capacity of the prototype diode stack, which is calculated as

$$\frac{(24 \times cjo_{\mathrm{mini}} + 8 \times 10^{-9})}{26} \simeq 0.5 \times 10^{-9}\ F, \qquad (1)$$

where $cjo_{\mathrm{mini}} = 1.74 \times 10^{-10}$ is the "zero-bias junction capacitance" of the minidiode described in Table II.

Figure 5 shows a photo of the newly designed diode unit comprising a 10-Ω resistor and the diode stack. A magnified photo of the diode stack is shown in the lower panel of Fig. 6. The schematic presented in the upper and middle panels in Fig. 6 shows the configuration of the stack, where the black capsule shown in Fig. 4 has been removed. Furthermore, the minidiodes are arranged in a ladder shape with an increasing number of parallels of the branches comprising the diode stack, thereby reducing the heat load on the diodes and the synthetic inductance of the stack. Slits are placed in the insulator base that supports the minidiodes, in order to increase the cooling efficiency of the respective diodes by allowing oil flow through these slits. One diode (see Fig. 2) consists of 30 parallel and 27 series minidiodes and 6 parallel and 27 series 1000 pF capacitors in this new diode stack. As a result, the synthetic capacitor capacity is calculated as

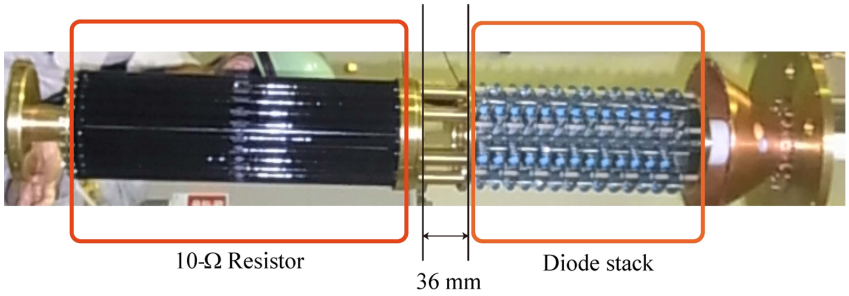

FIG. 5. A photo of a newly designed diode unit comprising a 10-Ω resistor and the diode stack.

$$\frac{(30 \times cjo_{\text{mini}} + 6 \times 10^{-9})}{27} = 0.415 \times 10^{-9}\ F, \quad (2)$$

which is lower than $0.5 \times 10^{-9}\ F$.

Figure 7 shows a schematic and a photo of the diode unit consisting of the newly designed diode stack and the resistors in the oil tank that lies below the relay box. Figure 8 shows a setup, where two diode units are placed on the left-hand side and the right-hand side of the kicker power supply, respectively. As shown in Fig. 5, the diode stack and the 10-Ω resistor are separated by a distance of 36 mm. This is quite different from the structure of the end-clipper, where no such space exists (see Fig. 6 in Ref. [20]). Owing to the space, the heat propagation from the resistors to the diode stack can be strongly suppressed even for a 1-MW beam operation (refer to Sec. V B).

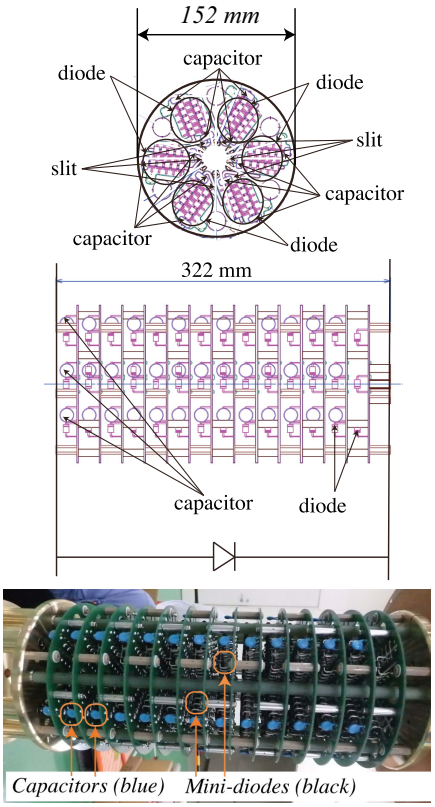

FIG. 6. Schematic pictures of the newly designed diode stack (upper/middle) and a photo of it (lower). The middle and lower panels show the side view, and the upper panel illustrates the view from the anode side (refer to Fig. 12).

To attach a voltage probe and current transfer to the diode unit, the relay box is placed on the unit, and hence we can measure the voltages across the unit and the currents on the unit, where the current transfer is placed in the direction to display positive when the currents flow from 10-Ω resistor to the diode stack. The relay box is well approximated as a series circuit comprising four parallel resonator circuits, where ($R_1 = 296\ \Omega$, $L_1 = 166.5$ nH, $C_1 = 25.3$ pF), ($R_2 = 1286\ \Omega$, $L_2 = 26.8$ nH, $C_2 = 41.4$ pF), ($R_3 = 9799\ \Omega$, $L_3 = 10.9$ nH, $C_3 = 8.12$ pF), and ($R_4 = 223.5\,\Omega$, $L_4 = 2.65$ nH, $C_4 = 39.6$ pF) [15]. These values are obtained from the conversion of the S-matrix for the relay box calculated with the three-dimensional simulation code CST STUDIO© [21]. The oil tank and the box are electrically connected and grounded. Note that 3.1-m long 20-Ω coaxial cables are connected between the box and the thyratron in Figs. 7 and 8.

Figure 9 compares the measured current waveform with the prototype diode unit and the waveform with the new diode unit observed at "A" in Fig. 2. The results indicate that the waveforms undergo comparable levels of deformation, demonstrating the success of the strategy for designing the new diode stack.

Figure 10 shows the measured forward current in the kicker with (blue) the new diode unit observed at "A" in Fig. 2 and that in the present kicker (red) without the unit observed at "A" in Fig. 1. Again, we can identify that a significant ripple is excited on the current waveform when the diode unit is attached to the kicker.

It should be reminded that two bunches must be successively extracted from the RCS within about 1.0 μs (see Fig. 11) [9]. That is when we assume that the superposed forward and backward waveform currents with the ripple directly affect the magnetic field in the kicker

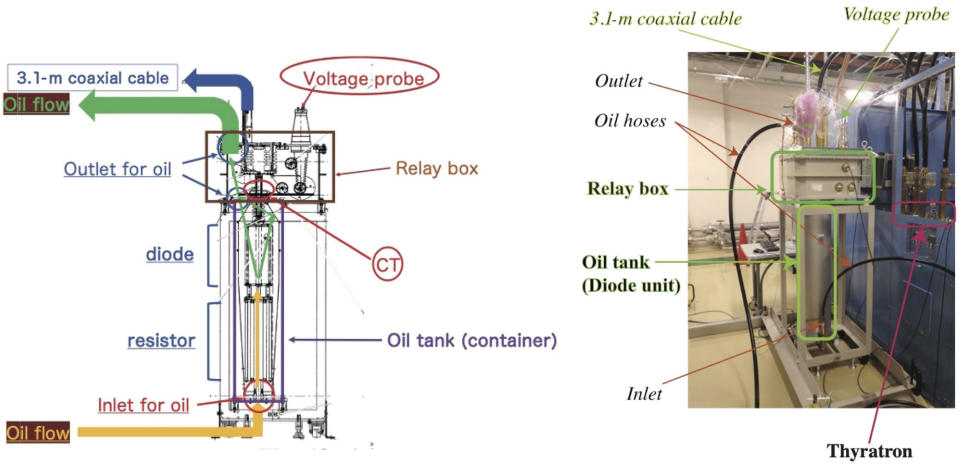

FIG. 7. A schematic (left) and a photo (right) of the diode unit consisting of the diode and the resistors in the oil tank located below the relay box.

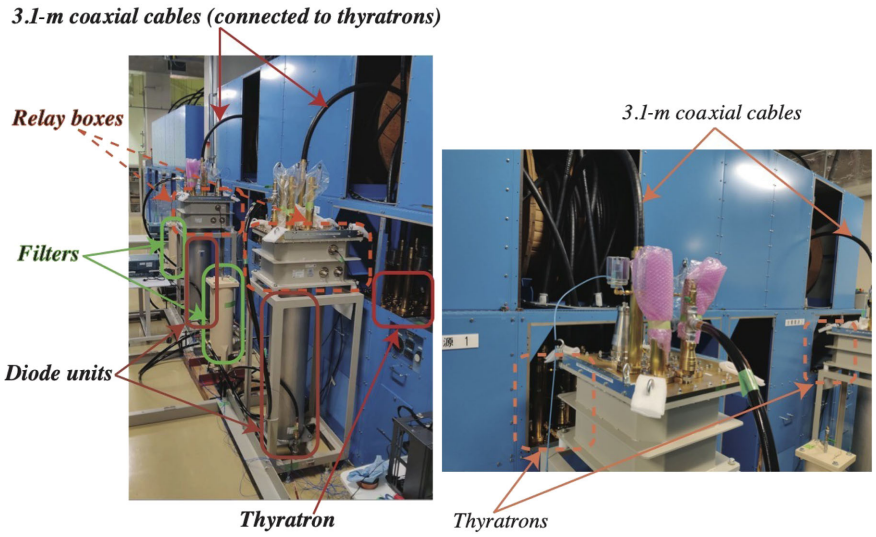

FIG. 8. Photos of two diode units placed on the kicker. The left and right panels show the pictures from the right-hand and left-hand sides for the kicker power supply, respectively.

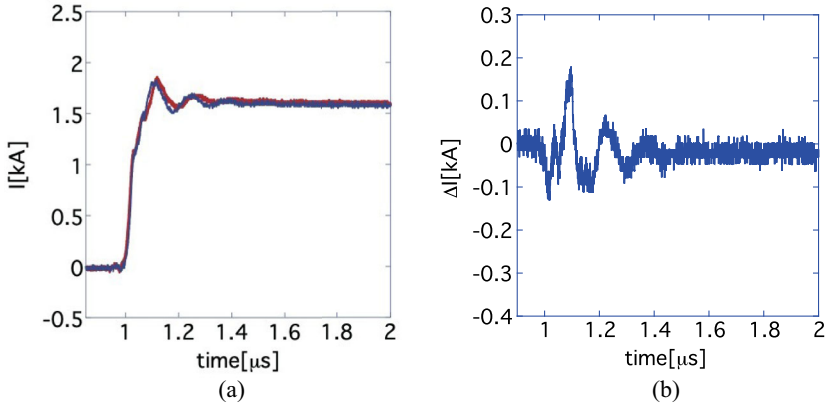

FIG. 9. The difference between the measured current waveform with the prototype diode unit and with the improved diode unit at position "A" in Fig. 2. The diode units are connected to the thyratron container via a 3.1-m long coaxial cable (a) Overlaid forward current waveforms with the prototype diode unit (red) and with the improved diode unit (blue). (b) Forward current waveform with the improved diode unit subtracting the one with the prototype diode unit.

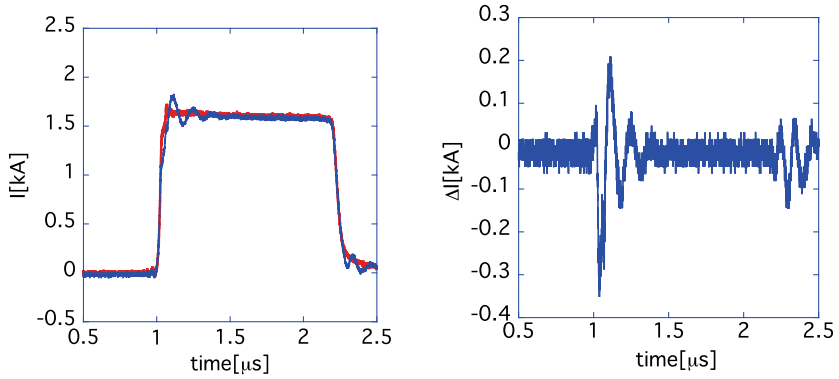

FIG. 10. Difference between the forward current waveform with and without the diode unit at "A" in Figs. 1 and 2 (measurements). The unit is connected to the thyratron container via a 3.1-m long coaxial cable. (a) Overlaid forward current waveforms with (blue) and without (red) the diode unit. (b) Forward current waveform with the diode unit subtracting the one without it.

magnet, it is possible that the trajectories of the first and the second extracted bunches intolerably deviate, depending on the arriving timing of the bunches at the flattop of the trapezoidal waveform of the generated magnetic field. Whether this speculation is true or not will be discussed in Sec. VIII B.

Here, let us investigate whether the MW solver of CST STUDIO©, a typical three-dimensional simulator, can simulate the entire kicker system including the diode unit, the power supply, and the magnetic parts by monitoring the current at position "A" in Fig. 2, where the parameter sets (saturation current, Ohmic resistance, and zero-bias junction capacitance) in Tables II and I are used as the input parameters for the minidiode (in the new diode unit) and capsuled diode module (in the prototype diode unit), respectively.

Figure 12 presents the simulation setup, where the upper-left and the upper-right panels show the electric circuit models with and without the diode units, respectively; the lower-left and the lower-right panels show the three-dimensional models for the new-diode unit and the prototype diode unit, respectively. In the lower-left panel (new-diode unit), we assume $R = 0.01\ \Omega$, $C = 1.74 \times 10^{-10}\ F$, and $I0 = 5.58 \times 10^{-8}$ A, as the "parameters" of the minidiode in CST STUDIO©. Similarly, $R = 0.01\ \Omega$, $C = 1.52 \times 10^{-9}\ F$, and $I0 = 2.04 \times 10^{-6}$ A are taken as the parameters of the "prototype diode module with the black capsule" in the lower-right panel (prototype diode unit). Note that the functioning of the PFLs (composed of 110-m coaxial cables in Fig. 2) is largely overlooked because CST STUDIO© can set only three types of excitation sources (voltage, current, and power signals) as the input parameters in the electric circuit simulation part in a straightforward manner [22], and 110-m coaxial cables cannot be set to be charged as an initial condition (note 110-m long cables in Fig. 12 are dummy cables, not the PFLs). Besides, the end-clippers cannot be modeled behind the power supply, which is another drawback of three-dimensional simulations with CST STUDIO©.

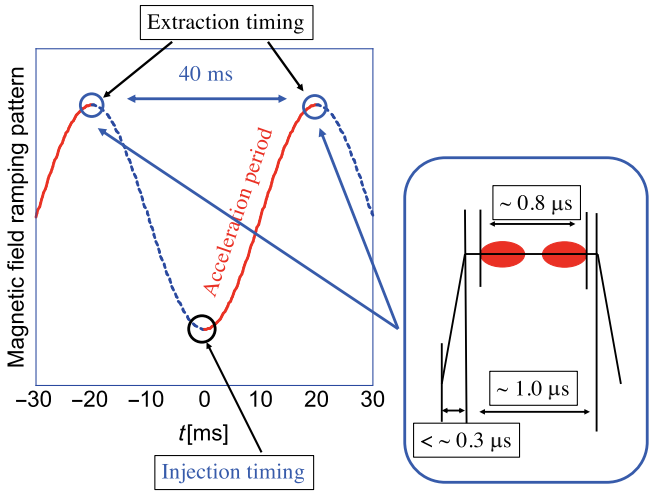

FIG. 11. The ramping pattern of the RCS and the excitation pattern of the magnetic field of the extraction kicker [9].

Three-dimensional simulations are performed, and Fig. 13 presents the overview (left) and the magnified figure (center) around the rising edge of the first pulse current observed at the position labeled "A" in Fig. 2, where the blue and the red lines show the results obtained for the newly designed diode unit and the prototype diode unit, respectively, and the black line shows the reference results without any diode unit. The right panel shows the result with the new diode units subtracting the result with the prototype diode units.

In the left panel, the reflection currents from the electric power supply are superposed owing to the lack of end-clippers. Then, we focus on the behavior of the first pulse from now on in this simulation.

In the center panel, the current waveform rises sharply because we neglect the effect of the PFLs comprising coaxial cables as the charging unit by simply inputting the trapezoidal waveform with ~25 ns rise time (refer to

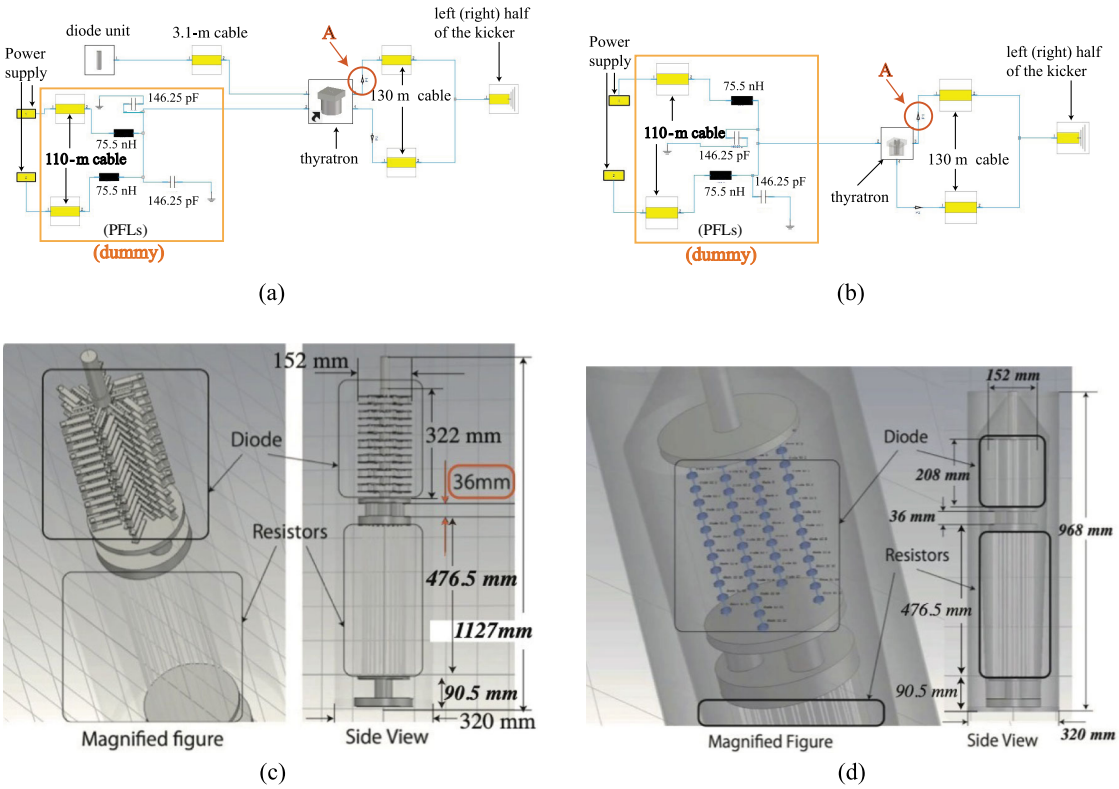

FIG. 12. Simulation setup. (a) Electric circuit model with the diode unit. The location "A," which is identical to that in Fig. 2, shows the current monitoring point. (b) Electric circuit model without the diode unit. The location "A", which is identical to that in Fig.1, shows the current monitoring point. (c) Three-dimensional model for the new diode unit. (d) Three-dimensional model for the prototype diode unit.

Table I in [9]) into the power supply in Fig. 12. We can identify a slightly damped oscillation around the rising edge of the current waveform even for the case without a diode unit (black), which can be found in the measured result (red) in Fig. 10, because of the PFLs and thyratron between the power supply and the monitored position "A" in the panel (b) of Fig. 12.

The remarkable oscillation amplitudes obtained for both the new and the prototype diode units are relatively the same, the difference being within ±0.13 kA and the same order of magnitude as the measured data in Fig. 9 so that the bunch-by-bunch trajectory of the extraction beams can be stabilized following the procedure illustrated in Sec. VIII B. From this simulation and measurements (see Fig. 9) points of view, the strategy for decomposing the diode modules into minidiodes seems effective in producing a new diode module equivalent to the prototype diode unit.

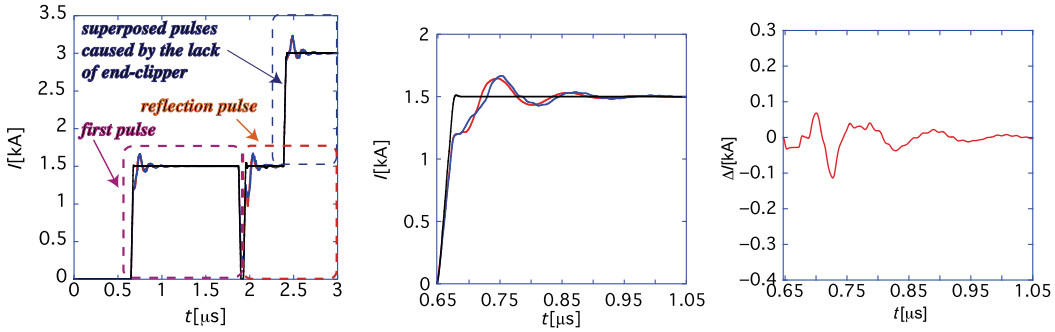

FIG. 13. Three-dimensional simulations. The overview (left) and the magnified figure (center) around the rising edge of the first pulse current observed at the position labeled "A" in Fig. 12 (Figs. 1 or 2), where the blue and the red lines show the results with the new and the prototype diode units, respectively, and the black line shows the reference results obtained without any diode units. The right panel shows the result with the new diode units subtracting the result with the prototype diode units.

Here, the other drawback was encountered for full three-dimensional simulation performed using CST STUDIO© combined with electric circuit simulation, when we consider the case where nonlinear devices are distributed in the simulation setup like the kicker system of RCS including diode units and end-clippers. That is, three-dimensional simulations must be executed by choosing one of the parts that includes these devices (the diode unit part in Fig. 12 in this case) as the main platform, while the other parts are "manually" assigned to the electric circuit part in CST STUDIO©. This means that the three-dimensional models including nonlinear devices such as end-clippers and diode units are not "automatically" described in terms of electric circuit theory when they are assigned to the electric circuit part in CST STUDIO© during the simulation process.

Hence, it is quite helpful to us to identify SPICE© parameters, in advance, that describe the kicker and the diode units. Therefore, in the next section, we search for suitable parameters for them used in the SPICE© simulation in this report.

IV. MEASUREMENTS AND SPICE© SIMULATIONS OF CURRENTS AND VOLTAGES EXCITED BY THE PFLs

We try to identify suitable SPICE© parameters for describing the kicker and the diode units used in electric circuit simulations. For the magnet part, previous studies have proposed electric expressions [23], while we found that the diode unit can be described by a series circuit of a 1.18-μH inductor and the diode by the SPICE© parameter provided in Table III, where the inductive effect, resulting from the structure of the diode unit (see Fig. 6), is included.

TABLE III. The diode in Fig. 2, consisting of 30 parallel and 27 series minidiodes and 6 parallel and 27 series 1000 pF capacitors, is effectively represented by a series circuit of a 1.18-μH inductor and the diode with SPICE© parameter given by the present parameters.

Parameters	Units	Value
Saturation current	A	5.0×10^{-12}
Ohmic resistance	Ω	0.2
Emission coefficient	···	2.55
Transit time	*s*	1.0×10^{-6}
Zero-bias junction capacitance	F	0.415×10^{-9}
Junction Potential	V	1
Grading coefficient	···	0.5
Action Energy	eV	1.11
Saturation current Temperature exponent	···	3
Flicker noise coefficient	···	0
Flicker noise exponent	···	1
Coefficient for forward-bias	···	0.5
Reverse breakdown voltage	V	54000
Current at breakdown voltage	A	1.0×10^{-10}
Normal temperature	°C	25

In this section, we determine the reliability of the expressions for the magnet and the diode unit by conducting SPICE© simulations and comparing the results with the measurements. This SPICE© simulation setup enables us to use the PFLs as a charging unit and comprehensively deal with the whole kicker system including the end-clippers, the PFLs, the kicker magnets, and the diode units.

A. The case of the present kicker without a diode unit

First, we consider the whole present kicker system without a diode unit. The upper panel of Fig. 14 effectively represents the left (right) half of the kicker magnet in terms of the electrical equivalent model [23] and the lower panel represents the simulation setup for the present kicker powered by the PFLs.

Figures 15 and 16 show the simulation results and the measurement results for the present kicker, respectively. To observe the currents of the end-clipper, a current transformer is placed behind the matched load (20 Ω) of the end-clipper in the direction displaying positive when they flow from 20 Ω resistor to the diode. The left panels show the current waveform at the position designated "A" in Fig. 1, and the right panels show the current at the end-clipper. The first and second trapezoidal current waveforms in the left panels represent the forward current from the PFL and the reflection current from the kicker magnet, respectively. The right panels demonstrate that the diode of the end-clipper successfully blocks the initial pulse with positive polarity (dc current) from 110-m long PFL to produce the forward current to the kicker, while permitting the reflection current from the kicker with negative polarity to flow and be absorbed into the matched load behind the diode of the end-clipper.

The center panels in Figs. 15 and 16 represent the magnified figures around the rising edge of the forward current waveform in the left panels. Though the minor damped oscillation in the measurement cannot be described in the simulation, the SPICE© simulation well describes the 100-ns transient rising time, which is quite different from the black line in the right of Fig. 13 obtained from three-dimensional simulations with CST STUDIO©, because a simple trapezoidal waveform is just used as the input parameter. Therefore, SPICE© simulations, coping with this effect, are preferable to CST STUDIO© simulations.

The results of the simulations without the diode unit are fairly consistent with those of the measurements. Here, note that the impedance matching errors in the whole kicker system increase the enhancement of the current waveform in the measurements by ∼10% (from 1.5 to 1.62 kA). Furthermore, the circuit model of the kicker magnet creates a bit sharper peaks at the edge on the reflection current monitored at position "A" and at the end-clipper than those on the measured reflection current. Although these discrepancies should be noted, the proposed electric circuit

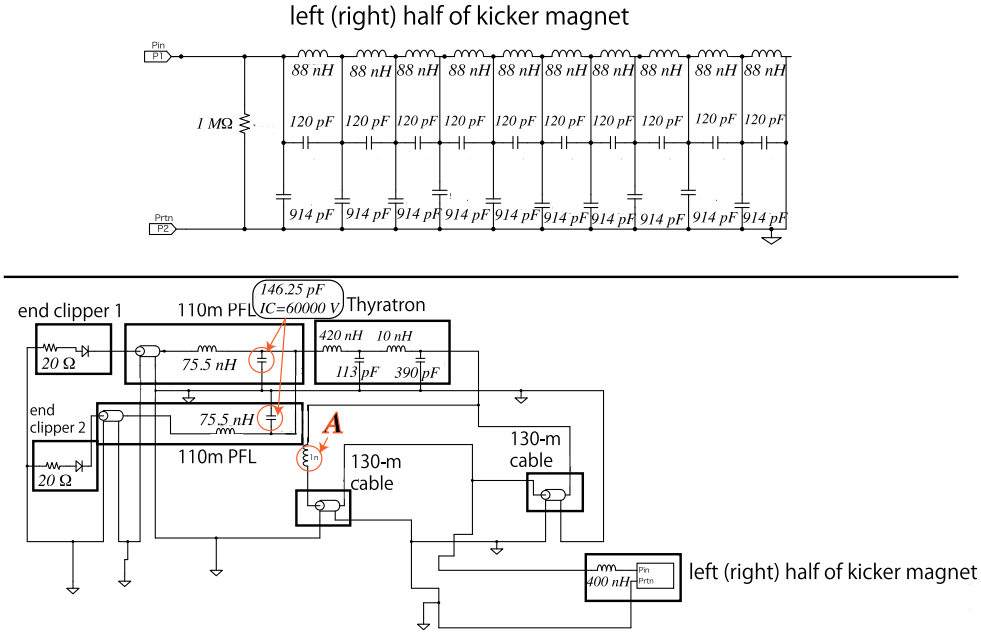

FIG. 14. Simulation setup (by SPICE©) without diode units. The upper panel effectively represents the left (right) half of the kicker magnet. The location "A," which is identical to that in Fig. 1, shows the current monitoring point.

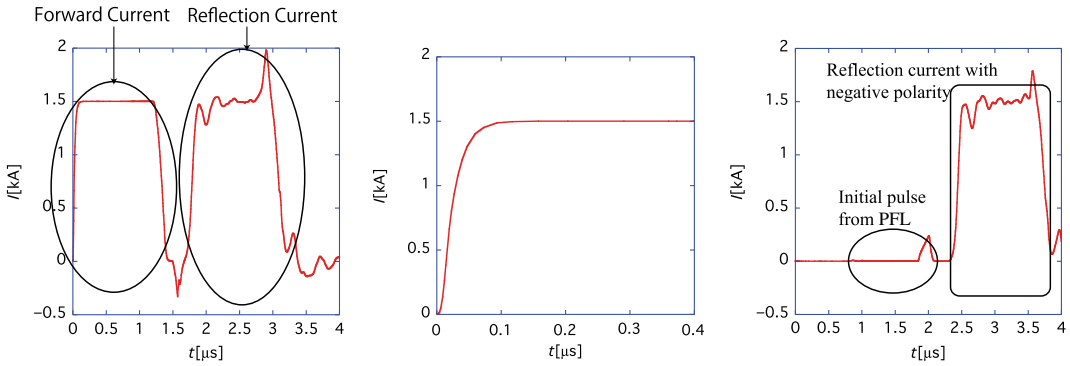

FIG. 15. SPICE© simulations without diode units. The left panel shows the current waveform at the position labeled "A" in Fig. 14 (Fig. 1), and the right panel shows the current at the end-clipper. The center panel represents the magnified figure around the rising edge of the forward current in the left panel.

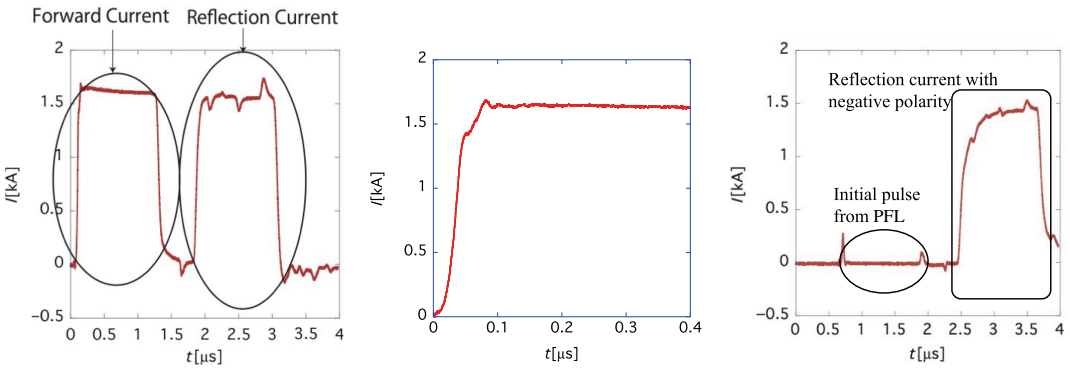

FIG. 16. Measurements without diode units. The left panel shows the current waveform at the position labeled "A" in Fig. 1, and the right panel shows the current at the end-clipper. The center panel represents the magnified figure around the rising edge of the forward current in the left panel.

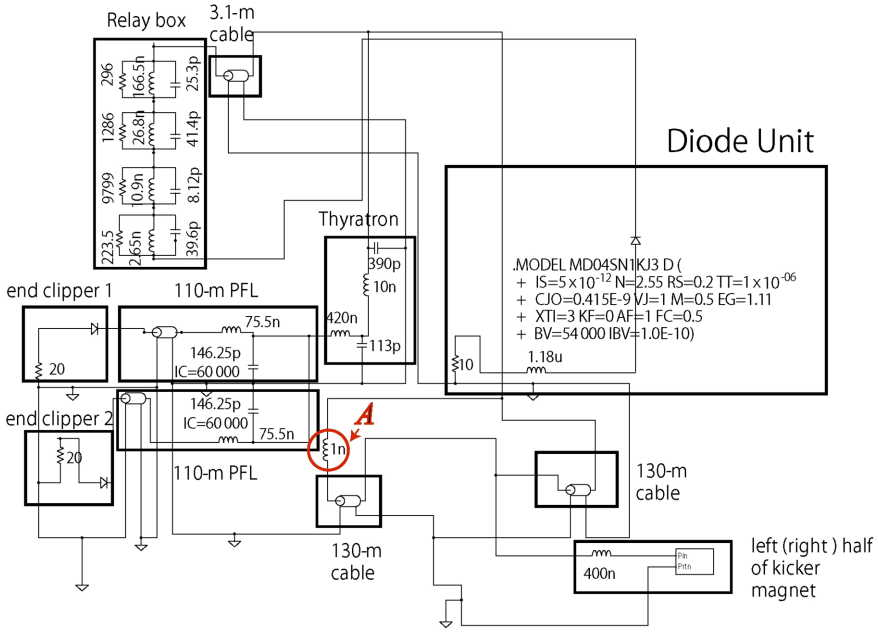

FIG. 17. Simulation setup with the diode unit by SPICE©. The location "A," which is identical to that in Fig. 2, shows the current monitoring point.

model in Fig. 14 sufficiently well describes the characteristics of the whole kicker system and enables us to estimate the power consumption due to the kicker appropriately, which is illustrated by using the kicker with diode unit in the next Sec. IV B.

B. The case of kicker with diode unit

We also simulate the case involving the new diode unit. Figure 17 describes the circuit model of the kicker magnet with the new diode unit, where the upper panel of Fig. 14 is substituted into "the left (right) half of the kicker magnet" in Fig. 17.

Figure 18 provides an overview of the current waveform in a longer time range (than previously considered time ranges), which is important for evaluating (from a design point of view) the heating rate caused by the diode unit. This rate is associated with the impedance mismatch created after the unit is attached to the kicker in addition to the end-clippers.

The left and the right panels show the SPICE© simulation and measurement results, respectively. The red and blue lines in the right panel denote the current waveforms associated with diode unit 1 and diode unit 2, respectively. The results demonstrate the high reproducibility of the diode unit, indicating that the fabrication process of the diode unit satisfying the specification is now established in principle. The overall behavior is well explained by the SPICE© simulations, although the simulations create a bit sharper peaks at the edge of the reflection current wave than that on the measured waveform, similar to the case without the diode unit.

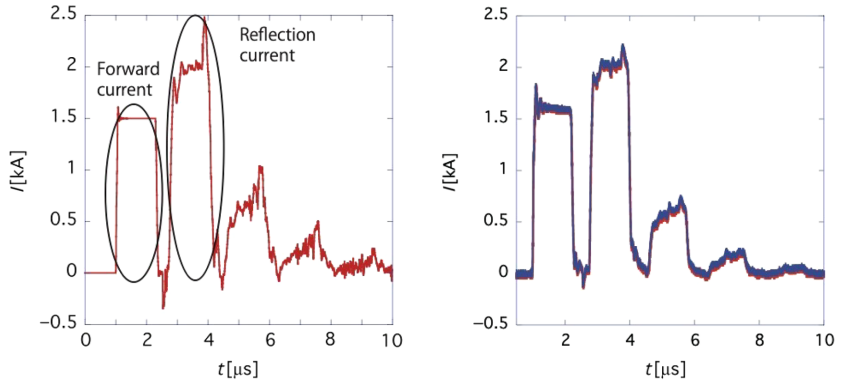

FIG. 18. The results obtained for simulations (left) and measurements (right) of the current waveform at "A" in Fig. 17 (Fig. 2) when the diode unit is attached to the thyratron container via a 3.1-m coaxial cable. The red and blue lines in the right panel denote the current waveforms with diode unit 1 and diode unit 2, respectively.

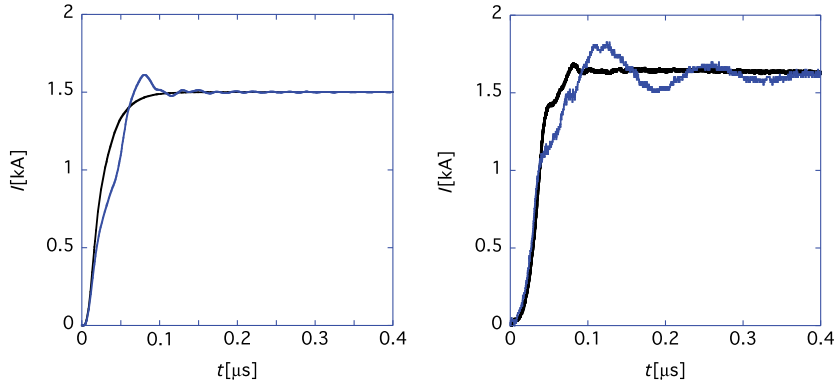

FIG. 19. Results of SPICE© simulations (left) and measurements (right) around the rising edge of the current waveforms. The blue line shows the result with the new diode unit, and the black line shows the reference result obtained without the diode unit.

When no diode unit is employed, the end-clipper can perfectly absorb the reflection current. However, the impedance mismatch resulting from the diode unit excites the subsequent lingering currents for the waveform. Though this may seem to be a drawback, the RCS is operated at a 25-Hz repetition rate with a 20-ms ramping time, as shown in Fig. 11. In other words, the subsequent beam pulse is injected into the RCS 20 ms after the previous beam is extracted, which is sufficient for damping the (∼10 μs) trapezoidal lingering currents. In the end, the diode unit causes no problems in the machine like the RCS.

Figure 19 shows the results of SPICE© simulations (left) and measurements (right) around the rising edge of the current waveforms. The blue lines show the results obtained with the diode unit, and the black lines show the reference results obtained without the unit. The simulations underestimate the measurements by ∼10% (as in the case without the diode unit), owing to imperfect impedance matching of the real kicker. The new diode unit can be relatively well modeled by the series circuit of a 1.18-μH inductor and a diode with the SPICE© parameter provided in Table III because the oscillation amplitude becomes comparable to the measurements by taking into account the 10% enhancement.

Figure 20 shows simulations with the improved diode unit by SPICE©, revealing that the oscillation amplitudes dependence of the 20-Ω coaxial cable connecting the thyratron and the diode unit on the cable length. The black line shows the case without the diode unit. The blue solid line, green solid line, red solid line, and purple dashed line correspond to the cases of 3.1, 2.6, 2, and 1 m, respectively. Hence, we determined that the oscillation on the rising edge in Fig. 10 is caused by a 3.1-m long 20-Ω coaxial cable [10] connecting the diode unit to the thyratron [14]. The simulation results suggest that negligible oscillation on the currents can be achieved for cable lengths lower than 2 m. Furthermore, housing the diode unit and the thyratron in the same oil tank would be better than using separate tanks when the proposed scheme is implemented for suppressing the kicker impedance from the very beginning of the construction phase.

The oscillation effect on the extraction beams from the RCS seems significant from a view point of only the observation of waveform currents. However, the effect is modest, as discussed in Sec. VIII B from view points of simulating the magnetic field and the direct measurements of extraction beams.

In the present measurement, the voltage probe and the current transformer are attached to the diode unit, which enables us to directly observe the current and the voltage across the units. The left panel of Fig. 21 shows the results obtained from the SPICE© simulation of the currents on the diode units; the measurement results are shown in the right panel. The red and blue lines in the right panel denote the current on diode unit 1 and the current on diode unit 2, respectively. These lines overlap almost completely,

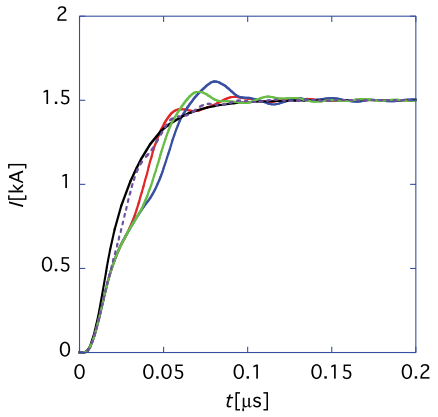

FIG. 20. The 20-Ω coaxial cable length dependence of the oscillation amplitudes on the current waveform at "A" in Fig. 17 (Fig. 2) with the improved diode unit (simulations). The black line shows the case without the diode unit. The blue solid line, green solid line, red solid line, and purple dashed line correspond to the cases of 3.1, 2.6, 2, and 1 m, respectively.

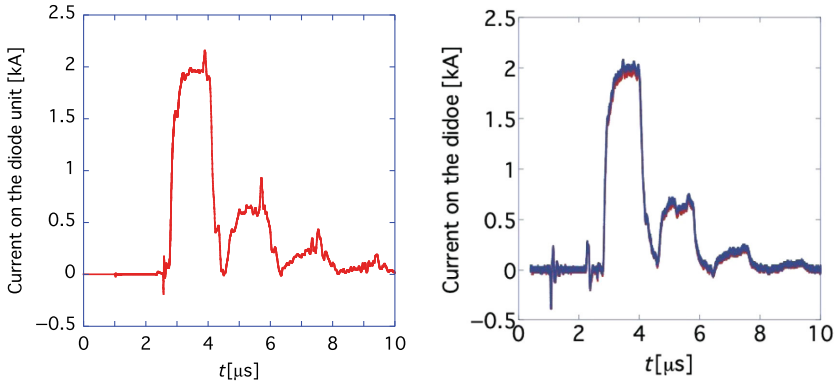

FIG. 21. The simulation (left) and the measurement (right) results of the current on the diode unit. The red and blue lines in the right panel denote the currents on diode unit 1 and diode unit 2, respectively.

reiterating that two diode units are fabricated with good accuracy.

The measurement results reveal that no current flows on the diode unit during the passage of the forward current except during the rise and fall periods of the current waveforms. The high-frequency components can flow more through the diode units than in the simulation case. In other words, we expect that the measured beam impedance could be lower than that determined by the simulations. The measured result demonstrates that the new diode has sufficient withstand voltage against the induced voltage because no "dc" current flows on the diode when the forward current passes to the kicker magnet.

The above observation that the withstand voltage of the diode units is sufficient is more directly demonstrated in Fig. 22. The left and the right panels in Fig. 22 show the simulated voltage across the diode unit and the measurement results. Although a good agreement for its overall behavior is obtained between the results, being consistent with the results shown in Fig. 21, we see that the measured maximum surge voltage is higher than the simulated value of around 1 μs, which is a transient effect during the passage of the forward current. Obtaining an accurate estimate of the transient effect was difficult for us, owing to the unknown floating inductance and capacitance in the real whole setup of the kicker. Therefore, confirmation, via measurements, that the diode unit has sufficient withstand voltage during the transient time is important for the practical use of the diode unit.

In the present measurement, we observed the current on the diode unit and the voltage across the diode unit simultaneously. Hence, based on the measurements, we can directly calculate the amount of electric power generated in the unit by using the right panels of Figs. 21 and 22 and compare it with the simulations calculated by using the left panels of them.

Let us calculate

$$P(t) = \frac{1}{0.040}\int_0^t dt'[-I(t')] \times V(t'), \tag{3}$$

for the total diode unit (the sign of the observed current must be opposite due to the setup of the current transformer in the relay box; refer to Sec. III) and

$$P(t) = \frac{1}{0.040}\int_0^t dt' 10 \times I(t')^2, \tag{4}$$

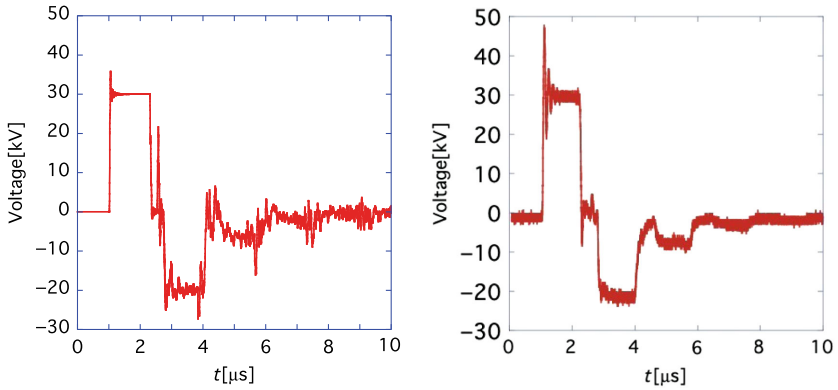

FIG. 22. The left and the right panels show the results of simulations and measurements, respectively, of diode unit 1.

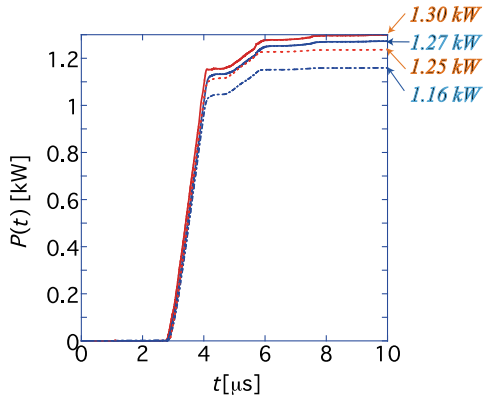

FIG. 23. Electric power generated in the diode unit (red) and the 10-Ω resistor part only (blue). The dashed and the solid lines represent the results by measurements and simulations.

for 10-Ω resistor part only. The red and blue lines in Fig. 23 denote the results for the total diode unit and only the 10-Ω resistor part, respectively. The dashed and the solid lines represent the estimates by measurements and simulations, where the values are saturated at $t = 10$ μs. With a repetition rate of 25 Hz, the amount of electric power generated in the unit is about 1.25 kW by measurements and about 1.3 kW by simulations, which are estimated after $t = 10$ μs is plugged into Eq. (3). Though the transient peaks of the measured voltage for the first pulse are higher than those for the simulated one in Fig. 22, the main contribution to the power consumption is from the reflection pulse since the diode unit successfully blocks the forward current from flowing into the unit. In the end, the estimate by the measurement is smaller than that by the simulation. One of the main purposes of the simulation study is to determine the power consumption rate (with high accuracy) from a design point of view. Therefore, we conclude that we have successfully established a simulation model within $5\% = (1 - 1.25/1.3)$ accuracy from a practical point of view.

We will investigate the durability of the diodes and resistors from a thermohydrodynamic point of view in Sec. V. For this investigation, we divide the measured 1.25 kW into the power consumption of the resistors and the consumption of the diodes. The contribution from the resistor is estimated as 1.16 kW based on the fact that the total resistor in the diode unit is 10 Ω, and thus, the contribution from the diode stack is estimated as 0.09 kW.

For the durability test of the diode units, we operated the kicker continuously for 12 days with a repetition rate of 25 Hz. The left panel in Fig. 24 shows the current waveform observed at "A" in Fig. 2 from day to day. The red, blue, green, black, pink, light blue, and yellow colors denote the data obtained on February 15–19, 2021, February 22, 2021, and February 24, 2021, respectively. The right panel in Fig. 24 shows the current waveforms observed on February 16, 2021 (blue), February 17, 2021 (green), February 18, 2021 (black), February 19, 2021 (pink), February 22, 2021 (light blue), and February 24, 2021 (yellow) subtracting the one observed on February 15, 2021, effectively representing the difference of current from day to day. As the output current waveform is stably produced for 12 days, the results demonstrate that the diode unit is of use from a practical point of view.

Note that we cannot precisely observe the current below ±0.05 kA accuracy in these measurements as found in the right panel, because the fluctuation of current with at most amplitude 0.05 kA was detected even before 1 μs when no current should flow. Nonetheless, the result demonstrates that the significant modulation of the current waveform could occur within ±0.1 kA at

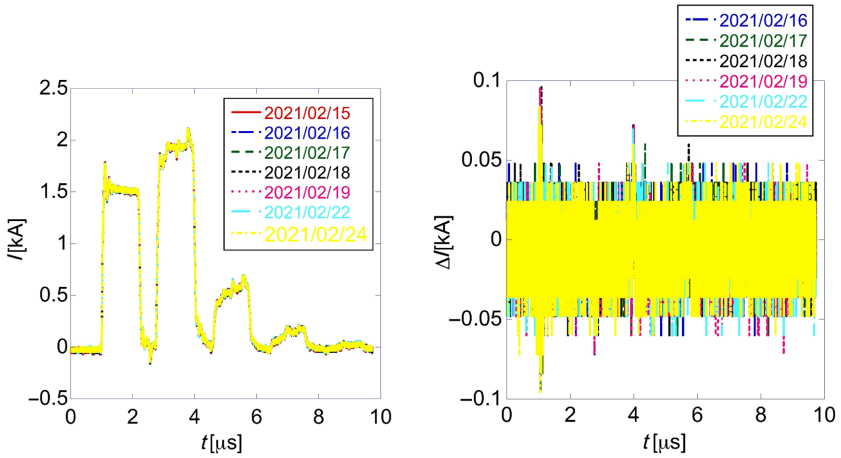

FIG. 24. The measured current waveform observed at "A" in Fig. 2 from day to day (left), and the respective values subtracting the data measured on February 15, 2021 (right).

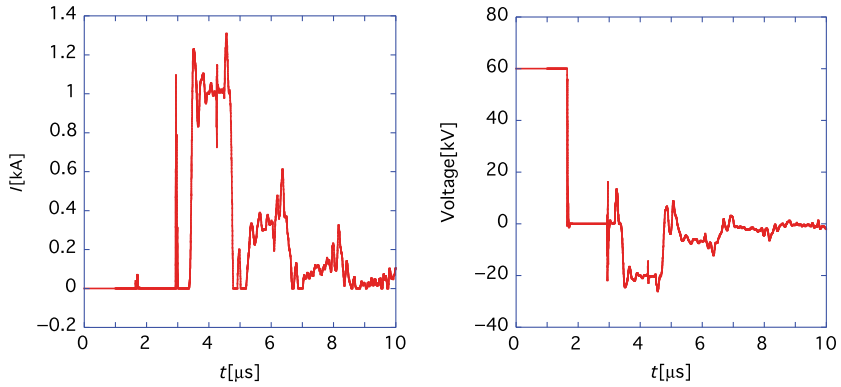

FIG. 25. Simulation results of the current (left) and the voltage (right) on the end-clipper.

the rising edge of the forward current, which is the same order of magnitude as the difference of measured currents in Fig. 9 for the prototype and newly developed diode units. In other words, when we focus only on the flattop region, we can judge that the difference between the currents day to day is within the same current oscillation level of the present kicker without the diode unit. In Sec. VIII B, we will describe that the modulation at the rising edge of the current day-to-day is not so effective on the trajectory of the extracted beam from the RCS (or the magnetic field in the kicker) from analytical and measurement points of view.

Finally, let us numerically estimate the power consumption generated by the end-clipper. It is impossible to directly measure it because no special voltage probe like in the diode unit is installed in any present end-clipper at the RCS. Meanwhile, since the initial charging voltage is set to 60 kV in PFLs in Fig. 17 (and reality), it is apparent that the end-clippers have sufficient withstand voltage beyond 60 kV, though no voltage has been observed across the end-clipper. In detail, the simulations based on this circuit model provide the current and voltage on the end-clipper, as shown in Fig. 25. The power consumption can be estimated as $W \simeq 0.8$ kW with a 25-Hz repetition rate as done in the diode unit. In Sec. VI, we can see that the estimated power consumption is consistent with the measured heating rate of the end-clipper, indirectly demonstrating the effectiveness of this SPICE© model.

Overall, the SPICE© simulation circuit model can fairly describe the characteristics of the whole kicker system comprehensively, including the end-clippers, the PFLs, the kicker magnets, and the diode units, in the RCS. From here on, we model the new diode unit as a series circuit of a 1.18-μH inductor and a diode with the SPICE© parameter shown in Table III. Some numerical examples obtained by SPICE© in combination with CST STUDIO© are further shown in the figures in the following sections. However, note that we need to take special care of the simulation results when the high-frequency behavior plays an important role in some analyses, paying attention to no end-clipper being implemented in the simulation model.

V. SUPPRESSION OF HEATING RATE OF THE DIODE UNITS UNDER CONTINUOUS KICKER OPERATION

We also investigate the surface temperature of the diodes and the resistors to avoid malfunctioning of the diode unit. Under the present specification, the maximum temperature can be 150 °C for the resistors because the metal fittings on both ends of the resistor are fixed with lead-free solder, while the limit temperature for the diodes is 85 °C as determined by the terminal conditions on the diode.

Figure 26 presents an overview of the oil-flow transport path, where the oil flow is $\mathbb{V} = 6.5$ L/ min in the oil tank containing the diode unit. As previously observed in Fig. 7, the inlet of the oil is placed on the bottom of the oil tank, and the outlet of the oil is placed on the upper part of the oil tank. The insulating oil is used to cool the diode units, thyratrons, and end-clippers. A filter is installed on the downstream side of the oil circulation system in case the diodes are scrapped due to the heating.

A. Analytical evaluation of temperature rises on the diodes and the resistors

Here, we estimate, in an analytical manner, the temperature rise of diodes and the resistors, when the kicker functions with a repetition of 25 Hz. When the contribution from the beam-induced currents is assumed to be neglected (the contribution from beams to the diode unit is around 5% even in the 1-MW case, as shown in Table V in Sec. VII), we estimate that the consumed electric power due to the 10-Ω resistor is 1.16 kW and the power due to the diode is 0.09 kW (see Sec. IV).

The center panel of Fig. 27 shows the details of the diode unit, where 25 cylindrical resistors with a diameter $d_R =$ 15 mm and length $l_R = 0.455$ m (see right panel) are cylindrically placed with its diameter $D_i = 0.137$ m.

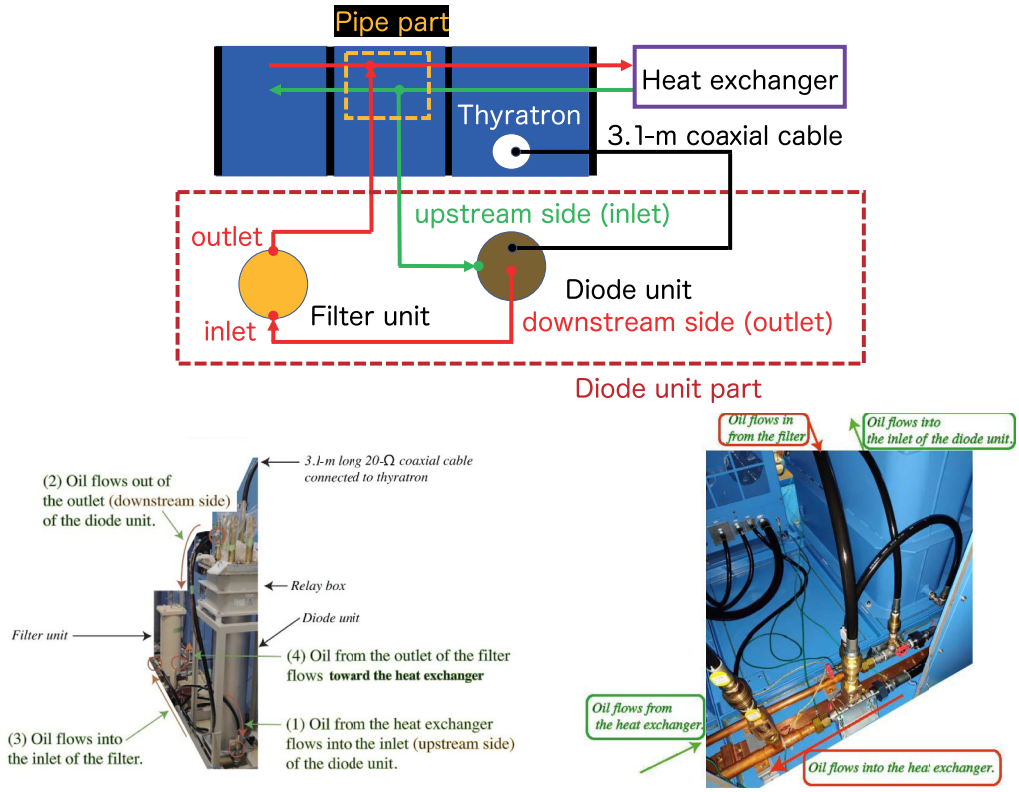

(a) Diode unit part. (b) Pipe part.

FIG. 26. Overview (top) of the oil circulation system for cooling of the diode unit: the transport path of the insulating oil used to cool the diode units. (a) and (b) panels show the magnified figures of the "diode unit part" and the "pipe part" in the top panel, respectively.

There are 25 gaps between the cylindrical resistors. As the left panel shows, holes with a 10-mm diameter are placed on the upper plate on the resistor part and the lower plate on the bottom part of the diode part to secure the oil flow.

Figure 28 shows the oil flow in the diode unit (which was simulated by ANSYS FLUENT© [24]). The diameters of the inlet and the outlet of the oil tank are 27 and 30 mm, respectively.

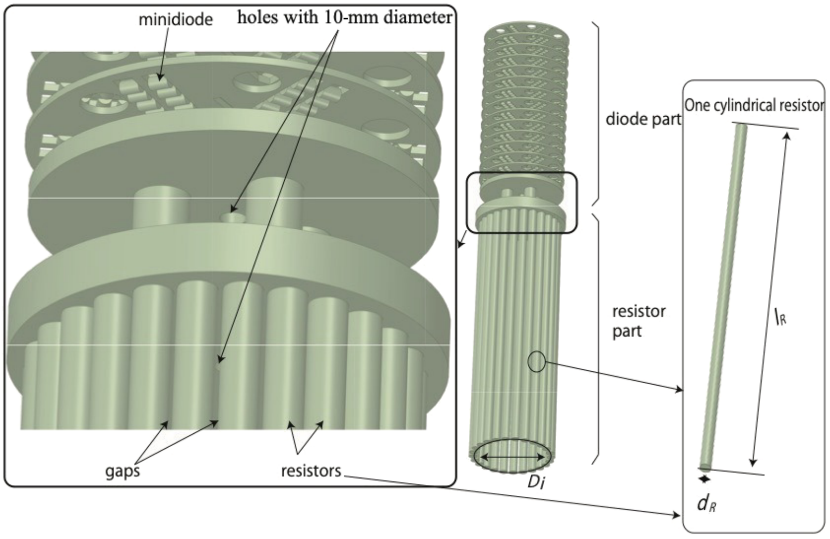

FIG. 27. A schematic of the diode unit (center). The resistor part consists of 25 cylindrical resistors, which are cylindrically aligned with the diameter $D_i = 0.137$ m. One cylindrical resistor with diameter $d_R = 15$ mm and length $l_R = 0.455$ m is shown in the right picture. To secure the oil flow, holes with 10 mm diameter are placed on the upper plate on the resistor part and the lower plate comprising the bottom part of the diode part (see the left panel).

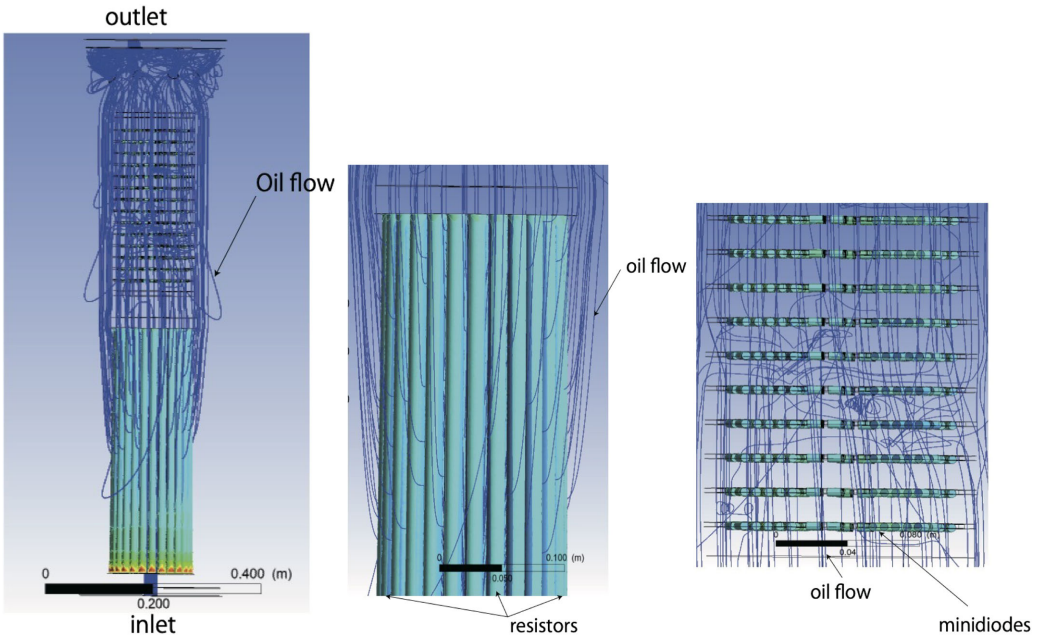

FIG. 28. Overview of the oil flow in the diode unit (left), high-magnification view of the region around the upper part of the resistor part (center), and the region around the lower part of the diode part (right). The diameters of the inlet and the outlet are 27 and 30 mm, respectively.

The surface temperature T_R of the respective cylindrical resistor can be calculated from Newton's law of cooling, which is given as follows,

$$T_R = T_o + \frac{w_R}{h l_R \pi d_R \times 10^{-3}}, \tag{5}$$

where T_o is the temperature of the surrounding oil, h is the heat transfer coefficient, and w_R is the heating rate due to a cylindrical resistor. The heat transfer coefficient h is estimated from the thermal conductivity λ and Nusselt number Nu_D for the assumed Reynolds number Re_D and Prandtl number Pr [25].

A Shin-Etsu Chemical silicon oil (KF-96-20CS) with properties given in Table IV [26], was used for cooling. A somewhat large Prandtl number of $\mathrm{Pr} \sim 170$ is evaluated for the oil temperature $T_o \sim 308.7$ K, as seen in Sec. VI. This value suggests that the thermal boundary layer is close to the heating object. Accordingly, the oil flow in the oil tank can be simplified as an "external flow" in the lowest order approximation.

Referring to the center panel of Fig. 28, let us consider the case where the oil flows through 25 gaps between the resistors. The velocity V_R of the oil flow in the gap (between the resistors) is then roughly estimated as follows:

$$60 \times 1000 \times (\pi D_i - 25 \times d_R \times 10^{-3}) \times l_R V_R = \mathbb{V}. \tag{6}$$

This equation yields $V_R = 0.0043$ (m/s) for an oil flow of $\mathbb{V} = 6.5$ L/min in the oil tank. Hence, the local Reynolds number $\mathrm{Re_D}$ associated with one cylindrical resistor is calculated as follows:

$$\mathrm{Re_D} = \frac{V_R d_R \times 10^{-3}}{\nu} = \frac{0.0043 \times 15 \times 10^{-3}}{17 \times 10^{-6}} \simeq 3.8, \tag{7}$$

where we use $\nu = 17 \times 10^{-6}$ m^2/s, suggesting a laminar flow because the value is lower than 2300.

Churchill-Bernstein proposed a formula for the Nusselt number $\mathrm{Nu_D}$ for $\mathrm{Pr} \cdot \mathrm{Re_D} \geq 0.2$ [27], i.e.,

TABLE IV. Temperature dependence exhibited by kinematic viscosity ν, density ρ, isobaric specific heat c_p, thermal conductivity λ, and Prandtl number Pr of Shin-Etsu Chemical silicon oil (KF-96-20CS) [26].

T (K)	ν (m^2/s)	ρ (kg/m^3)	c_p (kJ/kg K)	λ (W/mK)	$\eta = \rho\nu$ (Ps s)	$\mathrm{Pr} = \eta c_p 10^3/\lambda$
298	20×10^{-6}	950	1.6	0.15	0.019	202
323	13×10^{-6}	930	⋯	⋯	0.01209	128

$$\mathrm{Nu_D} = \frac{h d_R \times 10^{-3}}{\lambda} = 0.3 + \frac{0.62 \mathrm{Re}_D^{\frac{1}{2}} \mathrm{Pr}^{\frac{1}{3}}}{[1+(0.4/\mathrm{Pr})^{\frac{2}{3}}]^{\frac{1}{4}}} \left[1 + \left(\frac{\mathrm{Re}_D}{282000}\right)^{\frac{5}{8}}\right]^{\frac{4}{5}} \simeq 7, \quad (8)$$

which means that the heat transfer coefficient h is reversely calculated as

$$h = \frac{7\lambda}{d_R \times 10^{-3}} = 70 \ [\mathrm{W/m^2\,K}], \quad (9)$$

by identifying the second formula in Eq. (8) with the numerical value of $\mathrm{Nu_D} \simeq 7$, where we take $\mathrm{Pr} = 170$ and $\lambda = 0.15$ W/mK.

Hence, the heating rate w_R contributed from one cylindrical resistor is estimated as follows:

$$w_R = \frac{1160}{25} = 46.4[W], \quad (10)$$

when the total heating rate owing to 10 Ω is 1.16 kW. Finally, the surface temperature T_R of the cylindrical resistor can be calculated from Eq. (5) as follows:

$$T_R = T_o + \frac{w_R}{h l_R \pi d_R \times 10^{-3}} = T_o + 31. \quad (11)$$

The estimation suggests that the surface temperature of the cylindrical resistor could rise by 31 °C relative to the temperature of the surrounding oil. For example, when the temperature of the oil reaches 40 °C, this rough estimation suggests that the surface of the resistor could be 71 °C, which is sufficiently below the specification for the temperature of the cylindrical resistor (150 °C).

We also estimate the surface temperature of the minidiode, which is cylindrical in shape with $D_d (= 5.4\ \mathrm{mm}) \times l_d (= 7.6\ \mathrm{mm})$. The diode part consists of 30 parallel and 27 series of minidiodes. Hence, the heating rate iv due to one minidiode is calculated as

$$iv = \frac{90}{30 \times 27} = 0.1 \ [\mathrm{W}], \quad (12)$$

where we assume that the total heating rate due to the total diode part is 90 W.

Referring to the right panel of Fig. 28, the assumption is made that the minidiode is placed perpendicular with respect to the oil flow V_m, which is roughly estimated as

$$60 \times 1000 \pi \frac{D^2}{4} V_m = \mathbb{V} (= 6.5\ \mathrm{L/\,min}), \quad (13)$$

resulting in

$$V_m = 0.003 \ [\mathrm{m/s}], \quad (14)$$

where $D = 0.214$ m is the diameter of the oil tank. Accordingly, the local Reynolds number $\mathrm{Re_D}$ around one cylindrical minidiode is calculated as follows:

$$\mathrm{Re_D} = \frac{V_m D_d \times 10^{-3}}{\nu} = \frac{0.003 \times 5.4 \times 10^{-3}}{17 \times 10^{-6}} = 0.95, \quad (15)$$

where we use $\nu = 17 \times 10^{-6}\ \mathrm{m^2/s}$, suggesting a laminar flow because the value is lower than 2300.

The Nusselt number associated with $\mathrm{Pr} \cdot \mathrm{Re_D} \geq 0.2$ and, hence the heat transfer coefficient h is calculated as follows:

$$h = \frac{\lambda 3.63}{D_d \times 10^{-3}} \simeq 100 \ [\mathrm{W/m^2\,K}], \quad (16)$$

with $\lambda = 0.15$ W/m K, because

$$\mathrm{Nu_D} = \frac{h D_d \times 10^{-3}}{\lambda} = 0.3 + \frac{0.62 \mathrm{Re_D}^{\frac{1}{2}} \mathrm{Pr}^{\frac{1}{3}}}{[1+(0.4/\mathrm{Pr})^{\frac{2}{3}}]^{\frac{1}{4}}} \left[1 + \left(\frac{\mathrm{Re_D}}{282000}\right)^{\frac{5}{8}}\right]^{\frac{4}{5}} \simeq 3.63. \quad (17)$$

Finally, the surface temperature T_d of the cylindrical minidiode is evaluated as follows:

$$T_d = T_o + \frac{iv}{h l_d \times 10^{-3} \pi D_d \times 10^{-3}} = T_o + 7.75. \quad (18)$$

Hence, if the temperature of oil reaches 40 °C, the surface of the minidiode could be roughly 47.75 °C, which is sufficiently lower than the temperature specification of the minidiode (85 °C).

In the lowest order approximation, all analytical estimations suggest that an oil flow of 6.5 L/ min yields sufficient cooling of the respective diodes and the resistors. In the next Sec. V B, we will investigate the details of the cooling efficiency by performing simulations.

B. Numerical analysis

For more rigorous estimations than those achieved via the analytical method, numerical simulation is executed by using ANSYS FLUENT©. The structure of the diode unit is similar to that of a Pin Pitch Heat Sink, though analytical estimates in Sec. V A indicate that the overall flow of oil is close to a laminar flow. Hence, the oil flow is analyzed in detail based on the "k-ϵ with RNG model" [28,29] in ANSYS FLUENT©. This method is employed based on its applicability to cases where the flow becomes turbulent only near a structure and becomes relaminarized after passing through the structure. Such flow behavior could occur not only around the diodes and the resistors but also

around the holes where the flux is changing due to the geometry change.

We take the following as the properties of the oil, density $\rho = 941$ kg/m^3, isobaric specific heat $c_p = 1600$ J/kg K, thermal conductivity $\lambda = 0.15$ W/mK, and viscosity $\eta = 0.016$ kg/m s (see Table IV). For the properties of the metal part comprising the diode unit, we use $\rho = 7930$ kg/m^3, $c_p = 590$ J/kg K, and $\lambda = 16.7$ W/mK based on the properties of stainless steel.

In the simulation, we impose the heat flux on the surface of the minidiode and the cylindrical resistor as the thermal condition. The heat flux on the cylindrical resistors is divided by the contribution from the PFLs and from the beams and is given as follows:

$$\begin{cases} \dfrac{46.4}{\pi d_R \times 10^{-3} \times l_R + 2\pi (d_R \times 10^{-3}/2)^2} \simeq 2128 \text{ W/m}^2, & \text{the contribution from the PFLs,} \\ \dfrac{35.8/25}{\pi d_R \times 10^{-3} \times l_R + 2\pi (d_R \times 10^{-3}/2)^2} \simeq 67 \text{ W/m}^2, & \text{the contribution from 1-MW beam, for example.} \end{cases} \tag{19}$$

The heat flux on the minidiode is given as follows:

$$\begin{cases} \dfrac{0.1}{\pi D_d \times 10^{-3} \times l_d \times 10^{-3} + 2\pi (D_d \times 10^{-3}/2)^2} \simeq 572 \text{ W/m}^2, & \text{the contribution from the PFLs,} \\ \dfrac{25.3/(30 \times 27)}{\pi D_d \times 10^{-3} \times l_d \times 10^{-3} + 2\pi (D_d \times 10^{-3}/2)^2} \simeq 179 \text{ W/m}^2, & \text{the contribution from 1 MW beam, for example,} \end{cases} \tag{20}$$

where Eqs. (10) and (12) are used for the estimations "from the contribution from the PFLs" on the resistor and diode. The measured 1-MW beam-induced power consumption on the diode unit, which will be discussed in Sec. VII and summarized in Table V, is used to evaluate "the contribution from 1-MW beam" on the resistor and diode.

The surfaces on the diode, the resistors, and their metal fixtures, are in contact with the flowing oil. To account for the heat transfer from the diodes and resistors to these materials (metal and oil), we adopt "coupled" boundary conditions of the diodes and resistors in ANSYS FLUENT©.

The radiation effect can be taken into consideration in ANSYS FLUENT© simulations. However, determining the "internal emissivity" from non-blackbody heated material (such as the diodes and resistors) is difficult. Therefore, we perform both simulations with the internal emissivity set to 1 (blackbody case) and without consideration of the radiation effects, recognizing the mitigation effect of radiation on the heating of the diodes and resistors.

TABLE V. The relationship between particle per pulse and beam power consumption.

Particles per pulse (two bunches)	Output beam power (MW)	Power consumption on one diode unit (diodes +10-Ω resistor) due to beam with 25 Hz (W)
8×10^{13}	0.96	$61.1 = (25.3 + 35.8)$
7×10^{13}	0.84	$54.3 = (27.4 + 26.9)$
6×10^{13}	0.72	$42.0 = (23.2 + 18.8)$
5×10^{13}	0.60	$29.1 = (16.7 + 12.4)$
4×10^{13}	0.48	$18.0 = (10.6 + 7.4)$
3×10^{13}	0.36	$11.6 = (7.8 + 3.8)$
2×10^{13}	0.24	$5.0 = (3.6 + 1.4)$

Figure 29 shows the simulation results obtained without beam contributions to the heating (the left and the right panels show the cases with and without the radiation effects, respectively), describing only PFL contributes to the heat fluxes on the resistors and the diodes. Temperature color scale is in Celsius. The nominal oil flow is set to 6.5 L/ min at the inlet. The oil temperature on the inlet is assumed to be 300 K(=27 °C). The simulation results reveal that the oil temperature from the outlet is 306.3 K(=33.3 °C) with the radiation effect and is 306.5 K(=33.5 °C) without this effect. This indicates that the temperature rise ΔT for the oil is ~6.5 °C.

Each number in the figure corresponds to the temperatures around the area indicated by the arrows. For example, 36.8–41.2 °C on the first line in the left panel means that the temperatures of the diodes range from 36.8 °C to 41.2 °C, depending on the position of the minidiodes on this plane.

The highest conceivable temperature rise occurs in the case without radiation effects, represented in the right panel of Fig. 29. That is, the real temperature distribution should lie between the distributions shown in the left and the right panels of Fig. 29. The radiation effect could mitigate the temperature rise of the diodes and resistors by 2 and 5 °C,

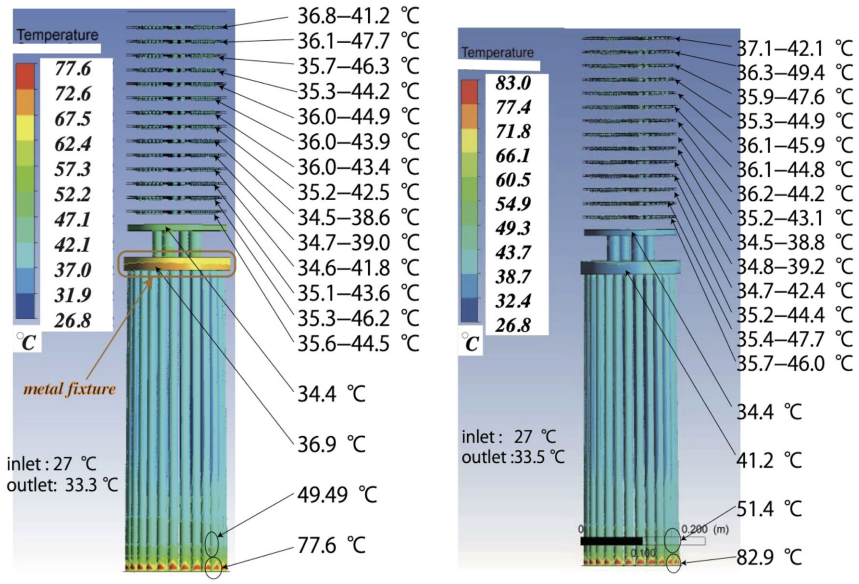

FIG. 29. Temperature distribution on the diode unit with radiation effects and without beam heating effects (left) and on the diode unit without both radiation and beam heating effects (right). Temperature color scale is in Celsius. The nominal oil flow is 6.5 L/ min at the inlet.

respectively. The effect is more enhanced for the resistors, owing to the larger surface area of the resistors compared with that of the diodes.

As the results without radiation effects (right in Fig. 29) show the temperature of the diodes ranges from 34.5 to 49.4 ℃, while the temperature of oil surrounding the diodes can be roughly estimated as ∼30 ℃. Hence, the difference between the average temperature of the diodes and the temperature of the oil is estimated as $(49.4 + 34.5)/2 - 30 \simeq 12$ ℃. This value is somewhat higher than the value (7.75 ℃) analytically estimated from Eq. (18) but is still a good rough estimate. Therefore, the analytical method can serve as a good guideline for estimating the temperature rise of diodes especially at the very early design stage of the diode unit.

The temperature of the resistor ranges from 41.2 to 82.9 ℃ in the right in Fig. 29. The oil flows from the center of the oil tank bottom (the inner side of the resistors) to the outer side of the resistors, as shown in the left and center panels of Fig. 28. Therefore, the highest temperature and lowest parts are at the bottom and top of the resistors, respectively. In other words, the outer bottom parts of the resistors are the least effectively cooled position in the diode unit, owing to the characteristic of the oil flow.

Similar to the diode case, we determine the reliability of the analytical method in estimating the temperature rise of the resistors. The difference between the average temperature on the resistor and the surrounding temperature (∼30 ℃) is calculated as $(82.9 + 41.2)/2 - 30 \simeq 32$ ℃. The result is more consistent with the analytical estimate of 31 ℃ obtained from Eq. (5), thanks to the simpler structure of the resistor part compared with that of the diode part.

As the color contour on the metal fixture between the resistor and diode parts in the left panel of Fig. 29 with radiation effects indicates heat conduction occurs from the resistors to the upper metal plate on the resistors (the conduction effect can be identified even from the right panel by carefully examining the corresponding color contour). The results indicate that the heat conduction effect occurring in the metals besides the resistors and the diodes is essential for determining the temperature distribution of the diode unit and accurately estimating the temperature rise on the resistors and diodes. Hence, the diode and the resistor parts must be separated by a distance of 36 mm, as shown in the left panel of Figs. 5 and 12.

We also analyze the simulation results including the 1-MW beam contributions. Figure 30 shows the results (the left and the right panels show the cases with and without the radiation effects, respectively). These results suggest that the highest temperature on the diode could be 54.4 ℃ on the second layer from the cathode side in the worst case; the corresponding temperature on the resistor could reach 84.7 ℃ at the very bottom end of the resistors. Still, the temperatures at the terminals of the diodes and the resistors are sufficiently lower than the respective critical temperatures (i.e., 85 and 150 ℃) when the oil flow and the temperature at the inlet are 6.5 L/ min and 27 ℃, respectively.

The result shown in the right panel of Fig. 29 is compared with that in Fig. 30. This comparison reveals that the 1-MW beam could contribute to the temperature

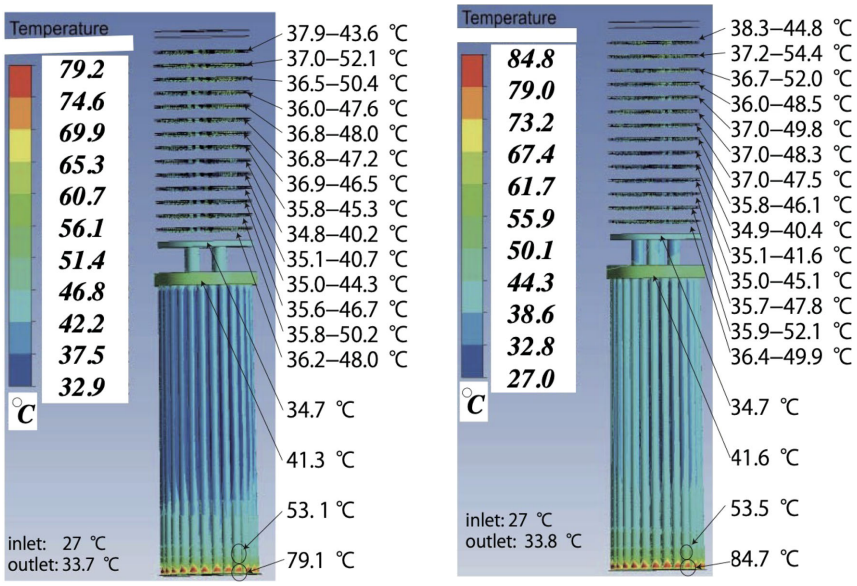

FIG. 30. Temperature distribution on the diode unit with both radiation and 1-MW beam heating effects (left), and on the diode unit including 1-MW beam heating effects without the radiation effect (right). Temperature color scale is in Celsius. The nominal oil flow is 6.5 L/ min at the inlet.

rise of the diode and the resistor by 5 and 1.8 °C, respectively.

Based on the simulation result for the 1-MW beam, we expect that this scheme for suppressing the kicker impedance can be applied to at least 5-MW beam power with an oil flow of 6.5 L/ min because we can estimate the temperature rise of the resistor caused by the 5-MW beam is $1.8 \times 25 = 45$ °C. Under the assumption, the temperature of the resistor can reach $82.9 + 45 \approx 130$ °C, which is still below 150 °C.

Furthermore, we can probably neglect the diode part, because Table V in Sec. VII suggests that the power consumption of this part peaks at ~840 kW beam. This peak consumption results from the fact that the dynamic resistance of the diode should decrease with increasing beam intensity. If this assumption is valid, the highest temperature of the minidiode could be ~54.4 °C (see the right of Fig. 30), even at 5-MW beams, when the radiation effect is neglected.

Figure 31 shows the simulation results of the 5-MW case without radiation effects. As the input parameters, the heat flux due to the 5-MW beam on a cylindrical resistor is assumed to be

$$\frac{1000/25}{\pi d_R \times 10^{-3} \times l_R + 2\pi (d_R \times 10^{-3}/2)^2} = 1871 \ [\mathrm{W/m^2}], \tag{21}$$

rather than 67 $\mathrm{W/m^2}$ for 1 MW beams described in Eq. (19). The result shows the high nonlinearity of the power increase. The heat flux on a minidiode is assumed to be 179 $\mathrm{W/m^2}$ as in the case of 1-MW beams following the previous speculation.

For the resistors, the temperature on the bottom of a resistor is 132 °C in the simulations and hence excellent agreement is obtained between the previous rough estimate (130 °C) and the simulations. However, the analytical estimation for the diodes is poor, because the highest

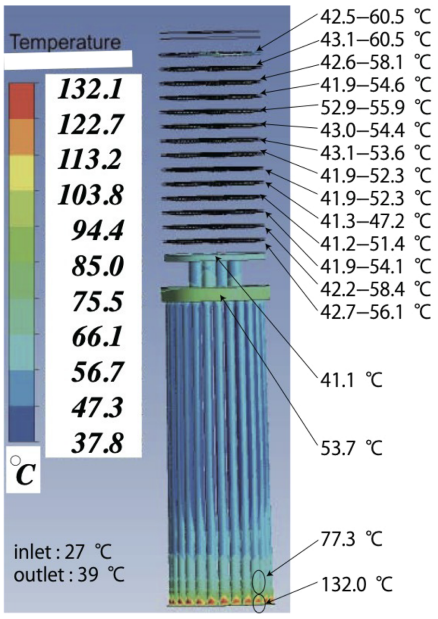

FIG. 31. Temperature distribution on the diode unit without radiation mitigation effects, where a 5-MW beam is extracted with a 25-Hz repetition rate. Temperature color scale is in Celsius. The nominal oil flow is 6.5 L/ min at the inlet.

temperature is 60.5 °C. This results from the fact that the oil heated by the resistors on the upstream side warms the diodes on the downstream side. Nevertheless, the simulations suggest that the modified diode unit can be applicable for up to 5-MW beams with the nominal oil flow being 6.5 L/ min at the inlet because the temperature on the diode is still below 85 °C even when we neglect the mitigation effect induced by radiation effects.

We also investigate the oil flow dependence of the diode unit temperature. The filter unit (see Fig. 26) is inserted into the downstream side of the unit, which limits the highest oil flow to 6.5 L/ min up to now, for safety reasons. In the present RCS system, the cooling oil is shared with a whole power supply for one kicker, including thyratrons, end-clippers, etc. Thus, if the diode part is destroyed accidentally due to some malfunctioning of the cooling system, the scrapped minidiodes can flow into the entire power supply, since the size of the minidiode is $D_d(=5.4\ \mathrm{mm}) \times l_d(=7.6\ \mathrm{mm})$.

However, we can remove the filter unit and increase the flow to 18.5 L/ min at the RCS after the reliability of the unit and the cooling system is established. In principle, we can perfectly eliminate the risk by additionally installing a special cooling system for the diode unit. This treatment can lead to a significant reduction in the temperature rise of the diodes and the resistors.

The combination of Eqs. (5)–(9) and (15)–(18) suggests that the effect of the oil flow is roughly proportional to the square root of the oil-flow velocity, with suppression of the resistor and diode temperature rise.

When $\mathbb{V}=18.5\,\mathrm{L/min}$, $T_o = 30\,^{\circ}\mathrm{C}$, $\nu = 17 \times 10^{-6}\ \mathrm{m^2/s}$, $\mathrm{Pr} = 170$, $\lambda = 0.15\,\mathrm{W/mK}$, $w_R = 46.4 + 35.8/25 \simeq 47.8\,\mathrm{W}$ [see Eq. (19)], and $iv = 0.1 + 25.3/(30 \times 27) \simeq 0.13\ \mathrm{W}$ [see Eq. (20)], the temperature rise of the resistor is analytically calculated as

$$T_R - T_o = \frac{w_R}{h_R l_R \pi d_R \times 10^{-3}} \simeq 19.3\ [\mathrm{K}], \tag{22}$$

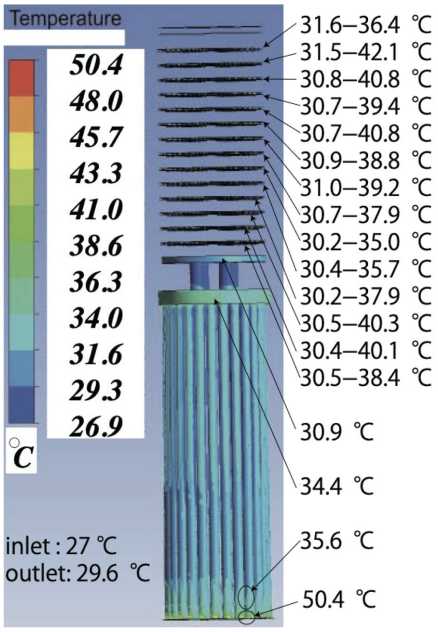

FIG. 32. Temperature distribution on the diode unit with radiation mitigation effects, where a 1-MW beam is extracted with a 25-Hz repetition rate. Temperature color scale is in Celsius. The nominal oil flow is 18.5 L/ min at the inlet.

[refer to Eq. (11)] resulting in $T_R = 49.3\,^{\circ}\mathrm{C}$ and the rise of the diode should be suppressed as

$$T_d - T_o = \frac{iv}{h_D l_d \times 10^{-3} \pi D_d \times 10^{-3}} \simeq 6.1\ [\mathrm{K}], \tag{23}$$

[refer to Eq. (18)] yielding (via the analytical method) $T_d = 36.1\,^{\circ}\mathrm{C}$ for the 1-MW beam in the case of $T_o = 30\,^{\circ}\mathrm{C}$, because the respective heat transfer coefficients h_R and h_D are calculated as

$$h_R = \frac{0.3\lambda}{d_R \times 10^{-3}} + \frac{0.62\lambda(\mathbb{V}d_R \times 10^{-1})^{\frac{1}{2}}\mathrm{Pr}^{\frac{1}{3}}\left(1 + \left(\frac{\mathbb{V}d_R \times 10^{-7}}{1692000 l_R \nu(\pi D_i - 25 \times d_R \times 10^{-3})}\right)^{\frac{5}{8}}\right)^{\frac{4}{5}}}{d_R(6 l_R \nu)^{\frac{1}{2}}(\pi D_i - 25 d_R \times 10^{-3})^{\frac{1}{2}}\left[1 + \left(\frac{0.4}{\mathrm{Pr}}\right)^{\frac{2}{3}}\right]^{\frac{1}{4}}}$$
$$\simeq 115.5[\mathrm{W/m^2\ K}], \tag{24}$$

and

$$h_D = \frac{0.3\lambda}{D_d \times 10^{-3}} + \frac{0.62\lambda(\mathbb{V}D_d)^{\frac{1}{2}}\mathrm{Pr}^{\frac{1}{3}}\left[1 + \left(\frac{\mathbb{V}D_d \times 10^{-3}}{4.23 \times 10^9 \pi D^2 \nu}\right)^{\frac{5}{8}}\right]^{\frac{4}{5}}}{D_d(15\pi\nu)^{\frac{1}{2}} D\left[1 + \left(\frac{0.4}{\mathrm{Pr}}\right)^{\frac{2}{3}}\right]^{\frac{1}{4}}} \simeq 165\ [\mathrm{W/m^2\,K}]. \tag{25}$$

Figure 32 presents the simulation result inclusive of the radiation effects with the nominal oil flow being 18.5 L/ min at the inlet, where a 1-MW beam is accelerated with a 25-Hz repetition rate. A temperature of 50.4 °C is determined for the bottom part of the resistor. The mean temperature of the resistors and the diodes are $(50.4 + 34.4)/2 \simeq 42.4\,^{\circ}\mathrm{C}$ and $(42.1 + 30.2)/2 \simeq 36\,^{\circ}\mathrm{C}$, respectively, suggesting analytical estimates given by Eqs. (22)

and (23) could be a good guideline for a judgment of whether the diode unit may malfunction or not. Overall, the analytical manner without radiation effects surprisingly provides relatively good estimates for the temperature rise of the resistors and diodes associated with oil flow levels of 18.5 L/ min as well as 6.5 L/ min.

C. Experimental validation of temperature increase

We also conducted measurements without beam contributions by using prototype power supply, equivalent to the installed kicker, and compared the measurements with the simulations shown in Fig. 29. A "temperature label" [30] is used to measure the temperature of objects to which the label is attached (refer to Fig. 33). Several numbers are shown on the temperature label. Changes in the color of the numbered part on the label indicate to us that the temperature reaches the numbered degree of Celsius. The present temperature label can measure temperatures ranging from 50 to 120 ℃. It is planned that more direct measurements will be conducted by monitoring the inside of the diode unit by making holes on the surface of it when we fabricate and install the second diode unit into another kicker.

The prototype kicker power supply was operated for 24 hours to directly measure the surface temperatures of the resistors by attaching the temperature label to the cylindrical resistor (see the upper-left and middle-left panels of Fig. 33). The temperature labels are attached to the lower part of the resistor part, i.e., the site experiencing the highest temperature (see Fig. 29). Direct attachment of the labels to the minidiodes is desired, but is quite difficult, owing to the small size of these diodes. Hence, we measure the temperature on the metal plate below the diode part instead, as shown in the upper-right and middle-right panels of Fig. 33.

The upper-left and upper-right panels in Fig. 33 show the temperature labels on the resistors and the metal plate below the diode part prior to 24-h operation of the kicker; the middle-left and middle-right panels show the resistors and plate after the operation. The lower-left and lower-right figures show the temperature labels detached from the resistors and the plate, respectively, after the operation. Any numbered parts remained unchanged, demonstrating that the temperature of each measured part was <50 ℃.

As shown in Fig. 29, the simulation results with the radiation effects are more consistent with the measurements than the results without these effects, because the simulations with the radiation effect represent that the temperature of the temperature label attachment site reaches 49.49 ℃, which is still lower than 50 ℃. Moreover, consistent with the measurements, the temperature of the metal plate reaches only 34.4 ℃ in the simulations. Consequently, the measurements directly demonstrate that the risk of the heating-induced resistor and diode destruction is drastically reduced by modifying the prototype diode unit with the new diode unit.

FIG. 33. The upper-left and upper-right panels show the cases where temperature labels are attached to the resistors and the metal plate below the diode part prior to 24-h operation of the kicker. The middle-left and middle-right panels show the resistors and metal plate after the operation. The lower-left and lower-right panels show the temperature labels detached from the resistors and the plate after the operation.

VI. TEMPERATURE MEASUREMENTS PERFORMED ON CIRCULATING OIL

We measured the temperature of circulating oil to indirectly detect the malfunction of the diode unit after 12 continuous days (17280 min) of kicker operation. Thermocouples are used to measure the room temperature and the temperatures at the upstream and downstream side of end-clipper 2, and those of the diode unit.

The left panel of Fig. 34 shows the overall behavior of the measured temperature. The right panel shows a magnified view around the rising edge of the temperature. The red solid line with (○) and red dotted line (unmarked) denote the temperature at the inlet of the diode unit, and the temperature at the outlet of the unit, respectively. The blue solid line with (□), blue dotted line (unmarked), and black line represent the temperature at the inlet of the end-clipper, the temperature at the outlet of the end-clipper, and the atmospheric temperature, respectively.

The left panel of Fig. 35 shows $\Delta T(t)$ [the temperature difference between the inlet and the outlet of the diode unit

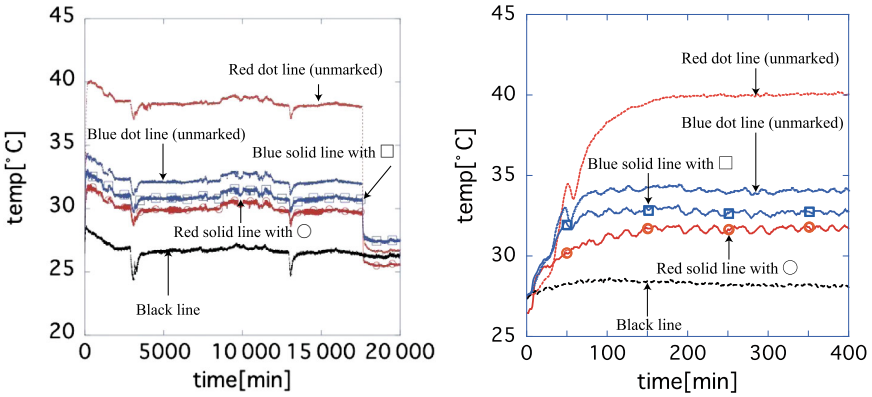

FIG. 34. The left panel shows the temperature of the diode unit (red), end-clipper (blue), and the air (black) measured in 12 days (17280 min) of kicker operation. The right panel shows a magnified view around the rising edge of the temperature. The red solid line with (○) represents the temperature at the inlet of the diode unit and the red dotted line (unmarked) represents the temperature at the outlet of the unit. Furthermore, the blue solid line with (□) denotes the temperature at the inlet of the end-clipper, the blue dot line (unmarked) denotes the temperature at the outlet of the clipper, and the black line denotes the atmospheric temperature.

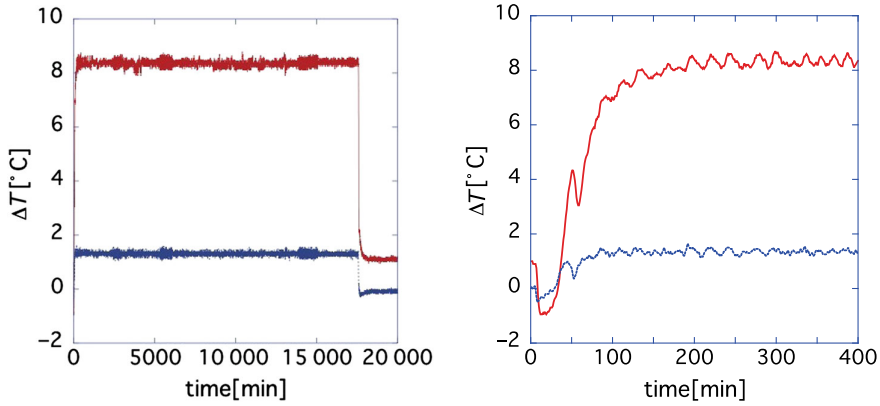

FIG. 35. The left panel shows the $\Delta T(t)$ (temperature difference between the inlet and the outlet of the diode unit and the end-clipper) measured in 12 days. The red and blue lines show the diode unit and the end-clipper, respectively. The right panel shows a magnified view of the left panel around the rising edge of $\Delta T(t)$.

(red) and the end-clipper (blue)]. The right panel shows a magnified view of the lines around the rising edge of $\Delta T(t)$.

The temperature $T(t,x)$ of the diode unit, when the surface of the unit is assumed to be adiabatic, can be analytically calculated from the energy balance, i.e.,

$$\frac{C[\mathrm{kJ/K}]}{L[\mathrm{m}]}\frac{\partial T}{\partial t}\left[\frac{K}{s}\right] = \frac{W[\mathrm{kW}]}{L[\mathrm{m}]} - \dot{m}\left[\frac{\mathrm{kg}}{s}\right] c_p\left[\frac{\mathrm{kJ}}{\mathrm{kg}\cdot\mathrm{K}}\right]\frac{\partial T}{\partial x}\left[\frac{\mathrm{K}}{\mathrm{m}}\right] \tag{26}$$

$$= \frac{W[\mathrm{kW}]}{L[\mathrm{m}]} - r\left[\frac{\mathrm{g}}{\mathrm{cm}^3}\right]\frac{1\left[\frac{\mathrm{kJ\cdot cm}^3}{\mathrm{J\cdot L}}\right]}{60\left[\frac{s}{\mathrm{min}}\right]}\mathbb{V}\left[\frac{\mathrm{L}}{\mathrm{min}}\right] 4.184\left[\frac{\mathrm{J}}{\mathrm{cal}}\right] \times \bar{c}_p\left[\frac{\mathrm{cal}}{\mathrm{g}\cdot\mathrm{K}}\right]\frac{\partial T}{\partial x}\left[\frac{\mathrm{K}}{\mathrm{m}}\right], \tag{27}$$

where the coordinates (t,x) are used to specify the time and the position along the diode unit; L [m] is the total length of the diode unit; C[kJ/K] is the heat capacity of the diode unit; W [kW] is the total heating rate resulting from the resistors and diodes; $\dot{m}[\mathrm{kg/s}](=r[\mathrm{g/cm}^3]\cdot\mathbb{V}[\mathrm{L/\,min}]/60)$, $c_p[\mathrm{kJ/kg\,K}]$ $(=4.184\bar{c}_p[\mathrm{cal/g\ K}])$, $r[\mathrm{g/cm}^3]$, and $\mathbb{V}[\mathrm{L/\,min}]$ are the mass flow rate, isobaric specific heat, specific gravity, and flow rate of the oil, respectively.

The general solution of Eq. (26) is expressed as

$$T(t,x) = x\frac{W}{\dot{m}c_pL} + \phi\left(t\frac{\dot{m}c_pL}{C} - x\right), \tag{28}$$

by introducing an arbitrary function $\phi(x)$. Then, we assume that the function is given as

$$\phi\left(t\frac{\dot{m}c_pL}{C}-x\right)=A_0+B_0e^{\alpha(t\frac{\dot{m}c_pL}{C}-x)}, \tag{29}$$

where A_0, and B_0 are constants and α is a constant determined from the cooling efficiency associated with the whole oil circulating system.

When $T(t=0,x=0)=T_{mi,0}$ and $T(t=0,x=L)=T_{mo,0}$, the temperature at the inlet $T_{mi}(t)=T(t,x=0)$ and the temperature at the outlet $T_{mo}(t)=T(t,x=L)$ are, respectively, given as

$$T_{mi}(t)=-\frac{(T_{mo,0}-T_{mi,0}e^{\alpha L}-\frac{W}{\dot{m}c_p})}{(e^{\alpha L}-1)}+\frac{(T_{mo,0}-T_{mi,0}-\frac{W}{\dot{m}c_p})}{(e^{\alpha L}-1)}e^{-\alpha\frac{\dot{m}c_pL}{C}t}, \tag{30}$$

$$T_{mo}(t)=T_{mo,0}-\frac{(T_{mo,0}-T_{mi,0}-\frac{W}{\dot{m}c_p})e^{\alpha L}}{(e^{\alpha L}-1)}+\frac{(T_{mo,0}-T_{mi,0}-\frac{W}{\dot{m}c_p})}{(e^{\alpha L}-1)}e^{-\alpha(t\frac{\dot{m}c_pL}{C}-L)}, \tag{31}$$

after Eq. (29) is rewritten.

By setting the temperature difference $\Delta T(t)$ between the inlet and the outlet to

$$\Delta T(t)=T_{mo}(t)-T_{mi}(t), \tag{32}$$

we obtain

$$\Delta T(t)=\frac{W}{\dot{m}c_p}+\frac{T_{mo,0}\left[e^{-\alpha(t\frac{\dot{m}c_pL}{C}-L)}-e^{-\alpha(t\frac{\dot{m}c_pL}{C})}\right]}{(e^{\alpha L}-1)}-\frac{T_{mi,0}\left[e^{-\alpha(t\frac{\dot{m}c_pL}{C}-L)}-e^{-\alpha(t\frac{\dot{m}c_pL}{C})}\right]}{(e^{\alpha L}-1)}-\frac{W\left[e^{-\alpha(t\frac{\dot{m}c_pL}{C}-L)}-e^{-\alpha(t\frac{\dot{m}c_pL}{C})}\right]}{\dot{m}c_p(e^{\alpha L}-1)}. \tag{33}$$

For sufficiently large times, the temperature $T_{mi}(t)$ at the inlet and the temperature difference $\Delta T(t)$ converge to $\hat{T}_{mi}^{(c)}$ and $\Delta T^{(c)}$, which are given as follows:

$$\hat{T}_{mi}^{(c)}=-\frac{T_{mo,0}}{(e^{\alpha L}-1)}+\frac{T_{mi,0}e^{\alpha L}}{(e^{\alpha L}-1)}+\frac{\Delta T^{(c)}}{(e^{\alpha L}-1)}, \tag{34}$$

$$\Delta T^{(c)}=(\hat{T}_{mo}^{(c)}-\hat{T}_{mi}^{(c)})=\frac{W[\mathrm{kW}]}{\dot{m}c_p[\mathrm{kW/K}]}=\frac{1000W[\mathrm{kW}]}{r[\frac{g}{\mathrm{cm}^3}]\frac{1}{60}\mathbb{V}[\frac{L}{\mathrm{min}}]4.184\bar{c}_p[\frac{\mathrm{cal}}{gK}]}, \tag{35}$$

with the cooling efficiency α:

$$e^{\alpha L}=\frac{(T_{mo,0}-\hat{T}_{mo}^{(c)})}{(T_{mi,0}-\hat{T}_{mi}^{(c)})}, \tag{36}$$

and the converged temperature $\hat{T}_{mo}^{(c)}$ at the outlet:

$$\hat{T}_{mo}^{(c)}=-\frac{T_{mo,0}}{(e^{\alpha L}-1)}+\frac{T_{mi,0}e^{\alpha L}}{(e^{\alpha L}-1)}+\frac{\Delta T^{(c)}e^{\alpha L}}{(e^{\alpha L}-1)}. \tag{37}$$

When α is positive infinite, $T_{mi}(t)=T_{mi,0}$, and $T_{mo}(t)=T_{mi,0}+W/\dot{m}c_p$, which are independent of t and are always constant.

Referring to Fig. 34, we can estimate $T_{mo,0}=273+27.45=300.45$ K, and $T_{mi,0}=273+26.45=299.45$ K for the diode unit. We also determine the converged average temperature $\hat{T}_{mo}^{(c)}=273+39.9=312.9$ K, and $\hat{T}_{mi}^{(c)}=273+31.5=304.5$ K at $t=200$ min. The length of the oil tank is $L=1.127$ m, and hence we can evaluate the cooling efficiency as $\alpha=0.8$ [/m] from Eq. (36).

As shown in Eq. (35), the convergence value of $\Delta T^{(c)}$ is related to the heating value W (which is equal to $W=1.25$ kW without beam contributions), the oil flow velocity $\mathbb{V}$ (which is 6.5 L/ min in the present case), the oil specific gravity r and specific heat of the oil c_p. We can analytically estimate the convergence value of $\Delta T^{(c)}$, provided with the oil-specific gravity r and specific heat of the oil c_p in Table IV [26], where the properties of the used oil, Shin-Etsu Chemical's silicon oil (KF-96-20CS), are listed. When the oil temperature $T\sim 308.7$ K, we can estimate a density of $\rho=941$ kg/m^3 (specific gravity $r=0.941$) and $c_p=1.6$ kJ/kg K ($\bar{c}_p=382.4$ cal/g K), corresponding to the Prandtl number (Pr ~ 170), thermal conductivity ($\lambda=0.15$ W/m K), and kinematic viscosity of oil ($\nu=17\times 10^{-6}$ m^2/s).

After substituting these values into Eq. (35), we obtain $\Delta T^{(c)}\simeq 7.66$ K. The exponential factor of Eq. (30) yields the heat capacity $C=221.8$ kJ/K of the oil tank from the estimated values of $\dot{m}, c_p$, α, and L.

Figure 36 shows the overall behavior of the analytical calculations of $\Delta T(t)$ involving Eq. (33), where $W=1.25$ kW, $r=0.941$, $\mathbb{V}=6.5$ L/ min, $\bar{c}_p=1.6$ kJ/kg K, $\alpha=0.8$ [/m], $C=221.8$ kJ/K, and $L=1.127$ m. Although the converged $\Delta T^{(c)}$ is slightly lower than the measured values observed in the right panel of Fig. 35, the trends are quite consistent with the measurement results, indicating that we can find whether the diode unit is in the normal state or not by monitoring the oil temperature and the oil velocity.

Now, let us consider the beam contribution to oil heating. The measured power consumption contributed by the accelerated beams on the diode unit is summarized in Table V. When a 1-MW beam is accelerated with a repetition rate of 25 Hz, the power consumption on the

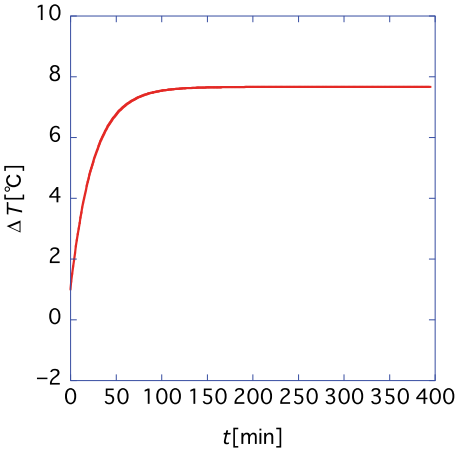

FIG. 36. Analytical result of $\Delta T(t)$ for the diode unit, where $W = 1.25$ kW, $r = 0.941$, $\mathbb{V} = 6.5$ L/ min, $\bar{c}_p = 1.6$ kJ/kgK, $\alpha = 0.8$ [/m], $C = 221.8$ kJ/K, $L = 1.127$ m.

diodes and the 10-Ω resistor in the diode unit is 25.3 [W] and 35.8 [W], respectively. These contribute to the temperature rise of the unit, evaluated as $\Delta T^{(c)} = 0.4$ [K], which is negligible compared with a rise of $\Delta T^{(c)} \simeq 8$ [K] due to only the PFLs. A comparison of the simulation results shown in the left panels of Figs. 29 and 30 reveals that the contribution from the beam is $\Delta T^{(c)} = 0.4$ [K], which is quite consistent with the analytical estimate.

Therefore, we can indirectly determine the stability of the diode unit by monitoring the temperature rise of the unit. Figure 37 shows the $\Delta T(t)$ measured in 45 days under RCS operations (830 kW beam effects are included). The result is consistent with that of the measurement without beam contribution (see Figs. 35 and 36), demonstrating the reliability of the diode unit and the contribution from the beam is negligible compared to that from the PFLs.

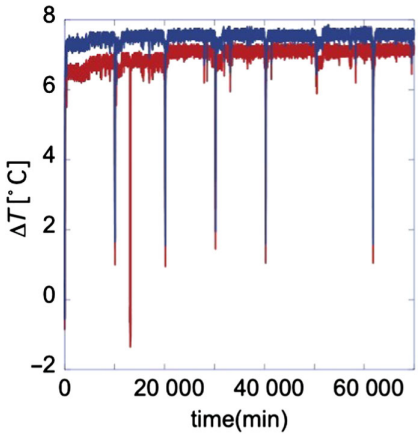

FIG. 37. Measurements of $\Delta T(t)$ during 45 days ($=45 \times 24 \times 60 = 64\,800$ min) including 830-kW beam effects. The red and blue lines represent the results of diode unit 1 and diode unit 2, respectively.

The monitoring system concerning the oil temperature is going to be attached to the diode unit for routine operation at the RCS so that we can double-check the malfunctioning of the unit by measuring the oil temperature as well as the oil flow at the inlet of the diode unit.

Finally, let us estimate the temperature rise of the end-clipper by this method for a consistency check of the present kicker model, as well as for the enhancement of the reliability of this method to estimate the temperature rise, because the structure of the end-clipper is similar to that of the diode unit, except for some parameter conditions. The blue solid and the blue dashed lines in the right panel of Fig. 34 represent the measured temperature at the inlet and at the outlet, respectively, of the end-clipper. For the temperature $T \sim 300.0$ K, the parameters are estimated as $\rho = 948.34$ kg/m^3 ($r = 0.94834$), and $c_p = 1.6$ kJ/kg K ($\bar{c}_p = 382.4$ cal/g K). Hence, Eq. (35) yields $\Delta T^{(c)} \simeq 1.7$ K when the power consumption rate $W = 0.8$ kW (see Sec. IV) and the oil flow $\mathbb{V} = 18.5$ L/ min in the end-clipper. The estimate concurs with the measurement results for the end-clipper (see the blue in Fig. 35), although the oil flow $\mathbb{V}$ and the power consumption rate W differ from those of the diode unit.

VII. COUPLING IMPEDANCE: MEASUREMENTS AND SIMULATIONS

When accelerated beams pass through the kicker, the coupling between the beams and the coils in the kicker induces currents with exciting voltages between the high voltage and grounding plates in the kicker [11] (refer to Appendix A), which is the source of the kicker impedance causing beam instabilities. The beam-induced currents and voltages propagate toward the diode unit through 130-m long coaxial cables, partially absorbed into the unit, and reflected to the magnet part. They are superposed during the beam acceleration period (20 ms). Let us observe the beam-induced currents and voltages via the current transformer and the voltage probe in the relay box on the diode unit when two bunched beams are accelerated to detect the beam-coupling impedance.

The measurement conditions are as follows: The longitudinal painting is performed by turning on the second harmonic of rf cavity until 5 ms to mitigate the space effects [31,32]. In the transverse direction, the unnormalized painting transverse emittance, which is defined as unnormalized value of the entire painting area, is 200π mm mrad, created following the anticorrelated painting scheme [33]. In the RCS, the painting transverse emittance is adjustable from 0 to 200π mm mrad both in the horizontal and vertical directions [34]. Table V summarizes the measured particle number per pulse (particle number per two bunches), output beam power, and power consumption due to the beam on one diode unit (the diode and 10-Ω resistor) with a repetition rate of 25 Hz.

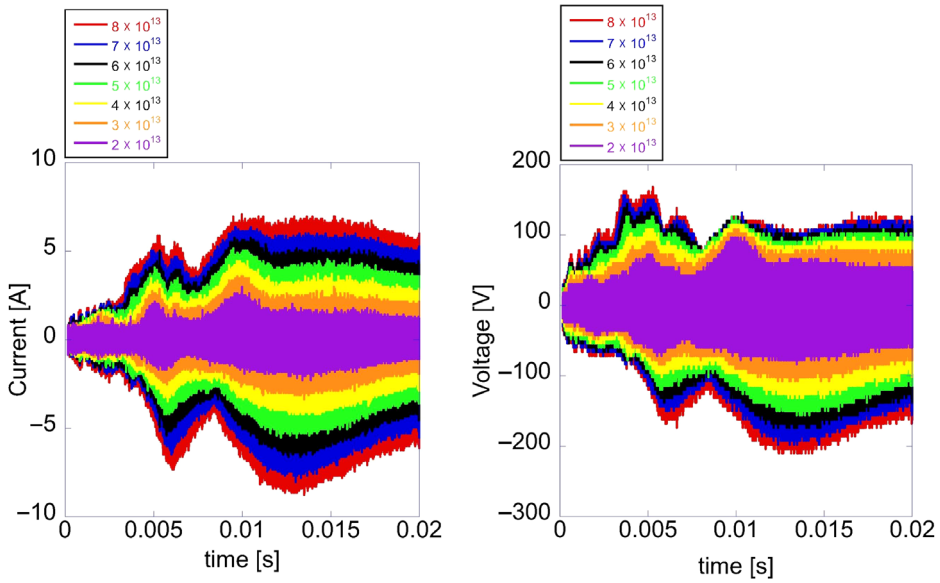

FIG. 38. Measured beam-induced current (left) and beam-induced voltage (right) on the diode unit (diode plus 10-Ω resistor).

Figure 38 shows the beam-induced current (left) on the diode unit (diode plus 10 Ω resistor) and beam-induced voltage (right). The red, blue, black, green, yellow, brown, and purple lines represent the results for 8×10^{13}, 7×10^{13}, 6×10^{13}, 5×10^{13}, 4×10^{13}, 3×10^{13}, and 2×10^{13} particle per pulse, respectively. The currents and the voltages are excited both positively and negatively, following envelope forms with a dip around 8 ms. Figure 39 shows one example of the normalized beam spectrum for 4×10^{13} particle per bunch (corresponding to 8×10^{13} particle per pulse) when the diode unit is attached, which is converted into Fourier space after the beam shape around 15 ms is measured by a wall current monitor along the RCS.

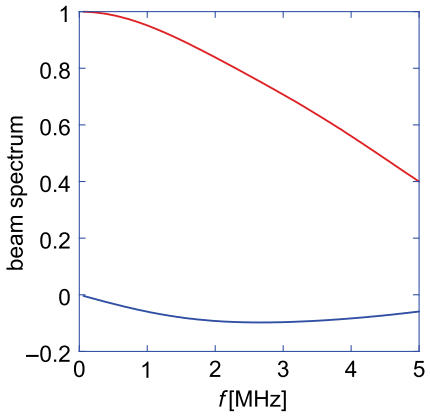

FIG. 39. One example of the normalized beam spectrum for 4×10^{13} particle per bunch (corresponding to 8×10^{13} particle per pulse) when the diode unit is attached (measurement), where the red and blue lines show the real and imaginary parts of the spectrum.

The minidiodes act as a capacitor as well as a rectifier for beam-induced currents. When a reverse voltage is applied, the anode and cathode are insulated, becoming a capacitor across the depletion layer. Then, the reverse current increases as the frequency increases. In addition, the structure of the diode part composed of the minidiodes creates inductance in the diode unit.

At the RCS, $B\rho$ curve follows the sinusoidal function with the period 40 ms, where Lorentz-β during the ramping process is shown in Fig. 40. We can see Lorentz-β drastically changes in the former period during the ramping time, especially from 5 to 10 ms. This means that the superposing pattern of the beam-induced currents and voltages are significantly changed during this ramping process because of the rapid change of the revolution frequency in the RCS. Moreover, the diodes cannot instantly respond to this change, and hence, the transient

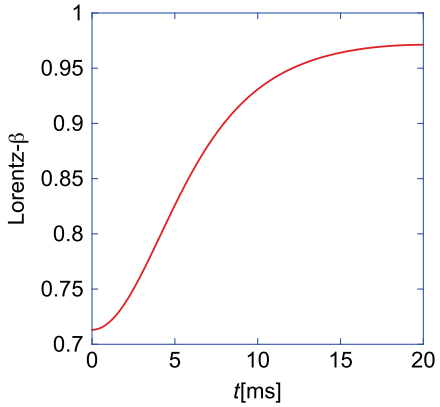

FIG. 40. Lorentz-β during the ramping process (calculation).

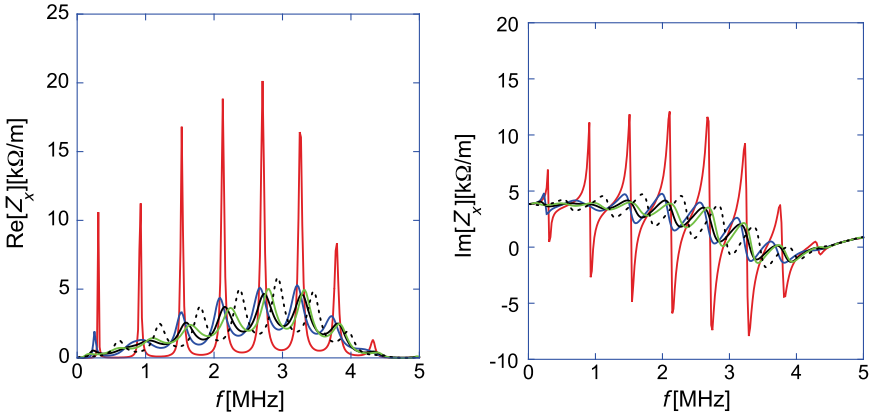

FIG. 41. Measurement results of Z_x for $\beta = 0.964$, where the diode unit is connected to the end of the thyratron through a 3.1-m long 20-Ω coaxial cable: The blue, black, and green lines show the results for 240, 480, and 960 kW beams, respectively. For comparison, the red line shows the theoretical result for the present kicker where the cable terminals are open "without any additional 3.1-m long 20 Ω coaxial cable." The black dotted line shows the theoretical result, where the thyratron end is terminated by only a 10-Ω resistor after a 3.1-m long 20-Ω coaxial cable.

effects intrinsic to the diode unit create the envelope shape with a dip of around 8 ms for the excited current and voltage patterns during the acceleration time.

Roughly, the beam-induced currents increased more than the beam-induced voltages when the beam intensity increased. This seems to suggest that the beam impedances of the kicker with the diode unit decreased with increasing beam intensity with a higher peak current. Nonetheless, the tendency is not so remarkable compared to the case of the prototype diode [14], because the increase of parallel branches in the diode part mitigates the contribution of it to the impedance of the diode unit in total.

The Fourier-transformed beam-induced voltage divided by the Fourier-transformed beam-induced current (the sign of the observed current must be opposite due to the setup of the current transformer in the relay box; refer to Sec. III) yields the effective impedance R_T of the diode unit. We can obtain the kicker impedance [14] by substituting the measured R_T into the formulas listed in Appendix B [14].

The transverse impedances Z_x for $\beta = 0.964$ are shown in Fig. 41, where the contribution from 3.1-m long 20-Ω coaxial cable is taken into consideration. It is better to be reminded that Z_x is roughly proportional to Lorentz-β at low frequency [14]. The left and right panels show the real and imaginary parts of the impedance, respectively. The blue, black, and green lines show the results for the 240, 480, and 960 kW beams, respectively. For comparison, the red line shows the theoretical result corresponding to the present kicker with open cable terminals "without both the diode unit and 3.1 m long 20 Ω coaxial cables" [14]. The black dotted line shows the theoretical result, where the thyratron end is terminated by only a 10-Ω resistor "after a 3.1 m long 20 Ω coaxial cable."

Figure 42 shows the theoretical results of Z_x for $\beta = 0.964$, where the thyratron end is "open" (red), or terminated by only a 10-Ω resistor (black), "after a 3.1 m long 20 Ω coaxial cable." There is no intensity dependence of Z_x, owing to the absence of diodes.

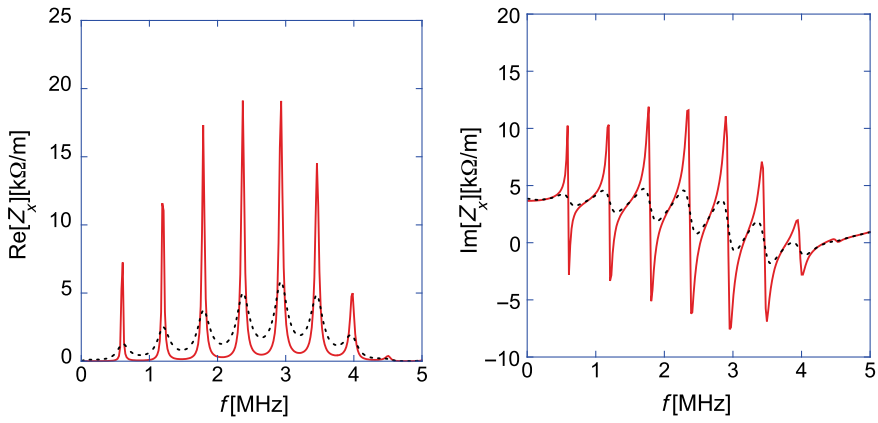

FIG. 42. Theoretical results of Z_x for $\beta = 0.964$, where the thyratron end is open (red) or terminated by only a 10-Ω resistor (black), "after a 3.1 m long 20 Ω coaxial cable."

The results in Figs. 41 and 42 are characterized by their spike structure created by the reflection waves excited at the end of 130-m long coaxial cables with impedance mismatch. Figure 41 directly shows, via measurements, that the diode unit makes the kicker impedance reduced to be comparable to the impedance where the thyratron end is terminated by only a 10-Ω resistor after a 3.1-m long 20-Ω coaxial cable. If we compare the impedances among various beam intensities fixed on the resonant frequencies of the impedance in the case of a 240-kW beam, we can see the tendency of the impedance reduction by increasing the beam intensity, consistent with the observation of beam-induced voltage and current in the time domain, though the difference is not so remarkable compared to the impedance of the prototype diode unit.

A closer look reveals that the beam intensity determines the spike structure (or resonant frequencies) of the impedance with the diode unit in Fig. 41 because the dynamic resistance of the diode depends on the beam intensity. As an extreme case, the resonant frequencies of the theoretical result (black dotted), where the thyratron end is terminated by only a 10-Ω resistor after a 3.1-m long 20-Ω coaxial cable, are significantly different from those (red) of the present kicker where the 130-m long coaxial cable terminals are open without any additional 3.1-m long 20-Ω coaxial cable. This is because the 3.1 m long 20 Ω coaxial cable lengthens the propagation length of beam-induced current and voltage from 130 m by 3.1 m. Finally, we can confirm the speculation by Fig. 42 because all resonant frequencies are identical between Z_x (red) where the thyratron end remains open after a 3.1-m long 20-Ω coaxial cable and that (black) where the end is terminated by a 10-Ω resistor through the cable.

The measurements more directly demonstrate that increasing the parallel branch in the diode stack is effective in minimizing the transverse impedance for the high-intensity beam and mitigating the intensity dependence of the impedance though the spike structure in the impedance is still critically determined by the beam intensity. Since the spike structure determines the tune on which the beam instabilities are excited during the ramping process, some optimization concerning the tune tracking might be preferable after all planned diode units have been installed for a routine operation [6,35].

The simulation approach partially supports the impedance reductions. The kicker is connected to 130-m long coaxial cables and hence performing a three-dimensional full simulation is almost impossible. Therefore, a partial three-dimensional simulation in combination with circuit simulation is performed by simulating the standard wire method, following the procedure outlined in Ref. [14]. This method is essentially the same as the simulation method described in Fig. 12.

The wire method, involving conversion of the scattering matrix into impedances, is simulated. The MW solver in CST STUDIO© provides the scattering matrix in combination with SPICE©. Twin wires are stretched inside the kicker chamber to obtain the transverse impedances. The impedance is calculated as follows [36]:

$$Z_x = -\frac{2cZ_{dd}}{\omega\Delta^2}\log\frac{S_{dd21}^{\mathrm{DUT}}}{S_{dd21}^{(\mathrm{ref})}}, \tag{38}$$

where Δ is the separation between the twin wires, Z_{dd} are the characteristic impedances for the differential modes; S_{dd21}^{DUT} and $S_{dd21}^{(\mathrm{ref})}$ are the transmission coefficients for the kicker (DUT) and the perfectly conducting reference chamber, respectively.

The lower panel of Fig. 43 shows an overview of the twin-wire measurement setup based on the electric circuit theory to calculate the transverse impedance where the cable terminals are open. The setup is divided into a magnetic part and cable parts, where the upper panel of Fig. 43 shows the magnified figure of the magnet part, which is the main platform in the three-dimensional simulation.

We consider two cases where the cable terminals are terminated by matched resistors after a 3.1-m long cable and where they are terminated by the diode units after a 3.1-m long cable. In these cases, we must replace the cable parts with the parts shown in the left panel or the right panel of Fig. 44, respectively. As shown in Fig. 43, ports (3)–(6) on the magnet are connected to the cables, while ports (1) and (2) describe the terminals composing the stretched wires and the kicker aperture. The terminals are terminated by the matched resistors (198.3 Ω) for the common mode. One end is terminated by the matched resistor (609.184 Ω) for the differential mode and the other is connected to the current source for the differential mode.

Here, the simulation is performed to obtain the S-matrix using time-domain analysis, because the diodes are the nonlinear device. In other words, the matrix is obtained by calculating the currents and the voltages on the wires in the time domain and then converting the calculated values into frequency spaces via Fourier transformation. The scattering matrix is calculated by substituting the current and voltage values into the following formula:

$$S_{dd21} = -\frac{2Z_{dd}\tilde{I}_2}{\tilde{V}_1 + Z_{dd}\tilde{I}_1}, \tag{39}$$

where $\tilde{I}_1$ and $\tilde{V}_1$ are the Fourier-transformed current and voltage at terminal 1, respectively; $\tilde{I}_2$ is the Fourier-transformed current at terminal 2; S_{dd21} represents the scattering matrix S_{dd21}^{DUT} or $S_{dd21}^{(\mathrm{ref})}$, depending on the simulation model.

Figure 45 shows the simulation results. The blue, black, and green lines show the results for the 240, 480, and 960 kW beams, respectively. For comparison, the red line shows the simulation result for the present kicker with an

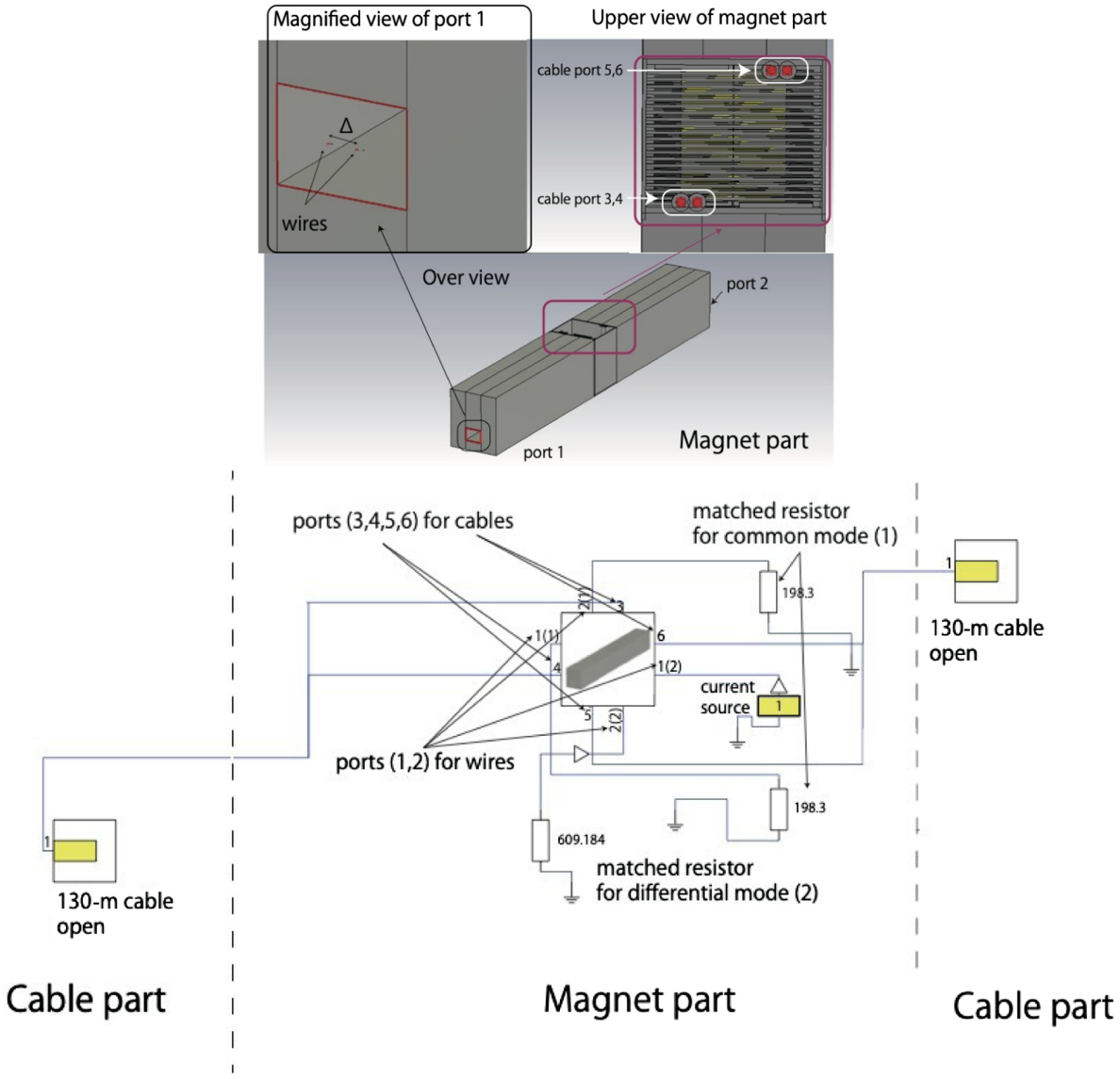

FIG. 43. The lower panel shows an overview of the twin-wire measurement setup based on the electric circuit theory, where the cable terminals are open. The upper panel shows the magnified figure of the magnet part, which is the main platform in the three-dimensional simulation.

open terminal without any additional 3.1-m long 20-Ω coaxial cable. The black dotted line shows the simulation result, where the thyratron end is terminated by only a 10-Ω resistor after a 3.1-m long 20-Ω coaxial cable.

The simulation results in Fig. 45 are considerably reduced compared to the present kicker impedance, describing the magnitude of the impedance is reduced to the level of the impedance when the thyratron end is hypothetically terminated by only a 10-Ω resistor after a 3.1-m long 20-Ω coaxial cable, though the measurement results in Fig. 41 demonstrate that they are more suppressed than the simulations. The intensity dependence of the impedance is mitigated in the simulations compared to the result of the prototype diode unit [14], as in the measured cases, by increasing the parallel branches of the diode part.

The simulations based on SPICE© tend to underestimate the suppression effect on the kicker impedance implementing the new diode stack. This is consistent with the results in Fig. 21, because the measured current with high-frequency components more passes through the diode units than the simulation result. In other words, it is difficult to accurately predict the impedance reduction over the high-frequency range with SPICE©, when we deal with a more complicated diode stack like a new diode, compared to the prototype diode with a simpler structure. In this sense, the measurements are preferable to precisely evaluate the kicker impedance rather than simulations.

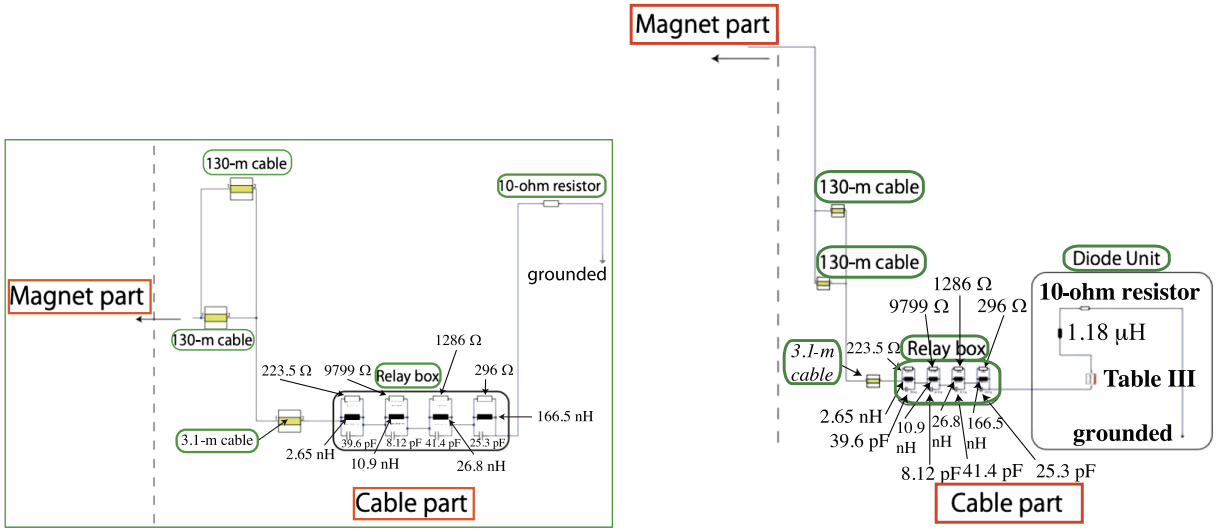

FIG. 44. The cable part. The left panel corresponds to the case where the cable terminals are terminated by matched resistors after a 3.1 m long cable. The right panel corresponds to the case where they are terminated by the diode units after a 3.1 m long cable.

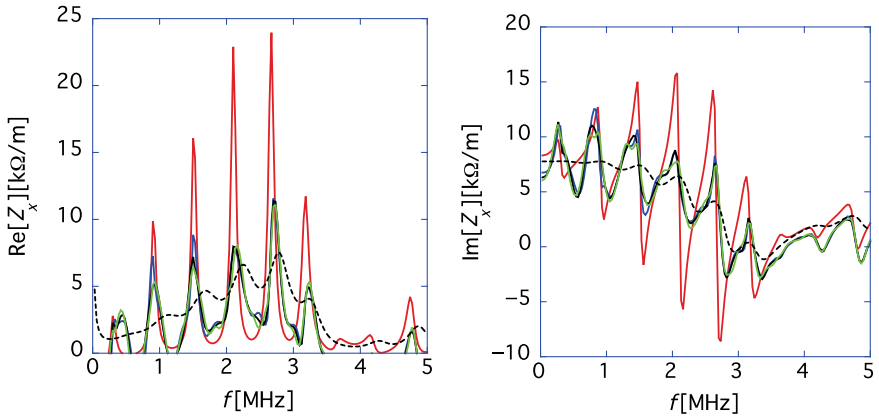

FIG. 45. Simulations: the beam intensity dependence of Z_x, where the diode unit is connected to the end of the thyratron through a 3.1-m long 20-Ω coaxial cable. The blue line, black line, and green line show the result for the 240, 480, and 960 kW beam, respectively. For comparison, the red line shows the simulation result for the present kicker. The black dotted line shows the simulation result, where the thyratron end is terminated by only a 10-Ω resistor after a 3.1-m long 20-Ω coaxial cable.

VIII. THE EFFECT OF THE IMPROVED DIODE UNITS ON BEAM

A. The suppression of beam instability

We also consider the effect of the impedance reduction on the beam instabilities at the RCS. Note that the diode unit is only attached to "one RCS kicker" among eight kickers installed at the RCS in this measurement while maintaining the present terminal condition for the other seven kickers.

In the RCS, the bipolar sextupole magnetic fields have been dynamically manipulating the chromaticity to suppress the beam instability [35,37,38]. Figure 46 illustrates the configuration of the bipolar power supply whose peak ratings are 1100 V and 750 A, respectively [39], where the original ac currents are converted into dc currents before the dc currents are inverted into ac currents for the sextupole magnet as its input current. Hence, the power supply is comprised of a diode rectifier, a smoothing circuit, pulse width modulation (PWM) inverter, and a passive filter. The PWM inverter is a voltage-fed H-bridge inverter, whose switching element uses an IGBT of 1400 V–600 A, and the switching frequency is 20 kHz. One sextupole magnet is modeled by a series circuit of the inductance L_m and resistance R_m. Figure 46 is identical to Fig. 2 in Ref. [39], which was the monopolar power supply because half part of the PWM inverter was defunct until the summer of 2016. However, it has been working as a bipolar power supply since the fall of 2016 by making the PWM inverter fully function.

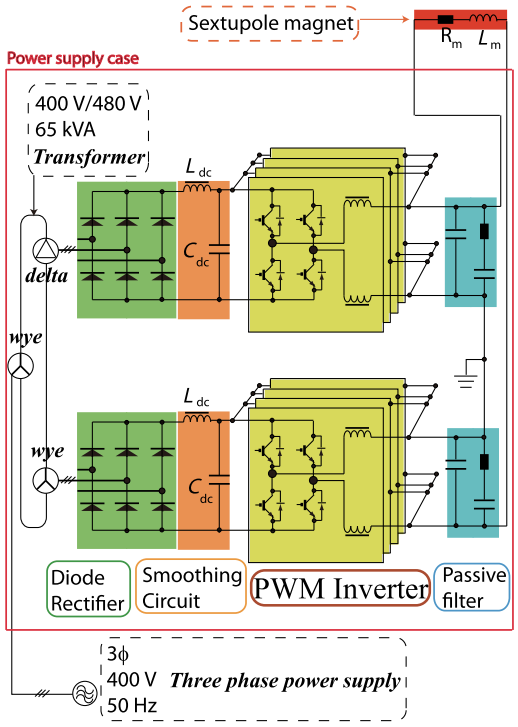

(a)

Parameters	Value
Peak output voltage	1100 V
Peak output current	750 A
Repetition rate	25 Hz
dc inductance (L_{dc})	10 mH
dc capacitance (C_{dc})	264 mF
Magnet resistance (R_m)	132 mΩ
Magnet inductance (L_m)	19.3 mH

(b)

FIG. 46. Bipolar power supply for a sextupole magnet [39]. (a) System configuration. (b) Parameters.

Figure 47 shows the time dependence of two kinds of measured input current (left) for a sextupole magnet and the calculated horizontal absolute chromaticity (right) by using the same colored data as the input parameter, where the chromaticity ($Q\xi_x$) is determined by the tune shift as a function of the relative momentum of the beam during the ramping time (20 ms). The natural chromaticity is −9 at RCS.

The blue line in the left panel activates the sextupole magnet to suppress the beam instability. As the blue line in the right panel shows, the chromaticity is corrected by half using a dc power supply from 0 to 5 ms. Subsequently, from 5 to 10 ms, the sextupole magnets yield targeting a 1.15 times increase of the chromaticity in the negative direction at 10 ms, before it tries to synchronize with $B\rho$-curve from 10 to 20 ms (but fails to rigorously do it). We can identify the zero crossing occurs around 7 ms in the left panel, changing the polarities of the magnet, while the absolute value of chromaticity starts getting larger than that of natural chromaticity in the negative direction at that time in the right panel. This manipulation of the chromaticity

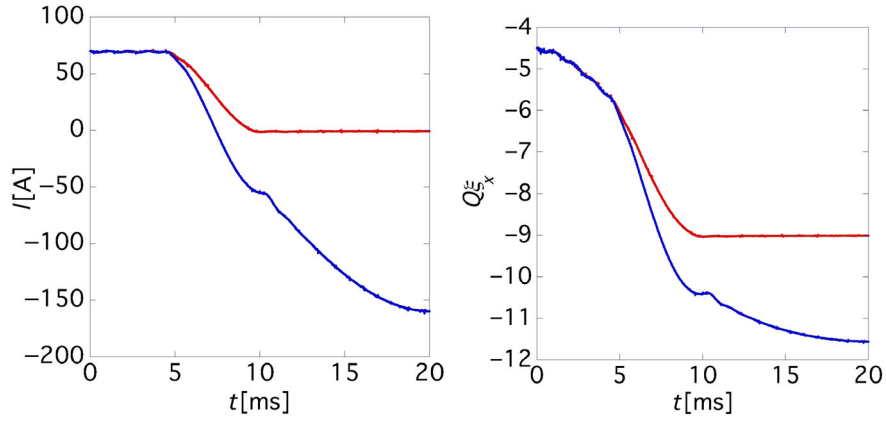

FIG. 47. Time dependence of two kinds of measured current (left) of a sextupole magnet and the calculated horizontal absolute chromaticity ($Q\xi_x$) by using the same colored data as the input parameter.

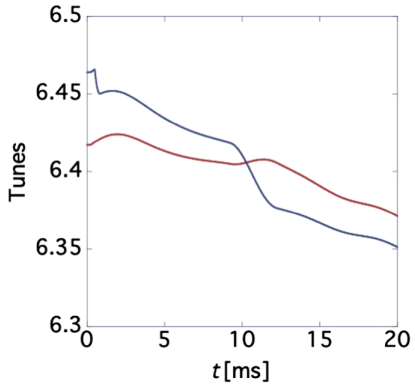

FIG. 48. Designed horizontal (blue) and vertical (red) tune tracking with a programmed tune during the acceleration (calculation).

leads to the suppression of the horizontal beam instability caused by the kicker for the smaller transverse emittance beams.

Two bunched beams are accelerated, following the tune tracking with a programmed tune as shown in Fig. 48 associated with beam delivery to the MR, where the blue and the red lines represent the horizontal and vertical tunes, respectively. Figure 49 shows the reference measurements of the transverse beam position without transverse instability in the case of the number of particles per pulse: 8.1×10^{13}, where the left and right panels show the horizontal and vertical beam positions, respectively. The monitored positions (centroid) do not precisely observe the beam behavior during the first 0.5 ms since the LINAC beams are injected and accumulated in the RCS while transverse painting is performed in the process. That is, the large peak around 0.5 ms does not describe beam instability in the horizontal direction.

Most beam position monitors (BPMs) along the RCS have two pairs of electrodes (in total four electrodes) whose shape is diagonal cut to secure a good linear response for the beam position [40]. The cutoff frequency is pushed down below half of the highest revolution frequency, typically 400 kHz, by inserting matching transformers between the detector heads and the coaxial cables with a characteristic impedance of 50 Ω. The BPM signal processing unit implements a 40 MS/s analog-to-digital converter to record waveform data to measure turn-by-turn beam centroid (beam orbits), provided after the recorded waveform data are analyzed following the procedure explained in Sec. III in Ref. [33].

Figure 50 shows the bunching factor, which is defined as the average beam current divided by the peak current, during the ramping time, where the longitudinal painting is performed until 7 ms by turning on the second harmonic of rf cavity [31,32]. H^- beam from LINAC is accumulated in the RCS during the first 0.5-ms injection time after a carbon-exchange foil to produce high intensity proton beams.

The red and blue lines in the left panel of Fig. 50 show one measurement each time of the bunching factor without and with the diode unit, respectively, where the number of particles per pulse is 8.1×10^{13}. The right panel describes the result without the diode units subtracting the result with it. Since the two bunching factors are almost overlapped in the left panel, the overall longitudinal beam shape is not significantly affected after the attachment of the diode unit. More closely, the right results illustrate that the high-frequency component in the beam without the diode unit, especially during the longitudinal painting process, is eliminated by attaching the unit, indirectly demonstrating the diode unit is effective to suppress the longitudinal impedance, as well [14].

Now, we change the chromaticity tracking pattern by activating the sextupole magnet as in the red line in the left panel of Fig. 47 to excite the beam instability. On the red line in the right panel of Fig. 47, the chromaticity is corrected by half using a dc power supply from 0 to 5 ms, before the sextupole magnets are gradually turned off so that the chromaticity becomes the natural chromaticity after 10 ms.

Figure 51 shows the overlaid results of each of three consecutive measurements (red, blue, and black) of the

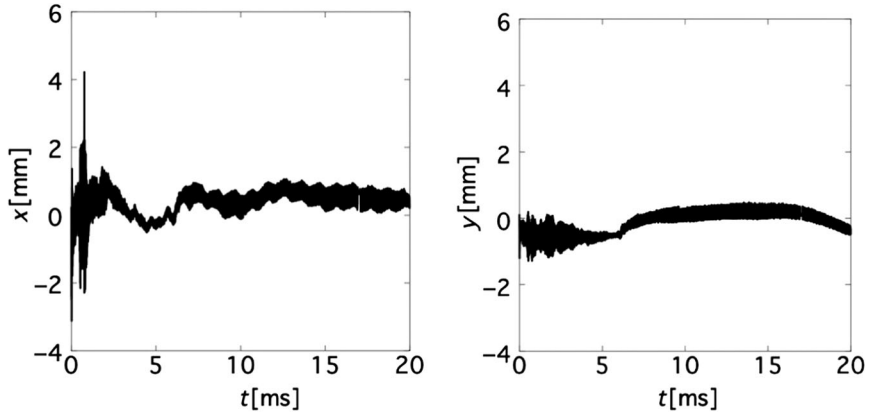

FIG. 49. Reference measurements of the transverse beam position without the diode unit (number of particles per pulse: 8.1×10^{13}).

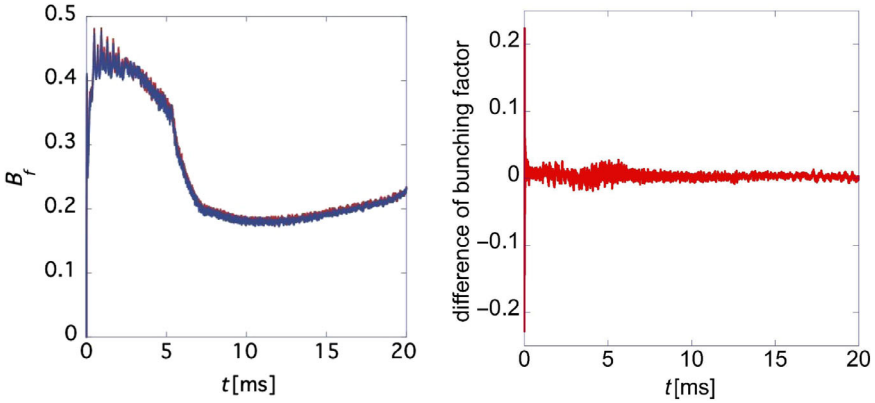

FIG. 50. Comparison of the measured bunching factors with (blue) and without (red) the diode units (number of particles per pulse: 8.1×10^{13}). The left panel shows the overlaid results, while the right panel shows the result without the diode units subtracting the result with it.

transverse beam position (number of particles per pulse: 8.1×10^{13} each, unaveraged). The left and the right panels show the results without and with diode units, respectively, while the upper and lower panels describe the horizontal and vertical beam positions, respectively. The horizontal beam instability starts around 11 ms during 20-ms acceleration. The vertical instability is slightly identified in the case without the diode unit (lower left) through the coupling effect of tunes. A comparison between the left and right results leads that the beam growth rate is more suppressed when the diode unit is attached to the kicker than that without the unit.

Note that the suppression of beam instability is realized in the case of the kicker with the diode unit when the

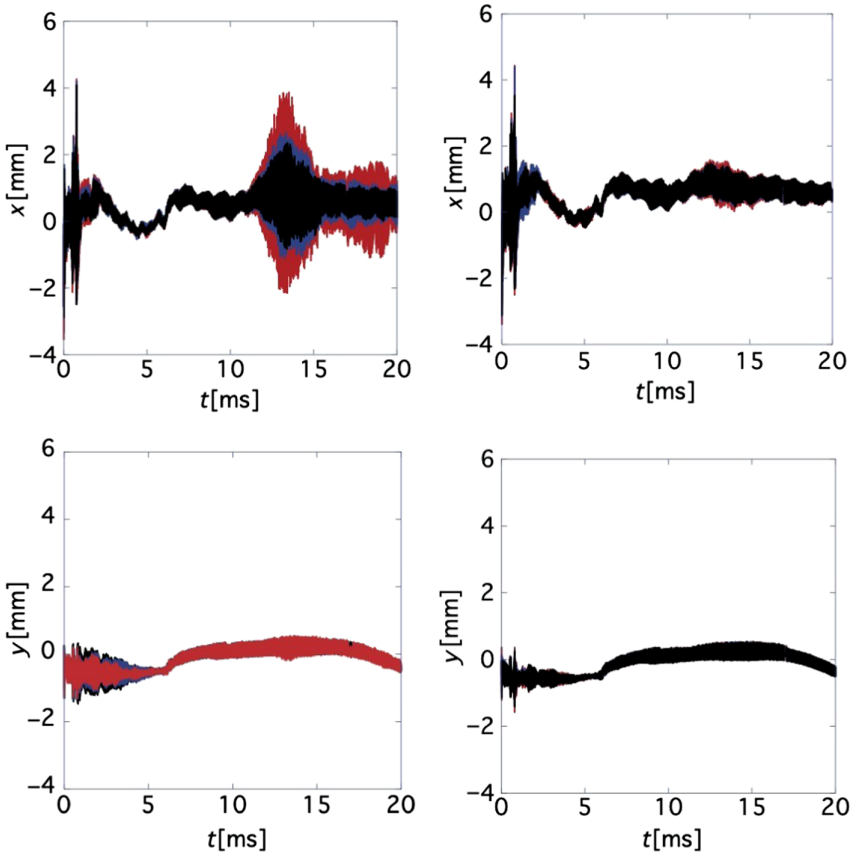

FIG. 51. Comparison of measured beam behavior before (left) and after (right) the attachment of the diode unit (number of particles per pulse: 8.1×10^{13}). The upper and lower panels show the horizontal and vertical beam positions, respectively.

unnormalized horizontal and vertical root mean square (rms) emittance at the 3-GeV extraction energy were 6.42π and 5.52π mm mrad [41], respectively, measured after five successive shots before being averaged. This achievement is remarkable to deliver higher intensity beams with smaller emittance to the MR because the beam growth rate tends to be more suppressed for high-intensity beams with larger emittance, thanks to the indirect space-charge effects, having been realized without any manipulation of the bipolar power supply in the space-charge-dominated machine like in the RCS [6].

More closely, let us examine whether the measured emittance is reasonable or not. One numerical simulation result shown in Fig. 4 in Ref. [42] suggests that an unnormalized 50π mm mrad emittance beam created in the painting area following the correlated painting process broadens and saturates around 1.5 ms to 99% normalized emittance beam with 90π and 110π mm mrad in the horizontal and vertical directions, respectively. For simplicity, if we assume a Gaussian beam, 99% emittance corresponds to five rms emittance. Then, we expect the results to be extrapolated to an unnormalized emittance beam with 4.4π mm mrad horizontal and 5.4π mm mrad vertical rms emittance at the extraction energy. The estimations are in good agreement with the measurements within factor 1.5.

B. The effect of the diode unit on the extracted beam

We have already seen that the oscillation excited on the current waveform is due to the 3.1-m long 20-Ω coaxial cable attached to the diode unit (see Fig. 20). If the trajectory of the extracted beam is significantly deviated from the ideal one due to ringing effects on the current waveform, the thyratron must be redesigned with a built-in diode unit, which is a daunting task for the present RCS due to a possibility of malfunctioning of the new thyratron with significant modifications. On the other hand, when the ringing effects do not cause major errors on the extraction trajectory, the installation of the diode unit to the kicker power supply becomes a safer and easier task because we only connect the present thyratron and the diode unit with a 3.1-m long 20-Ω coaxial cable.

Hence, we need to investigate the ringing effect of the current waveform on the magnetic fields of the kicker or the trajectory of extraction beams in this section. We will find from measurements and simulations that the current exerts only a modest ringing effect on the magnetic fields or the extraction beam, resolving the concern raised in a previous study [16].

At first, we employ a simulation approach. In this approach, the circuit shown in Fig. 43 is replaced with the circuit presented in Fig. 52 (the upper and the lower panels show the cases with and without the diode unit, respectively). Note that CST STUDIO© simulation cannot implement the end-clippers, nor PFLs as the charging units.

The upper-left panel shown in Fig. 53 simulates current waveforms observed at the "A" part of Figs. 1 and 2 for the case with (blue) and without (red) the diode units, which are the inputs to produce the magnetic field in the kicker. The upper-right panel shows the magnified simulated current with the diode unit subtracting the one without it. The lower-left panel shows the BL products divided by μ_0, vacuum magnetic permeability, along the excitation time (the blue and the red lines denote the results with and without the diode unit, respectively). The lower-right panel shows the magnified simulation result of BL products divided by μ_0 with the diode unit subtracting the one without it.

We can see that the BL products (red) in the lower-left panel are modulated around the rising edge even when the diode unit is not connected to the kicker. This results from the interference between the current flows in opposite directions on two coils, in the kicker, connecting to the high voltage plates sandwiched by the ground plates and the ferrite cores (see Fig. 59 in Appendix A). Moreover, the flattop time length becomes about 1.05 μs on the BL product though it is 1.2 μs on the forward current (red) depicted in the upper left panel in Fig. 53. This blunt of the rising time is caused by the characteristic of the transmission line and combined-type kicker magnet [43].

Meanwhile, the results shown in the lower panels demonstrate that the trapezoidal magnetic fields excited by the current waveform are rather modestly affected by the current oscillation due to the diode unit, because the difference between the results with and without the diode unit is within 1% between 1.60 and 2.65 μs (flattop region). The result is consistent with the previous expectation from the simpler simulation setup by only using SPICE© [15]. Since the interference effect between the cores is more significant on the magnetic fields than the current oscillation effect due to the diode unit, the diode unit may have only a minor effect on the extraction beams from the RCS, indicating that the difference between the cases with and without the diode unit is small.

Figure 54 shows an example of the previously measured magnetic field "without the diode units," which is normalized by the flattop value during the excitation time, corresponding with 20-kV charging voltage [43,44]. The measured absolute value of the flattop field is consistent with the expected value of $\mu_0 I_c/g_p$ ($\simeq$0.0147 T in the case of Fig. 54) within 10% difference, where g_p is the gap height and I_c is the superposed current due to the short plates in the left- (or right-) hand side of the kicker [45]. This ambiguity is caused by the systematic error intrinsic to the circuit constant of the measurement system [9], though the magnetic field is linearly response to the coil current (or charging voltage of the PFL).

There are in total eight kicker magnets at the extraction section in the RCS. To more precisely detect this field modulation on the kicker fields, it is noticeable that the ringing on the flattop fields of the kicker magnets displaces

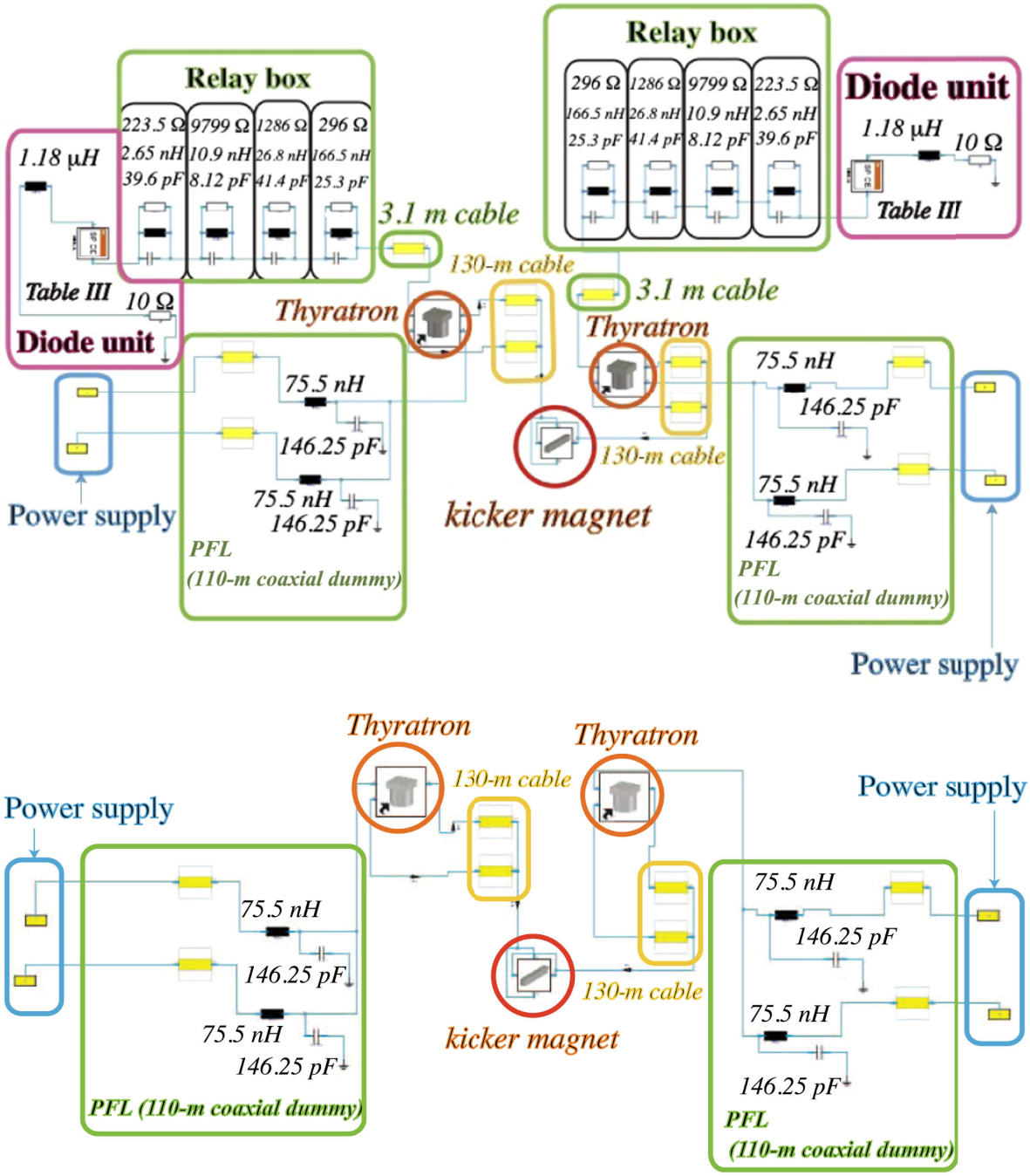

FIG. 52. Electric circuit part on CST STUDIO©. The upper and lower panels show the cases with and without the diode unit, respectively. Note "kicker magnet" part is a realistic model as in the simulation of Fig. 43.

the extracted beam horizontally from the ideal trajectory at the downstream beamline of the RCS. In the RCS, there are two kinds of trigger systems for the kicker power supply. One timing module controls the entire trigger timing of the thyratrons for all eight kicker magnets, while the other timing module does the individual trigger timing for the respective kicker magnets. The degree of field flatness for one kicker was found via the beam position shift measured by a beam position monitor installed at the downstream beamline of the RCS when the trigger timing for the assigned kicker pulse was changed step by step [44]. In this measurement, the longitudinal beam width was chopped to be very short, about 30 ns in the full width at the extraction energy before 10 times averaged under full chromaticity correction, while a typical bunch width is 180 ns in user operation.

Figure 55 shows the trajectory modulation (closed circle) caused by only the assigned kicker in the RCS (though all

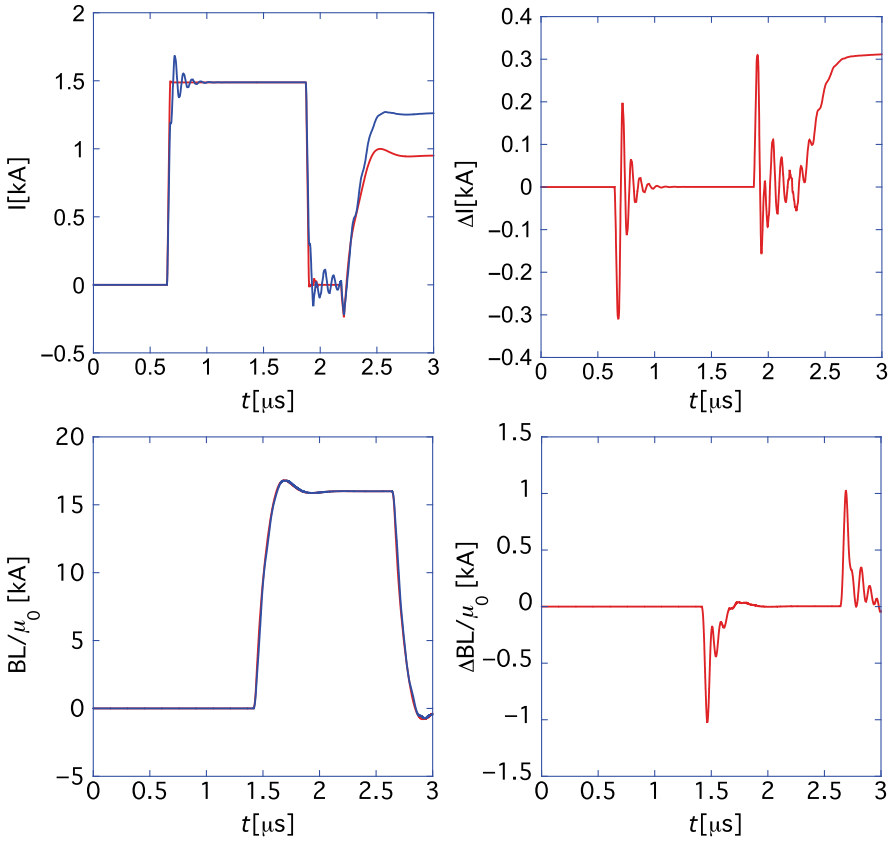

FIG. 53. The upper-left panel shows the simulated current waveforms observed at the "A" part of Figs. 1 and 2 for the case with (blue) and without (red) the diode units. The upper-right panel shows the magnified simulated current with the diode unit subtracting the one without it. The lower-left panel shows the simulated BL products divided by μ_0 along the excitation time (the blue and the red lines denote the results with and without the diode unit, respectively). The lower-right panel shows the magnified simulation result of BL products divided by μ_0 with the diode unit subtracting the one without it.

eight kickers contribute to the trajectory modulation, the contribution from respective kickers can be distinguished by scanning the individual trigger timings kicker by kicker [44]). The result revealed the field modulations can be identified by the measurements. The magnetic field modulation effect (excited by the interference between the coils in the left- and right-hand sides of the kicker) in the case without a diode unit [43] was observed directly via the trajectory modulation of the extraction beams with the short longitudinal length [44].

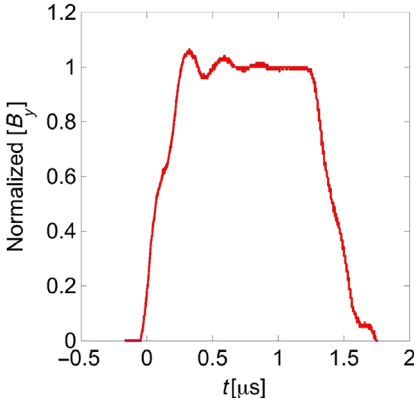

FIG. 54. The kicker magnetic field normalized by the flattop value during the excitation time without the diode units (measurement) [43].

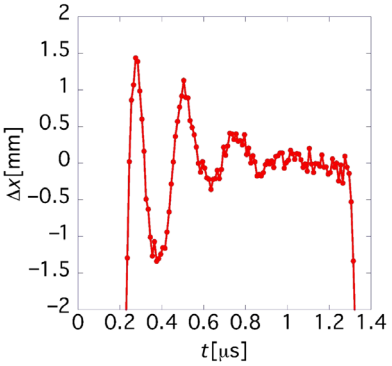

FIG. 55. Trajectory modulation of the beams (closed circle) caused by the assigned kicker, monitored by BPM at the downstream line of the RCS when the diode units are absent (measurement).

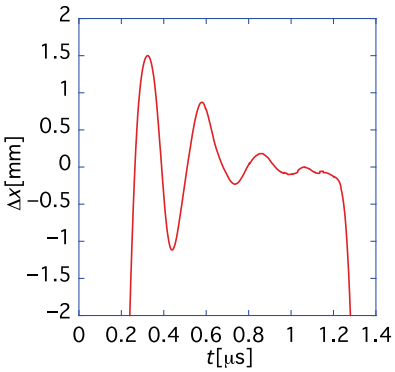

FIG. 56. Reproduction of the beam trajectory deviation monitored by BPM at the downstream line of the RCS when the diode units are absent (calculation).

Prior to the measurement "with the diode unit," we roughly estimate the trajectory modulation of extraction beams resulting from the diode units in an analytical manner by using the previously measured data, such as Fig. 16, the right panel of Figs. 18 and 54. The magnetic field fluctuation (interference effect) in Fig. 54 attributes to the structure of the magnet and the mutual inductance between the coils. Hence, the current and the magnetic field should be considered in Fourier space so that we introduce

$$\mu_0 H(t) = B(t) = \int_{-\infty}^{\infty} \frac{d\omega e^{-j\omega t}}{2\pi} \mathcal{F}(\omega)\mathcal{I}(\omega), \quad (40)$$

$$\mathcal{I}(\omega) = \int_{-\infty}^{\infty} dt e^{j\omega t} I(t), \quad (41)$$

where $I(t)$ is the forward current on the waveform and $\mathcal{F}(\omega)$ is a form factor, which is obtained after dividing the Fourier-transformed magnetic field (Fig. 54) by that of the current (Fig. 16) associated with the no-diode case.

For simplicity, we assume that the field modulation on the flattop magnetic fields can be related to the trajectory deviation Δx from the ideal one observed at a monitor at the downstream beamline as follows:

$$\Delta x = r_m \left(\frac{B(t)L}{B\rho} - \frac{B(t_0)L}{B\rho} \right), \quad (42)$$

with fixed beam optics, where t_0 is a specific time in the latter half on the flattop of the trapezoidal magnetic field pattern, where the field fluctuations are settled (here, we choose $t_0 = 1$ μs). The parameter r_m is determined for the reproduction of the maximum value (1.5 mm) in Fig. 55. Figure 56 shows the calculated Δx, which provides a good description of the measured trajectory deviation (see Fig. 55) without the diode unit.

Now, all parameters are determined. Hence, we can evaluate Δx with the diode unit by Eq. (42), after substituting the measured $I(t)$ (the red line in the right panel of Fig. 18) into Eq. (40). The left panel of Fig. 57 shows the calculation results, where the red and blue lines denote the cases with and without the diode unit, respectively. This figure predicts that the oscillation effects due to the diode unit on the trajectory modulation are not significant as expected, but that a chip appears on the latter part of the trapezoidal magnetic field when the diode unit is attached to the thyratron, which is absent from the simulation results shown in the lower-left panel of Fig. 53.

The right panel of Fig. 57 shows the 10 times averaged measured trajectory (closed circle), at the downstream line, of the extracted beams with about 30-ns longitudinal full width, where one bunch beam with 8.5×10^{11} particle per bunch is accelerated under full chromaticity correction. The arrival timings and widths of the first and second bunches under the user operation are specified with the dashed lines.

The measured maximum amplitude ranges from approximately 1.5 to 2 mm for the case with the diode unit. The difference between the cases with and without the diode unit was within 0.6 mm. Though the analytical result underestimates the measured deviation, it has excellence

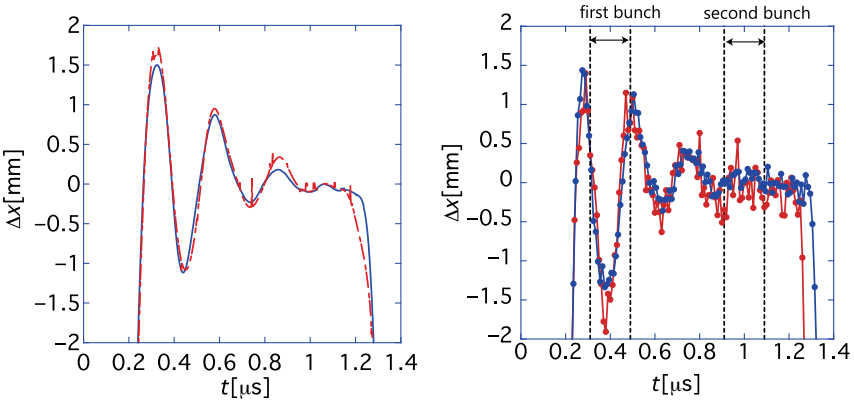

FIG. 57. Comparison of the deviation of the extracted beam positions with (red) and without (blue) diode units. The left and right panels show the calculations and the measurements (closed circle). The arrival timings and widths of the first and second bunches under the user operation are specified with the dashed lines.

featuring the oscillation on the fields which was overlooked in the simulation results in the lower-left panel of Fig. 53.

At the RCS, the effective flatter trapezoidal field is produced during the extraction time for user operation by adjusting the thyratron timings among eight kickers. Hence, the diode unit does not have a significant effect on the first bunch (among the beam pulse) from a practical point of view, as suggested by the simulation and calculation results, because the modulation can be compensated by appropriately adjusting the thyratron timings to create the effective flatter flattop as being done in the case without the diode unit.

On the other hand, the measurements demonstrate the chip on the latter part of the waveform to shorten the flattop time range by ∼50 ns (but still 150 ns left for the second bunch), as expected by the analytical calculations. Such shortening represents one drawback of this impedance reduction method. However, this drawback did not cause any critical difficulty at the RCS to correctly extract beams, because the effective flatter trapezoidal field was produced by delaying the thyratron timings for the assigned kicker with the diode unit.

When the diode unit is absent, the effective flatter trapezoidal field is produced by delaying the thyratron timings for six designated kickers so that six diode units can be installed into the RCS without any special adjustment of the timing associated with the extraction beams by assigning the kickers as the ones with diode units.

Presently, a simulation result suggests that the beam can be delivered to the MR with beam instability being suppressed and without any restriction on the tunability in the tune diagram of the RCS if at least four diode units are installed into the RCS. However, it is necessary to readjust all thyratron timings for all eight kickers to extract two bunches within tolerable displacement by making use of the remained available flattop length on the trapezoidal fields of the respective kickers when we attach the diode unit to all kickers to realize 1.5 MW, or more, beam power at the RCS in the future [7].

Finally, let us estimate how degree of the current modulation day to day at the rising edge, illustrated in Fig. 24 in Sec. IV B, could affect the trajectory of the extracted beam. The trajectory deviation of the extracted beam is calculated following the analytical manner explained above after changing the input current in Eq. (41) to those in Fig. 24. As the results in Fig. 58 show, we expect that the trajectory deviation caused by the current modulation day to day is the same level as shown in the right panel of Fig. 57 and small compared to the amount of the original trajectory displacement caused by the intrinsic structure of the kicker magnet.

As already demonstrated in Fig. 37, we successfully performed an 830-kW beam user operation for 45 days with the diode unit attached to one designated kicker (among the six) without any significant trajectory deviations for the extracted beams and any special adjustment of the timing of the assigned kicker pulse associated with the extraction beams.

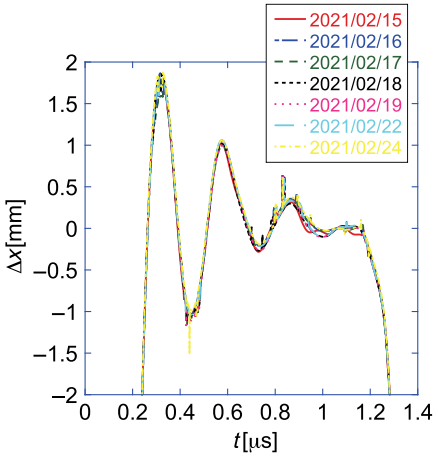

FIG. 58. Estimation of beam trajectory fluctuations day to day monitored at the downstream line of the RCS (calculation).

IX. SUMMARY

In a previous study, we demonstrated that the kicker impedance can be reduced by inserting diodes and resistors at the switch end of the coaxial cables. The scheme ensures doubled excitation currents for the extraction beam by inverting the voltage wavefront and superposing the excitation currents with two shorted ends, which is beneficial for power saving. The resistors are isolated from the switch cathode but can be seen by high-intensity beam-induced currents, thereby reducing the kicker impedance.

However, a few concerns have been raised in Ref. [16]. (1) A current ripple, which may be unacceptable for the extraction beam, occurs with the rising edge of the current waveform. (2) The fast-rising voltage across the diodes during turn-on of the thyratron switch may lead to the degradation of the diode stack, thereby affecting the durability of the stack.

To address these concerns, we have improved the diode unit considerably by scrapping the capsule of the prototype diode module consisting of minidiodes and capacitors and increasing the parallel branch of the minidiodes. The new diode unit consists of 30 parallel and 27 series minidiodes, although the prototype diode unit consists of 24 parallel and 26 series minidiodes.

Thanks to this improvement, the durability of the diode stack has improved, as demonstrated by a 45-day 830-kW beam operation after a 12-day preliminary test operation. These results are supported by simulations with ANSYS FLUENT© and analytical analysis. The specification for the diode unit requires that the surface temperature should be below 85 °C for the minidiode comprising the diode part and 150 °C for 250-Ω cylindrical resistors composing the

10-Ω part. These criteria would be sufficiently satisfied even when a 25-Hz 5-MW operation was conducted.

Moreover, increasing the number of parallel branches in the diode part has reduced the kicker impedance significantly to a level comparable to that of the case with only a matched resistor attached to the kicker. The kicker impedance reduction by this improved diode unit is demonstrated by measurements and simulations with CST STUDIO©.

The beams extracted from the RCS are delivered to the MR through the beam extraction line with a small mechanical aperture, exciting a large residual dose in the area. To cure the situation, the beam with a smaller emittance is preferable to minimize losses for a given aperture. Hence, we created a beam with 6.42π mm mrad horizontal and 5.52π mm mrad vertical rms unnormalized emittance at the extraction energy by using 50π mm mrad correlated painting scheme because the RCS manipulates the transverse painting area from 0 to 200π mm mrad at the injection energy both in the horizontal and vertical directions [34].

Owing to the impedance reduction, the unit, although attached to only one extraction kicker among eight kickers in the RCS, has significantly suppressed the beam instabilities, even when the horizontal and vertical root mean square unnormalized emittance are 6.42π mm mrad and 5.52π mm mrad, respectively, at the 3-GeV extraction energy. This achievement is of great importance to extend the parameter windows in the tune diagram of the RCS for future higher power operation of the MR because the beam growth rate for smaller emittance beams is more enhanced in the space charge-dominated beam like in the RCS, as we already demonstrated the emittance dependence of the beam growth rate by using a 1-MW beam from both theoretical and measurement points of views [6].

We have demonstrated that the current ripple caused by the diode unit in the rising time of the current waveform has a minor effect on the extraction beam, which is predicted by simulations with CST STUDIO©, and more consistent with an analytical estimate. The result reveals that the coupling effects resulting from mutual inductances between two coils could (compared with the ripple caused by the diode unit) have a more significant effect on the exciting magnetic field or the extraction beams from the RCS.

Though the effect of a current ripple is not so significant on the extraction beam at the RCS from a practical point of view, the diode unit would be better integrated into the thyratron section from the beginning than at a subsequent stage from the viewpoint of designing the kicker power supply, because the effect is excited by a 3.1-m long 20-Ω coaxial cable connecting the diode unit and the thyratron of the kicker.

ACKNOWLEDGMENTS

The authors gratefully acknowledge Mr. Isamu Koizumi from NAT [46] for his support in conducting the measurements. They would like to thank Dr. Junichiro Kamiya for kindly providing the previous data on the magnetic field pattern (Fig. 54). They would like to appreciate the contribution to the J-PARC project at JAEA/KEK from all members of the J-PARC Accelerator Technical Advisory Committee, which was led by Dr. Steve Holmes and Dr. Thomas Roser until 2009 and 2018, respectively, and has been led by Dr. Jie Wei since 2019. They would like to express gratitude to all members of the J-PARC Center.

APPENDIX A: PARAMETERS OF THE PRESENT KICKER MAGNET

As shown in Fig. 1, the kicker consists of a magnet and two PFLs. Aluminum (Al) coils are embedded in the kicker magnet, which is a window-frame transmission-line type consisting of two ferrite cores, each of 9.8-Ω characteristic impedance.

The characteristic impedance Z_{cable} of the power cable and the wave propagation speed v_{cable} in the power cable are 22.6 Ω and $0.57 \times c$ m/s, respectively. The combined resistivity R_{cable} of the inner and outer conductors in the cable, and the conductance G of the insulator between the conductors, are given as follows:

$$R_{\mathrm{cable}} = \frac{1}{2}\left(\frac{1}{a_{\mathrm{cable}}} + \frac{1}{b_{\mathrm{cable}}}\right)\sqrt{\frac{Z_0 f}{c\pi\sigma_c}}, \tag{A1}$$

$$G = 2\pi f \mathcal{C}_{\mathrm{cable}} \tan\delta, \tag{A2}$$

[11], where $\mathcal{C}_{\mathrm{cable}} = 1/(v_{\mathrm{cable}} Z_{\mathrm{cable}})$ is the capacitance of cable per unit length, f is the frequency, c is the velocity of light, $Z_0 = 120\pi$ Ω is the impedance of free space. In addition, $a_{\mathrm{cable}} = 9.1$ mm and $b_{\mathrm{cable}} = 15$ mm are the radii of the inner and the outer conductors of the cable, respectively, $\sigma_c = 4.48 \times 10^7$ S/m is the conductivity of the conductors, and $\tan\delta = 0.018$ is $\tan\delta$ of the insulator between the conductors.

A photograph and a schematic of the kicker are shown in Fig. 59, where $2a = 280$ mm, $2b = 199$ mm, $2\rho_p = 48$ mm, $2\rho_w = 4$ mm, and $B - b = 70$ mm. The kicker magnet consists of aluminum alloy components (high voltage plates, a flux break, grounding plates, and a vessel) and ferrite (Ni-Zn ferrite PE14, TDK Ltd. [47]) components. Aluminum coils and the high voltage plates are electrically connected, while the flux break and the grounding plates are attached to the vessel in which they are housed. The ferrite is sandwiched by the plates. The relative permeability μ' of the ferrite is approximated as

$$\mu' = 7.0 + \frac{800.0}{1.0 + j2\pi f\tau}, \tag{A3}$$

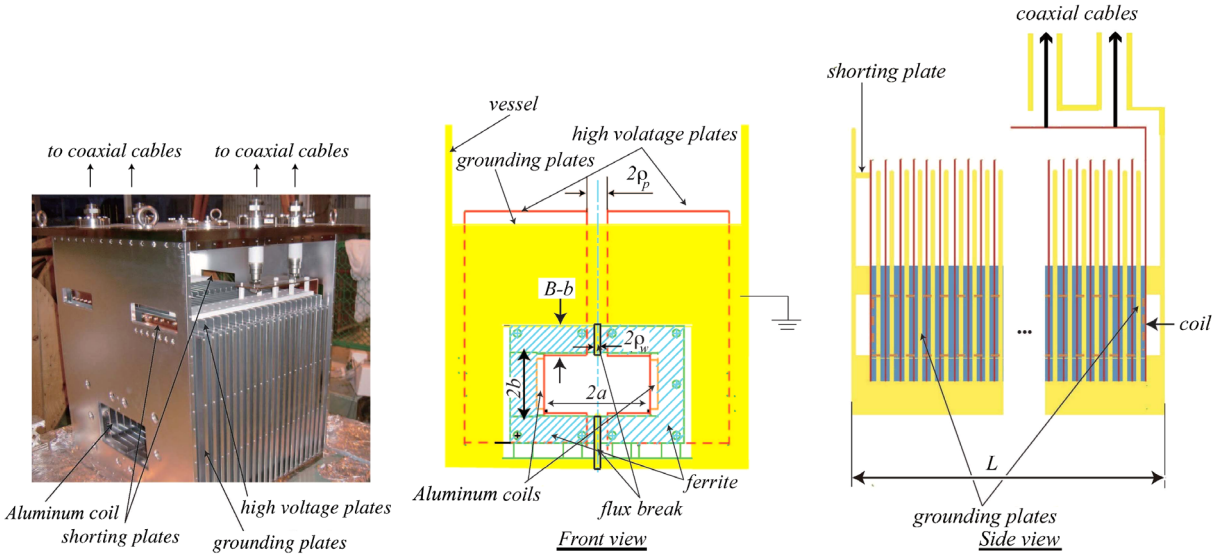

FIG. 59. A photograph (left) and illustrations (middle/right) of the RCS kicker in J-PARC.

where j is an imaginary unit, and the relaxation time $\tau = 1.59155 \times 10^{-7}$ s. The relative dielectric constant ϵ' of the ferrite is equal to 6.2, regardless of the frequency [11].

APPENDIX B: THE KICKER IMPEDANCES WITH COAXIAL CABLES, THE ENDS OF WHICH ARE TERMINATED BY THE IMPEDANCE R_T

The horizontal impedance Z_x including Lorentz β dependence but excluding the space-charge impedance is derived in Ref. [11] as

$$Z_x = Z_x^{(1)} + Z_x^{(crr)}, \tag{B1}$$

with

$$Z_x^{(1)} = -\frac{c\beta\theta_3 Z_{c,d}(e^{j(k+\omega\theta_3)L}-1)}{qa(k+\omega\theta_3)}\frac{dF_1}{dx_0}\bigg|_{x_0=0} - \frac{c\beta\theta_3 Z_{c,d}(e^{j(k-\omega\theta_3)L}-1)}{qa(k-\omega\theta_3)}\frac{dF_2}{dx_0}\bigg|_{x_0=0} + \frac{jc\beta L}{a}\frac{dM_-}{dx_0}\bigg|_{x_0=0}, \tag{B2}$$

$$Z_x^{(crr)} = -\frac{L_f}{ka}\sum_{m=1}^{\infty}\left(\frac{dE_m^{\gamma}}{dx_0}\bigg|_{x_0=0} - \frac{jkk'_{xm}Z_0\tanh[k_{xm}b]\cos[k'_{xm}a]}{2\beta\gamma^2 k_{xm}}\right)k'_{xm}\cos[k'_{xm}a], \tag{B3}$$

where c is the velocity of light; β is Lorentz-β; γ is Lorentz-γ; $\omega = 2\pi f$ is the angular frequency; $k = \omega/c\beta$; q is the charge of a bunch in the beam; $L(= 638$ mm) is the total length of the kicker; $L_f(= 500$ mm) is the total length of the ferrite component of the kicker; $2a$ and $2b$ are the gap width and gap height, respectively; x_0 is the horizontal position of the beam;

$$\theta_3 = \sqrt{(L_k - M_b)C_k}, \tag{B4}$$

$$Z_{c,d} = \sqrt{\frac{(L_k - M_b)}{C_k}}, \tag{B5}$$

$$M_-(x_0) = \frac{[M^r(x_0) - M^l(x_0)]}{2[1 - c^2\beta^2(L_k - M_b)C_k]}, \tag{B6}$$

$$\left.\frac{dE_m^{\gamma}(x_0)}{dx_0}\right|_{x_0=0} = \frac{\frac{jkk'_{xm}Z_0\cos[\frac{m\pi}{2}]}{2\beta\gamma^2 k_{xm}}}{\left[\frac{k'^2_{xm}}{k^2_{xm}} - \frac{\left(1-\frac{\mu' k'_{ym}\tanh[k'_{ym}(b-B)]\tanh[k_{xm}b]}{\gamma^2(1-\beta^2\epsilon'\mu')k_{xm}}\right)\left(1-\frac{\frac{\epsilon' k'_{ym}\cosh[k'_{ym}(b-B)]}{\tanh[k'_{ym}(b-B)]}}{\gamma^2(1-\beta^2\epsilon'\mu')k_{xm}\sinh[k_{xm}b]}\right)}{(1-\frac{1}{\gamma^2(1-\beta^2\epsilon'\mu')})(1-\frac{\mu'\epsilon'}{\gamma^2(1-\beta^2\epsilon'\mu')})}\right]}$$
$$\times\left[\frac{k'^2_{xm}\tanh[k_{xm}b]}{k^2_{xm}} - \frac{\left(1-\frac{\mu' k'_{ym}\tanh[k'_{ym}(b-B)]}{\gamma^2(1-\beta^2\epsilon'\mu')k_{xm}}\right)\left(1-\frac{\epsilon' k'_{ym}\tanh[k_{xm}b]}{\gamma^2(1-\beta^2\epsilon'\mu')k_{xm}\tanh[k'_{ym}(b-B)]}\right)}{\tanh[k_{xm}b](1-\frac{1}{\gamma^2(1-\beta^2\epsilon'\mu')})(1-\frac{\mu'\epsilon'}{\gamma^2(1-\beta^2\epsilon'\mu')})}\right], \tag{B7}$$

$$k'_{xm} = \frac{m\pi}{2a}, \tag{B8}$$

$$k_{xm} = \sqrt{k'^2_{xm} + \frac{k^2}{\gamma^2}}, \tag{B9}$$

$$k'_{ym} = \sqrt{k'^2_{xm} + k^2(1-\epsilon'\mu'\beta^2)}, \tag{B10}$$

ϵ' and μ' are the relative dielectric constant and the relative permeability of the ferrite, respectively; $Z_0(=120\,\pi\,\Omega)$ is the impedance of free space; the parameter $C_k(=13.62\ \mathrm{nF/m})$ is the capacitance of the kicker per unit length; and $B-b$ is the thickness of the ferrite (see Fig. 59).

The parameters L_k and M_b, which are the self-inductance of the kicker per unit length and the mutual inductance between the coils per unit length, respectively, are calculated as follows:

$$L_k = -\frac{\mu_0}{4b}\left[-\frac{K_1(x_1)}{\sin[\frac{2\omega a}{c}]} + \frac{K_2}{\sin[\frac{\omega a}{c}]} + \sum_{m=1}^{\infty}\frac{(1+(-1)^m)K_3}{\sinh[\theta_{m0}a]}\right], \tag{B11}$$

$$M_b = -\frac{\mu_0}{4b}\left[-\frac{K_1(x_2)}{\sin[\frac{2\omega a}{c}]} + \frac{K_2}{\sin[\frac{\omega a}{c}]} + \sum_{m=1}^{\infty}\frac{(1+(-1)^m)K_3}{\sinh[\theta_{m0}a]}\right], \tag{B12}$$

where

$$K_1(x_i) = -\frac{c}{\omega}\left\{\cos\left[\frac{\omega(a+x_i)}{c}\right] - \cos\left[\frac{\omega(\rho_w+x_i)}{c}\right]\right\} - \frac{c}{\omega}\left\{\cos\left[\frac{\omega(x_i+a)}{c}\right] - \cos\left[\frac{\omega(|x_i-\rho_w|-2a)}{c}\right]\right\}, \tag{B13}$$

$$K_2 = -\frac{c}{\omega}\left[1-\cos\frac{\omega(\rho_w-a)}{c}\right], \tag{B14}$$

$$K_3 = \frac{1-\cosh[\theta_{m0}(\rho_w-a)]}{\theta_{m0}}, \tag{B15}$$

$$\mu_0 = \frac{Z_0}{c}, \tag{B16}$$

$$\theta_{m0} = \sqrt{\frac{m^2\pi^2}{4b^2} - \frac{\omega^2}{c^2}}, \tag{B17}$$

$$x_1 = a, \tag{B18}$$

$$x_2 = -a, \tag{B19}$$

and ρ_w is the half width of the flux break (see Fig. 59).

The parameters $M^r(x_0)$ and $M^l(x_0)$ are the induction coefficients between the beam and the right coil and between the beam and the left coil, respectively, and are calculated from

$$M^r(x_0) = -\frac{\mu_0}{4b}\left\{-\frac{K_1(x_0)}{\sin[\frac{2\omega a}{c}]}+\frac{K_2}{\sin[\frac{\omega a}{c}]}+\sum_{m=1}^{\infty}\left[-\frac{2(-1)^m\cos[\frac{m\pi}{2}]K_4(x_0)}{\mathrm{sh}[2\theta_{m0}a]}+\frac{(1+(-1)^m)K_3}{\sinh[\theta_{m0}a]}\right]\right\}, \tag{B20}$$

$$M^l(x_0) = M^r(-x_0), \tag{B21}$$

where

$$K_4(x_0) = \frac{\cosh[\theta_{m0}(a+x_0)]-\cosh[\theta_{m0}(\rho_w+x_0)]}{\theta_{m0}}+\frac{\cosh[\theta_{m0}(x_0+a)]-\cosh[\theta_{m0}(|x_0-\rho_w|-2a)]}{\theta_{m0}}. \tag{B22}$$

The functions $F_1(x_0)$ and $F_2(x_0)$ are determined by solving

$$\begin{aligned}&(Z_{c,d}-\mathcal{Z}_{\mathrm{cable}})F_1-(Z_{c,d}+\mathcal{Z}_{\mathrm{cable}})F_2-(Z_{c,c}-\mathcal{Z}_{\mathrm{cable}})F_3+(Z_{c,c}+\mathcal{Z}_{\mathrm{cable}})F_4\\&\quad=-(M_-+M_+)qc\beta-\mathcal{Z}_{\mathrm{cable}}qC_kc^2\beta^2(M_-+M_+),\end{aligned} \tag{B23}$$

$$-Z_{c,d}F_1+Z_{c,d}F_2-Z_{c,c}F_3+Z_{c,c}F_4 = qc\beta(M_--M_+), \tag{B24}$$

$$Z_{c,d}e^{j\omega\theta_3L}F_1-Z_{c,d}e^{-j\omega\theta_3L}F_2-Z_{c,c}e^{j\omega\theta_1L}F_3+Z_{c,c}e^{-j\omega\theta_1L}F_4 = -(M_-+M_+)qc\beta e^{-j\omega\frac{L}{c\beta}}, \tag{B25}$$

$$\begin{aligned}&-(Z_{c,d}+\mathcal{Z}_{\mathrm{cable}})e^{j\omega\theta_3L}F_1+(Z_{c,d}-\mathcal{Z}_{\mathrm{cable}})e^{-j\omega\theta_3L}F_2-(Z_{c,c}+\mathcal{Z}_{\mathrm{cable}})e^{j\omega\theta_1L}F_3+(Z_{c,c}-\mathcal{Z}_{\mathrm{cable}})e^{-j\omega\theta_1L}F_4\\&\quad=(M_--M_+)qc\beta e^{-j\omega\frac{L}{c\beta}}-\mathcal{Z}_{\mathrm{cable}}(M_--M_+)qC_kc^2\beta^2e^{-j\omega\frac{L}{c\beta}},\end{aligned} \tag{B26}$$

for $F_1(x_0), F_2(x_0), F_3(x_0)$, and $F_4(x_0)$, where

$$M_+(x_0) = \frac{[M^r(x_0)+M^l(x_0)]}{2(1-c^2\beta^2(L_k+M_b)C_k)}, \tag{B27}$$

$$\theta_1 = \sqrt{(L_k+M_b)C_k}, \tag{B28}$$

$$Z_{c,c} = \sqrt{\frac{(L_k+M_b)}{C_k}}. \tag{B29}$$

$$\mathcal{Z}_{\mathrm{cable}} = \frac{1}{2}\sqrt{\frac{L_{\mathrm{cable}}}{C_{\mathrm{cable}}}}\frac{\left(1+\frac{-\sqrt{\frac{L_{\mathrm{cable}}}{C_{\mathrm{cable}}}}+2\hat{R}_T}{\sqrt{\frac{L_{\mathrm{cable}}}{C_{\mathrm{cable}}}}+2\hat{R}_T}e^{-j\omega2\sqrt{C_{\mathrm{cable}}L_{\mathrm{cable}}}l_{\mathrm{cable}}}\right)}{\left(1+\frac{-\sqrt{\frac{L_{\mathrm{cable}}}{C_{\mathrm{cable}}}}+2\hat{R}_T}{-\sqrt{\frac{L_{\mathrm{cable}}}{C_{\mathrm{cable}}}}-2\hat{R}_T}e^{-j\omega2\sqrt{C_{\mathrm{cable}}L_{\mathrm{cable}}}l_{\mathrm{cable}}}\right)}, \tag{B30}$$

$$\hat{R}_T = \sqrt{\frac{L_{\mathrm{cable}}}{C_{\mathrm{cable}}}}\frac{\left(1+\frac{-\sqrt{\frac{L_{\mathrm{cable}}}{C_{\mathrm{cable}}}}+R_T}{\sqrt{\frac{L_{\mathrm{cable}}}{C_{\mathrm{cable}}}}+R_T}e^{-j\omega2\sqrt{C_{\mathrm{cable}}L_{\mathrm{cable}}}l_{3.1}}\right)}{\left(1+\frac{-\sqrt{\frac{L_{\mathrm{cable}}}{C_{\mathrm{cable}}}}+R_T}{-\sqrt{\frac{L_{\mathrm{cable}}}{C_{\mathrm{cable}}}}-R_T}e^{-j\omega2\sqrt{C_{\mathrm{cable}}L_{\mathrm{cable}}}l_{3.1}}\right)}, \tag{B31}$$

The relations (B23)–(B26) describe the boundary conditions (two ends are terminated in a short circuit, while the other two are connected to the coaxial cables), where

$$L_{\text{cable}} = \mathcal{L}_{\text{cable}} + \frac{R_{\text{cable}}}{j\omega}, \tag{B32}$$

$$C_{\text{cable}} = \mathcal{C}_{\text{cable}} + \frac{G}{j\omega}. \tag{B33}$$

The quantities $\mathcal{L}_{\text{cable}}(= Z_{\text{cable}}/v_{\text{cable}})$ and $\mathcal{C}_{\text{cable}}$ are the inductance per unit length and the capacitance per unit length of the cable. The resistivity R_{cable} and the conductance G are given by Eqs. (A1) and (A2), respectively. Equation (B30) considers the case where two-parallel cables with $l_{\text{cable}}(= 130\ \text{m})$ long are connected at the kicker's ends and terminated with one electric device having the impedance $\hat{R}_T(\omega)$ [5] comprising $l_{3.1}(= 3.1\ \text{m})$ length $\sqrt{L_{\text{cable}}/C_{\text{cable}}}\ \Omega$ coaxial cable terminated by the diode unit with impedance R_T as given by Eq. (B31) and therefore differs slightly from Eq. (D.11) employed in Ref. [11] and Eq. (A34) in Ref. [14]. The results for an open circuit shown in Figs. 41 and 42 are obtained by substituting infinity for the terminal impedances $\hat{R}_T$ and R_T, respectively.

When the diode unit with voltage probe and current transformer is connected to the end of a 3.1-m coaxial cable, the beam-induced voltages across the diode unit and the current on it are measured by letting a high intensity beam pass through the kicker. Accordingly, the effective impedance R_T of the diode unit can be determined for the given beam. By substituting the value of R_T into Eq. (B31), we obtain the kicker impedances shown in Fig. 41.

In three-dimensional particle tracking simulation code, such as ORBIT [48], the space-charge effect is taken into account dynamically. Hence, the space-charge impedance [49] must be excluded from the coupling impedance exciting the beam instability as its input parameter to avoid double counting the effects in the simulation [7].

[1] K. Yamamoto *et al.*, Design and actual performance of J-PARC 3 GeV rapid cycling synchrotron for high-intensity operation, J. Nucl. Sci. Technol. **59**, 1174 (2022).

[2] J-PARC Annual Report 2014, p. 9, http://j-parc.jp/documents/annual_report/a_report_2014.pdf#zoom=100.

[3] A. W. Chao, *Physics of Collective Beam Instabilities in High Energy Accelerators* (Wiley, New York, 1993).

[4] Y. H. Chin, K. Takata, T. Toyama, Y. Shobuda, and J. Kamiya, Impedance and beam instability issues at J-PARC rings, in *Proceedings of Hadron Beam 2008, Nashville, TN*, p. 40, https://accelconf.web.cern.ch/HB2008/papers/wga01.pdf.

[5] Y. Shobuda, P. K. Saha, T. Toyama, M. Yamamoto, Y. H. Chin, and Y. Irie, The kicker impedance and its effect on the RCS in J-PARC, in *Proceedings of HB2014, MI* (2014), p. 369, https://epaper.kek.jp/HB2014/papers/tho2ab02.pdf.

[6] Y. Shobuda, Y. H. Chin, P. K. Saha, H. Hotchi, H. Harada, Y. Irie, F. Tamura, N. Tani, T. Toyama, Y. Watanabe, and M. Yamamoto, Theoretical elucidation of space-charge effects on the coupled-bunch instability at the 3 GeV rapid cycling synchrotron at the Japan Proton Accelerator Research Complex, Prog. Theor. Exp. Phys. **2017**, 013G01 (2017).

[7] P. K. Saha, Y. Shobuda, H. Hotchi, H. Harada, N. Hayashi, M. Kinsho, F. Tamura, N. Tani, M. Yamamoto, Y. Watanabe, Y. H. Chin, and J. A. Holmes, Simulation, measurement, and mitigation of beam instability caused by the kicker impedance in the 3-GeV rapid cycling synchrotron at the Japan Proton Accelerator Research Complex, Phys. Rev. Accel. Beams **21**, 024203 (2018).

[8] J-PARC, http://j-parc.jp/index-e.html.

[9] J. Kamiya, T. Takayanagi, and M. Watanabe, Performance of extraction kicker magnet in a rapid cycling synchrotron, Phys. Rev. ST Accel. Beams **12**, 072401 (2009).

[10] Fujikura Ltd, https://www.fujikura.com/.

[11] Y. Shobuda, Y. Irie, T. Toyama, J. Kamiya, and M. Watanabe, Measurement scheme of kicker impedances via beam-induced voltages of coaxial cables, Nucl. Instrum. Methods Phys. Res., Sect. A **713**, 52 (2013).

[12] Y. Shobuda, Y. Irie, and T. Toyama, Analytical approach to evaluate coupling impedances of traveling kicker magnets, Nucl. Instrum. Methods Phys. Res., Sect. A **691**, 135 (2012).

[13] W. Zhang, J. Sandberg, H. Hahn, J. Mi, C. Pai, Y. Tan, N. Tsoupas, J. Tuozzolo, D. Warburton, J. Wei, K. Rust, and R. Cutler, SNS extraction fast kicker pulsed power system, in *Proceedings of the 9th European Particle Accelerator Conference, Lucerne, 2004* (EPS-AG, Lucerne, 2004), https://epaper.kek.jp/e04/PAPERS/WEPKF087.PDF.

[14] Y. Shobuda, Y. H. Chin, N. Hayashi, Y. Irie, T. Takayanagi, T. Togashi, T. Toyama, K. Yamamoto, and M. Yamamoto, Reducing the beam impedance of the kicker at the 3-GeV rapid cycling synchrotron of the Japan Proton Accelerator Research Complex, Phys. Rev. Accel. Beams **21**, 061003 (2018).

[15] Y. Shobuda, Y. Irie, T. Takayanagi, T. Togashi1, K. Yamamoto, and M. Yamamoto, Reduction of the kicker impedance maintaining the performance of present kicker magnet at RCS in J-PARC, J. Phys. Conf. Ser. **1067**, 062007 (2018).

[16] E. Koukovini-Platia, M. J. Barnes, H. Bartosik, G. Rumolo, L. Sermeus, and C. Zannini, Source of horizontal instability at the CERN Proton Synchrotron Booster, Phys. Rev. Accel. Beams **22**, 124201 (2019).

[17] SPICE© ("Simulation Program with Integrated Circuit Emphasis"), https://en.wikipedia.org/wiki/SPICE.

[18] TOPSPICE©, https://penzar.com/topspice/topspice.htm.

[19] Origin Company Limited, https://www.origin.co.jp/eng/.

[20] T. Togashi, T. Takayanagi, K. Yamamoto, and M. Kinsyo, Current status of the kicker magnet power supply in 3-GeV RCS, in *Proceedings of the 13th Annual Meeting of Particle Accelerator Society of Japan, PASJ-2016, Chiba, Japan* (2016), MOP117, http://www.pasj.jp/web_publish/pasj2016/proceedings/PDF/MOP1/MOP117.pdf.

[21] CST STUDIO©, www.3ds.com/products/simulia/.

[22] Private communications to a staff of AET Inc., a distributor of CST STUDIO in Japan, https://www.aetjapan.com/english/index.php.

[23] M. Watanabe, N. Hayashi, Y. Shobuda, K. Suganuma, T. Takayanagi, T. Togashi, and T. Toyama, Operation and

current status of injection, extraction, kicker magnet and the power supply for J-PARC 3 GeV RCS, in *Proceedings of the 3rd International Particle Accelerator Conference, New Orleans, LA, 2012* (IEEE, Piscataway, NJ, 2012), https://accelconf.web.cern.ch/ipac2012/papers/thppd052.pdf.

[24] ANSYS Fluent©, https://www.ansys.com/products/fluids/ansys-fluent.

[25] F. P. Incropera, D. P. Dewitt, T. L. Bergman, and A. S. Lavine, *Fundamentals of Heat and Mass Transfer*, 6th ed. (John Wiley & Sons, New York, 2006).

[26] Shin-Etsu, https://www.shinetsu.co.jp/en/; http://www.shinetsusilicone-global.com/catalog/pdf/kf96_e.pdf.

[27] S. W. Churchil and M. Bernstein, A correlating equation for forced convection from gases and liquids to a circular cylinder in crossflow, J. Heat Transfer, **99**, 300 (1977), 10.1115/1.3450685.

[28] ANSYS©, 4.4.2 RNG k − ϵ model, https://www.afs.enea.it/project/neptunius/docs/fluent/html/th/node59.htm.

[29] S. A. Orszag, V. Yakhot, W. S. Flannery, F. Boysan, D. Choudhury, J. Maruzewski, and B. Patel, Renormalization group modeling and turbulence simulations, in *Proceedings of International Conference on Near-Wall Turbulent Flows, Tempe, AZ* (1993), p. 1031.

[30] NiGK Corporation, https://www.nichigi.co.jp/en/en_downloadform/en_data.html; Temperature label file:///Users/shoubuda/Downloads/NiGK_Catalog_Temperature-Indicating-Materials_2022.01.pdf.

[31] Fumihiko Tamura, Masanobu Yamamoto, Masahito Yoshii, Chihiro Ohmori, Masahiro Nomura, Alexander Schnase, Makoto Toda, Hiromitsu Suzuki, Taihei Shimada, Keigo Hara, and Katsushi Hasegawa, Longitudinal painting with large amplitude second harmonic rf voltages in the rapid cycling synchrotron of the Japan Proton Accelerator Research Complex, Phys. Rev. Accel. Beams, **12**, 041001 (2009).

[32] H. Hotchi, 1-MW beam operation scenario of the J-PARC 3-GeV Rapid Cycling Synchrotron, J. Phys. Soc. Jpn. Conf. Proc. **8**, 012013 (2015).

[33] P. K. Saha, Y. Shobuda, H. Hotchi, N. Hayashi, T. Takayanagi, H. Harada, and Y. Irie, Direct observation of the phase space footprint of a painting injection in the Rapid Cycling Synchrotron at the Japan Proton Accelerator Research Complex, Phys. Rev. Accel. Beams **12**, 040403 (2009).

[34] H. Hotchi, H. Harada, N. Hayashi, M. Kinsho, P. K. Saha, Y. Shobuda, F. Tamura, K. Yamamoto, M. Yamamoto, M. Yoshimoto, and Y. Irie, Beam loss reduction by injection painting in the 3 GeV rapid cycling synchrotron of the Japan Proton Accelerator Research Complex, Phys. Rev. Accel. Beams **15**, 040402 (2012).

[35] Y. Shobuda, P. K. Saha, H. Hotchi, H. Harada, T. Takayanagi, F. Tamura, N. Tani, T. Togashi, T. Toyama, Y. Watanabe, K. Yamamoto, M. Yamamoto, Y. H. Chin, and Y. Irie, Coupled bunch instability and its cure at J-PARC RCS, in *Proceedings of 7th International Particle Accelerator Conference, IPAC2017, Copenhagen, Denmark*, p. 2946, https://accelconf.web.cern.ch/ipac2017/papers/wepik014.pdf.

[36] *Handbook of Accelerator Physics and Engineering*, edited by A. W. Chao and M. Tigner (World Scientific, Singapore, 1999).

[37] H. Hotchi, H. Harada, S. Kato, K. Okabe, P. K. Saha, Y. Shobuda, F. Tamura, N. Tani, Y. Watanabe, and M. Yoshimoto, Realizing a high-intensity low-emittance beam in the J-PARC 3-GeV RCS, in *Proceedings of 7th International Particle Accelerator Conference, IPAC2017, Copenhagen, Denmark*, https://accelconf.web.cern.ch/ipac2017/papers/weoaa3.pdf.

[38] P. K. Saha, H. Harada, H. Hotchi, Y. Shobuda, T. Takayanagi, F. Tamura, and Y. Watanabe, Dynamic variation of chromaticity for beam instability mitigation in the 3-GeV RCS of J-PARC, in *Proceedings of the 10th International Particle Accelerator Conference, IPAC-2019, Melbourne, Australia, 2019* (JACoW, Geneva, Switzerland, 2019), 10.18429/JACoW-IPAC2019-MOPGW037.

[39] Y. Watanabe, N. Tani, T. Adachi, S. Igarashi, and H. Someya, Rapid-cycling power supplies for the J-PARC RCS sextupole magnets, *Proceedings of IPAC2011, 3338, San Sebastian, Spain*, https://accelconf.web.cern.ch/IPAC2011/papers/THPO003.PDF.

[40] N. Hayashi, M. Kawase, S. Hatakeyama, S. Hiroki, R. Saeki, H. Takahashi, Y. Teruyama, R. Toyokawa, D. Arakawa, S. Hiramatsu, S. Lee, K. Satou, M. Tejima, and T. Toyama, Beam position monitor system of J-PARC RCS, Nucl. Instrum. Methods Phys. Res., Sect. A **677**, 94 (2012).

[41] S. Meigo, M. Ohi, T. Kai, T. Ono, K. Ikezaki, T. Haraguchi, H. Fujimori, and S. Sakamoto, Beam commissioning for neutron and muon facility at J-PARC, Nucl. Instrum. Methods Phys. Res., Sect. A **600**, 41 (2009).

[42] H. Hotchi, Effects of the Montague resonance on the formation of the beam distribution during multiturn injection painting in a high-intensity proton ring, Phys. Rev. Accel. Beams **23**, 050401 (2020).

[43] J. Kamiya, T. Ueno, and T. Takayanagi, Magnetic field measurement of the extraction kicker magnet in J-PARC RCS, IEEE Trans. Appl. Supercond. **16**, 1362 (2006).

[44] H. Harada, P. K. Saha, F. Tamura, S. Meigo, H. Hotchi, N. Hayashi, M. Kinsho, and K. Hasegawa, Beam-based compensation of extracted-beam displacement caused by field ringing of pulsed kicker magnets in the 3 GeV rapid cycling synchrotron of the Japan Proton Accelerator Research Complex, Prog. Theor. Exp. Phys. **2017**, 093G01 (2017).

[45] J. Kamiya (private communication).

[46] NAT Corporation, https://nat-web.com/en/about/index.html.

[47] TDK Corporation, http://www.global.tdk.com/corp/en/index.htm.

[48] J. A. Holmes, Recent enhancements to the ORBIT code, in *Proceedings of the International Particle Accelerator Conference, Kyoto, Japan* (ICR, Kyoto, 2010), https://accelconf.web.cern.ch/IPAC10/papers/tupec080.pdf.

[49] Y. Shobuda and Y. H. Chin, Rigorous formulation of space-charge wake function and impedance by solving the three-dimensional Poisson equation, Sci. Rep. **8**, 12805 (2018).